



SAPIENZA  
UNIVERSITÀ DI ROMA

Department of Chemistry

Molecular processes in the early Universe environment:  
quantum dynamics and chemical evolution with ab initio  
methods.

Stefano Bovino

Submitted in partial fulfilment of the requirements  
of the degree of Doctor of Philosophy

October 2011

School of Chemistry Sciences

---

Thesis Advisor  
Prof. F. A. Gianturco

---

External Advisor  
Prof. G. Moretti



---

Principium cuius hinc nobis exordia sumet, nullam  
rem e nihilo gigni divinitus umquam. quippe ita  
formido mortalis continet omnis, quod multa in terris  
feri caeloque tuentur, quorum operum causas nulla  
ratione videre possunt ac fieri divino numine rentur.  
quas ob res ubi viderimus nil posse creari de nihilo,  
tum quod sequimur iam rectius inde perspicimus, et  
unde queat res quaeque creari et quo quaeque modo  
fiant opera sine divom.

*De rerum natura* "Libro 1, vv. 146-214", Lucrezio

Its foundation will take the start for us in this: that  
nothing ever is generated out of nothing by God's  
will. So the shock dominates all men because they see  
happening on earth and in heaven many phenomena of  
which in no way they can see the cause, hence they be-  
lieve that God's will produce them. Therefore, when  
we have seen that nothing can come from nothing,  
then from here we can more easily find what we seek,  
and from where all things can be generated, and how  
all things happen without the intervention of the gods.

*Translation*



# Acknowledgements

First of all, I would like to thank my supervisor prof. F. A. Gianturco. The professor has pushed me beyond the common view of the physical phenomena stimulating continuously my mind. To work with Franco has been certainly a life's experience which I will bring with me in the future, for the nice moments spiced by good jokes, good food, good wines and good laughs that he gave me. Thank you Franco.

I'm grateful to Dr. Mario Tacconi, a friend, a colleague, who led me inside the deep tunnel of "computational" chemistry, sharing with me the developing of the NIP code. Thank you Mario for every bad and good day we had together: it has been great to work, side by side, with you.

I would like to thank all the MQSQD group that "lived" the department, every day, with me: Francesco and Mauro (two expert men in life and science), Fabio M. and Fabio C. for useful discussions, and Domenico Caruso, the student who I supervised during his thesis stage and who shared with me good glasses of "Amaro del Capo". Thanks also to Isabella for her support from CASPUR.

Last but not the least I would like to thank those who supported and stood by me during these three long years: Rosy and my family.

Thank you to Dr. Daniele Galli for his support from Arcetri and his help in calculating the molecular fractional abundances presented in this thesis.

Finally I'm very grateful to Prof. A. Dalgarno and Prof. Vasili Kharchenko for having allowed me to work at the Harvard-College Center for Astrophysics for four months during my PhD program. Thank you very much also to Dr. Peng Zhang, a very good scientist and a very good friend, from whom I have learnt a lot.

I thank also anyone whom I may have forgotten to mention, and all my friends, far and close, who entertained me during my (little) free time.



# Contents

0.1	Something to laugh about before reading my thesis . . . . .	1
<b>1</b>	<b>Introduction</b>	<b>3</b>
1.1	Time, space, and redshift . . . . .	3
1.2	A brief history of the universe . . . . .	5
1.3	The chemistry of the early universe . . . . .	6
1.4	The first stars and galaxies . . . . .	7
1.5	Measurements and observations . . . . .	9
1.6	Aims of this PhD work . . . . .	11
<b>2</b>	<b>Photochemical dynamics: theory and observables</b>	<b>15</b>
2.1	Spontaneous and stimulated association processes . . . . .	15
2.2	Dynamics of photodissociation processes . . . . .	18
<b>3</b>	<b>The theory of reactive scattering</b>	<b>23</b>
3.1	The exact reactive scattering approach . . . . .	23
3.1.1	The hyperspherical method . . . . .	23
3.1.2	ABC program: overview and limits . . . . .	26
3.2	The reduced dimensionality methods . . . . .	28
3.2.1	$J$ -shifting approximation . . . . .	28
3.2.2	Coupled states approximation . . . . .	29
3.3	The Negative Imaginary Potential method . . . . .	30
3.3.1	Theoretical approach . . . . .	31
3.3.2	Generalized R-matrix Propagation . . . . .	33
3.3.3	Asymptotic Matching . . . . .	34
<b>4</b>	<b>Writing the NIP code</b>	<b>39</b>
4.1	Structure of the program . . . . .	39
4.1.1	The optimization procedure . . . . .	43
4.1.2	How to make a calculation . . . . .	44
4.2	Benchmarks . . . . .	47
4.2.1	$\text{H}_2 + \text{D}$ benchmark . . . . .	47
4.2.2	The $\text{LiH} + \text{H}$ neutral reaction: validating the method . . . . .	47
4.2.3	$\text{HeH}^+$ : a key reaction to test our NIP method . . . . .	49
<b>5</b>	<b>Results for the chemical routes</b>	<b>53</b>
5.1	The lithium chemistry . . . . .	53
5.1.1	$\text{LiH} + \text{H}$ depletion . . . . .	54
5.1.2	$\text{LiH} + \text{H}^+$ depletion . . . . .	62
5.1.3	$\text{LiH}^+ + \text{H}$ depletion . . . . .	68
5.1.4	$\text{LiH}^+ + \text{He}$ depletion and inverse reaction . . . . .	73
5.2	The $\text{HeH}^+$ : first molecule in the universe . . . . .	85
5.2.1	The quantum calculations . . . . .	85
5.2.2	Low energy behaviour . . . . .	87
5.2.3	The depletion rates . . . . .	91

## CONTENTS

---

<b>6</b>	<b>Photon induced dynamics: the case of <math>\text{LiHe}^+</math></b>	<b>95</b>
6.1	The formation of $\text{LiHe}^+$ . . . . .	95
6.1.1	The ground state intermolecular potential . . . . .	96
6.1.2	Radiative association computational results . . . . .	96
6.1.3	Photodissociation computational results . . . . .	100
6.2	Implications for the chemical network . . . . .	101
<b>7</b>	<b>The chemical network</b>	<b>107</b>
7.1	The evolutionary model . . . . .	107
7.2	The lithium chemistry . . . . .	108
7.2.1	$\text{LiH}$ chemistry . . . . .	108
7.2.2	$\text{LiH}^+$ chemistry . . . . .	110
7.2.3	Chemical evolution . . . . .	112
7.3	The helium chemistry . . . . .	113
<b>8</b>	<b>Conclusions</b>	<b>119</b>
<b>9</b>	<b>A thesis' coda</b>	<b>125</b>
9.1	My work at the Harvard-College Center for Astrophysics . . . . .	125
9.2	The energy transfer processes . . . . .	125
9.2.1	Kernel of Boltzmann equation . . . . .	126
9.3	The results . . . . .	127
9.3.1	S-Xe . . . . .	127
9.3.2	Helium escape from Mars atmosphere . . . . .	128



# List of Figures

1.1	Cosmic archeology of the observable volume of the universe . . . . .	4
1.2	The timeline of the universe formation . . . . .	5
1.3	First stars formation mechanisms . . . . .	9
1.4	Most Distant Galaxy Candidate Ever Seen in Universe . . . . .	10
1.5	WMAP seven years map of the sky . . . . .	10
2.1	Schematic diagram of the energy levels of a diatomic molecule . . . . .	16
2.2	Radiative association sketch . . . . .	17
2.3	Photodissociation sketch . . . . .	18
3.1	Jacobi coordinates . . . . .	24
3.2	ABC elapsed time . . . . .	26
3.3	ABC-GPU code performance . . . . .	27
4.1	NIP program flowchart . . . . .	41
4.2	NIP code optimization scheme . . . . .	43
4.3	The "jmax" parameters convergence tests . . . . .	44
4.4	The "nbasis" parameter convergence tests . . . . .	45
4.5	NIP stability convergence test . . . . .	46
4.6	H <sub>2</sub> + D NIP benchmark . . . . .	47
4.7	LiH + H benchmark . . . . .	48
4.8	Comparing HeH <sup>+</sup> + H results with experimental data . . . . .	49
5.1	ABC input parameters . . . . .	54
5.2	Computed quantum reaction rates of LiH destruction . . . . .	58
5.3	Computed rates for H <sub>2</sub> -formation reaction . . . . .	59
5.4	Computed hydrogen-exchange reaction and o-H <sub>2</sub> formation . . . . .	60
5.5	Computed quantum LiH destruction rates . . . . .	62
5.6	Computed $J=0$ reaction probabilities for reaction LiH + H . . . . .	63
5.7	A comparison of computed $J=0$ reaction probabilities for LiH(v=0) reactants . . . . .	64
5.8	Computed final cross sections for the two different channels of reaction LiH + H . . . . .	65
5.9	Computed thermal rate coefficients, as a function of temperature and redshift values, for the H <sub>2</sub> <sup>+</sup> formation channel . . . . .	67
5.10	Reactive scattering cross sections for R-IOSA (left) and R-CSA (right) methods . . . . .	69
5.11	Comparison of computed rate coefficients from different methods . . . . .	70
5.12	Collinear profile of the RPES for LiHHe <sup>+</sup> system. . . . .	74
5.13	Computed reactive probabilities ( $J = 0$ ) for the LiH <sup>+</sup> depletion reaction at low collision energies . . . . .	75
5.14	Computed reaction probabilities for the inverse, exothermic reaction leading to LiH <sup>+</sup> formation . . . . .	76
5.15	Computed reaction cross section for the depletion reaction of LiH <sup>+</sup> with He . . . . .	77

## LIST OF FIGURES

---

5.16	Computed reaction cross sections for the exothermic formation process of $\text{LiH}^+$ from $\text{LiHe}^+$ cations . . . . .	78
5.17	Computed reaction rates for the $\text{LiH}^+$ depletion reactions as a function of the initial vibrational state of $\text{LiH}^+$ and for the considered range of temperatures . . . . .	79
5.18	Computed reaction rates, as a function of $T$ , for the formation of $\text{LiH}^+$ from $\text{LiHe}^+$ in reaction with $\text{H}$ . . . . .	80
5.19	Computed reactive cross sections ( $J = 0$ ) for the formation reaction of $\text{LiHe}^+$ at low collision energies . . . . .	81
5.20	Same calculations as in figure 5.19, but this time for the inverse, destruction reaction for $\text{LiHe}^+$ . . . . .	82
5.21	Computed adiabatic potential curves for the $\text{LiH}^+ + \text{He}$ reaction . .	83
5.22	Computed adiabatic potential curves for the $\text{LiHe}^+ + \text{H}$ reaction . .	84
5.23	Computed reactive probabilities for $\text{HeH}^+$ . . . . .	86
5.24	Computed integral cross-sections as a function of energy . . . . .	87
5.25	Computed reaction probabilities for $\text{HeH}^+$ at ultralow energies. . . .	88
5.26	Scattering length for $\text{HeH}^+$ at very low energies . . . . .	89
5.27	Computed, radial adiabatic potential curves $V_i(R)$ for $\text{HeH}^+$ . . . . .	90
5.28	Computed rate coefficient for the reaction 5.17 as a function of $T$ . .	91
6.1	Computed cross sections for stimulated plus spontaneous radiative association of $\text{Li}^+$ and $\text{He}$ . . . . .	98
6.2	Rate coefficients for stimulated plus spontaneous radiative association of $\text{Li}^+$ and $\text{He}$ . . . . .	100
6.3	Computed $\text{LiHe}^+$ photodissociation cross sections as function of photon energy . . . . .	101
6.4	Computed $\text{LiHe}^+$ photodissociation rate coefficients as function of black-body radiation temperature . . . . .	102
6.5	Production/destruction rates for $\text{LiHe}^+$ . . . . .	103
7.1	Production/destruction rates of $\text{LiH}$ . . . . .	110
7.2	Production/destruction rates of $\text{LiH}^+$ . . . . .	111
7.3	Relative abundances of $\text{LiH}$ and $\text{LiH}^+$ . . . . .	112
7.4	Computed production/destruction rates of $\text{HeH}^+$ as function of redshift	114
7.5	Computed relative abundances of $\text{HeH}^+$ in the post-recombination era as function of redshift $z$ . . . . .	115
9.1	The production rate of $^4\text{He}$ escape flux as a function of altitude . . .	132

# List of Tables

4.1	NIP code wall clock time . . . . .	43
5.1	Computed rate coefficients summed over all final states of the products	55
5.2	Calculated rate coefficients, summed over all final o-H <sub>2</sub> states, for different vibrational initial states of LiH . . . . .	55
5.3	Computed rates of H <sub>2</sub> formation into different rotovibrational states	59
5.4	Computed rate coefficients summed over all final states of the products	66
5.5	Computed depletion and survival rate coefficients . . . . .	72
5.6	Computed production/destruction rates of HeH <sup>+</sup> as function of redshift	92
6.1	Spectroscopic parameters for the three ionic molecules thought to be present in the early universe stage as among the most likely compo- nents of the latter . . . . .	96
6.2	Computed dipole moment $\mu(R)$ as a function of internuclear distances	97
6.3	Computed rotovibrational resonances for the ground electronic state of the LiHe <sup>+</sup> ion . . . . .	99
6.4	Computed total, spontaneous plus stimulated, radiative association rate coefficients for Li <sup>+</sup> + He . . . . .	99
7.1	Cosmological model . . . . .	108
7.2	List of considered reactions . . . . .	109
7.3	Computed rate coefficient for the reaction HeH <sup>+</sup> + H as a function of T . . . . .	113



## 0.1 Something to laugh about before reading my thesis

### WRITING YOUR THESIS OUTLINE

NOTHING SAYS "I'M ALMOST DONE" TO YOUR ADVISOR/SPOUSE/PARENTS LIKE PRETENDING YOU HAVE A PLAN

**STEP 1** Aim for a respectable number of chapters:

**THESIS OUTLINE**

- 1.
- 2.
- 3.
- 4.
5. ← chapter #'s
- 6.
- 7.

5 = "That's IT??"  
6-7 = "Not bad"  
8+ = "Are you crazy??"

**STEP 2** Fill in the "freebies":

**THESIS OUTLINE**

1. INTRODUCTION
2. LIT REVIEW
3. METHODOLOGY
- 4.
- 5.
- 6.
7. CONCLUSIONS

You're half way done!


**STEP 3** Make up titles for the "meat" chapters:

2. LIT REVIEW
3. METHODOLOGY
4. (THAT STUFF YOU DID YOUR FIRST YEAR)
5. (STUFF YOU'RE SUPPOSED TO BE DOING NOW)
6. (MAKE STUFF UP)
7. CONCLUSIONS

(It'll be years before you actually have to work on that later chapter, and by then your thesis topic will have changed anyway)

**STEP 4** Voilà! You just bought yourself another two years

So, how's your thesis going? i have an outline!



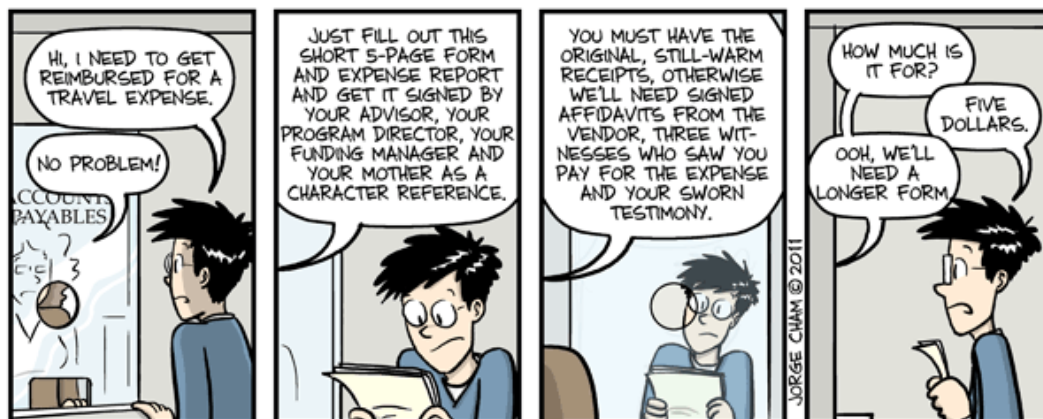
www.phdcomics.com

NET EFFECT OF A VACATION ON WORK PRODUCTIVITY = Clearing your mind and recharging your batteries - Travel Stress - Realizing how much better life would be if you didn't have to work = 0



JORGE CHAM © 2011

WWW.PHDCOMICS.COM



WWW.PHDCOMICS.COM



*Long as I remember  
The rain's been coming down  
Clouds of mystery fallin'  
Confusion on the ground*

# 1

## Introduction

When I started my PhD work, my knowledge about astrophysics was well-nigh little and confused. In the past, some of professor Gianturco's students had been involved in this fascinating world obtaining very good results which nowadays are cited by the community but, for long time, the early universe topic has remained frozen and the interest on this field is decreased.

During my first meeting with Franco, in 2008 when I was beginning my PhD work, we talked about different possible problems to be tackled in my research program like Efimov states, the quantum Monte Carlo calculations for helium clusters, and last but not the least the atom-molecule reactive scattering for the  $\text{LiH}_2$  system. The latter was the problem which I decided to study and which gave a strong push to a deep analysis of some important astrophysics' topics.

After three years of work I can of course state that some astrophysical concepts, at least I think, are not so confused and dark anymore even if the "dark age" has been the subject of my thesis. What I learnt is that the contribution of a theoretical chemist, inserted in a more broad context, is crucial for a complete and clearer understanding of the astronomical phenomena. I then realized that the theoretical astrochemistry is the continuous production of rate coefficients and other important quantities which can lead the astrophysicist to model our complex universe and travel back into its past. However, the best definition of the astrochemistry has been stated by professor Alexander Dalgarno: "*the astrochemistry is a blending of astronomy and chemistry in which each area enriches the other in a mutually stimulating interaction*".

Part of my work in these three years have been that of confirming the Dalgarno's definition of astrochemistry, trying to contribute with my calculations to the building of a clearer chemical evolution model of the early universe which led to the formation of the first astronomical objects, a still unsolved puzzle for the observers.

### 1.1 Time, space, and redshift

---

We know that the universe is expanding which means that the distance between objects, which are locally at rest, is increasing steadily. It also means that the wavelength of light is increasing while traveling between two objects which are locally at rest. The ratio between the wavelength of the observed light and the wavelength of the emitted light is equal to the relative change of the linear distance scale:

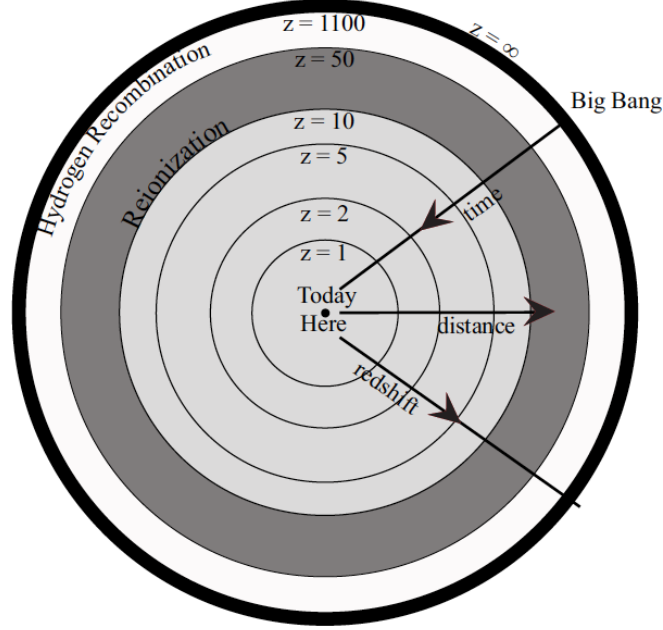


Figure 1.1 Cosmic archeology of the observable volume of the universe.

$$\frac{\lambda_{obs}}{\lambda_{em}} = \frac{a_{obs}}{a_{em}} \quad (1.1)$$

where  $\lambda_{obs}$  is the observed wavelength,  $\lambda_{em}$  is the emitted wavelength, and  $a_{obs}/a_{em}$  is the ratio between the cosmic scale when the light is observed, and the cosmic scale at the time of the light emission [1,2]. The cosmic scale factor  $a$  represents the relative expansion of the universe in the well-known Friedmann equations.

In astronomy this wavelength change is usually expressed by the "redshift"  $z$ , which is defined as

$$z = \frac{\lambda_{obs} - \lambda_{em}}{\lambda_{em}} = \frac{a_{obs}}{a_{em}} - 1. \quad (1.2)$$

For spectral lines,  $\lambda_{em}$  can be determined by means of laboratory measurements or by quantum-mechanical calculations.

The wavelength change actually measured in astronomical spectra differs from the redshift defined above, since, galaxies are moving relative to the local rest frame. Due to the Doppler effect, these local motions also produce wavelength shifts, which add to the wavelength due to the cosmic expansion. In order to derive accurate redshifts caused by the cosmic expansion, the measured wavelength shifts have to be corrected for the peculiar velocities of the observed objects (and for the motion of the observer). The effects of the peculiar velocities normally amount to  $\Delta\lambda/\lambda \leq 0.01$  therefore, the relative effect of the peculiar velocities are very important for nearby objects.



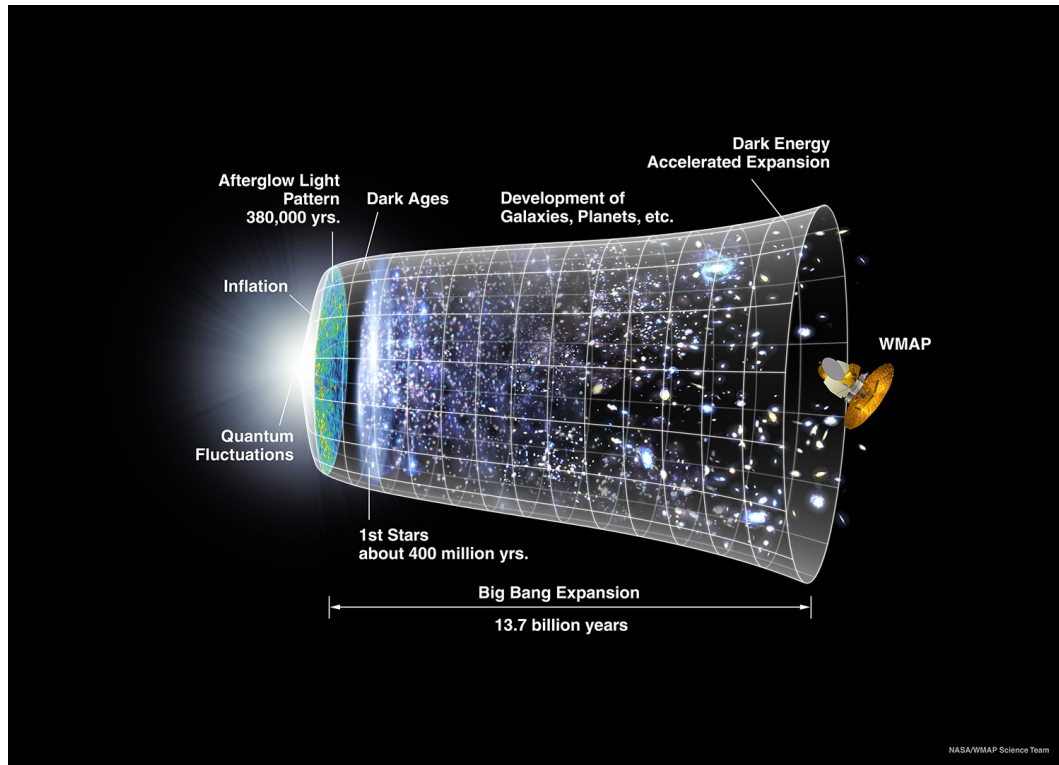


Figure 1.2 The timeline of the universe formation taken from WMAP resources site.

Since the redshift as defined above increases monotonically with distance and with the time which elapsed since the observed light was emitted, in the astronomical literature the dimensionless redshift  $z$  is often used as a measure of distances, for characterizing ages, and for defining time intervals (see figure 1.1). The use of  $z$  obviously has the advantage that, at least in principle, is a directly measurable quantity, and that distances and times expressed in terms of  $z$  can be easily compared.

## 1.2 A brief history of the universe

In the conventional view, the Universe began in a hot Big Bang some 13.7 billion years ago, and has been expanding ever since [3]. After the Big Bang a period called inflation during which the universe was dominated temporarily by the mass density of an elevated vacuum state, and experienced exponential expansion, occurred. After inflation, an unknown process, called "baryogenesis", generated an excess of particles over antiparticles. As the Universe cooled to a temperature of  $\sim 10^{12}$  K, protons and neutrons condensed out of the primordial quark-gluon plasma through the so-called QCD phase transition. When the temperature was still thousands of millions of kelvins, collisions between subatomic particles created hydrogen ( $\sim 76\%$ ) and helium ( $\sim 24\%$ ) nuclei with some traces of deuterium ( $10^{-4}$ ), lithium ( $10^{-10}$ ) and

beryllium ( $10^{-10}$ ). At this stage the matter was entirely ionized. *Recombination era* began when the temperature was low enough that the newly formed atoms could survive for further evolution [4]. In this era, at a redshift around  $z = 2500$  the Universe was about 100,000 years old and the temperature was about 4000 K. After recombination, the density was still very low and three-body reactions were still very inefficient: however, it was then that the first molecular species were postulated to be formed through radiative association. Matter and radiation decoupled at this stage and the Universe became transparent for most wavelengths.

With the diminishing density and temperature, chemistry came to an end and the universe started to getting darker. However, original fluctuations otherwise uniform cosmic flow were growing through gravitational instabilities and were developing into minihalos of mass  $10^6 M_\odot$  which collapsed at  $z \sim 30$ . The halos are host to primordial gas cloud clumps which collapsed to form the first stars which are metal free and are designed Population III stars. From this point forward the universe enriched of heavy elements coming from the death of the first stars and evolved in a more complex universe made of stars, galaxies, nebulae, quasars, planets and life, the universe that we can observe today. In figure 1.2 a timeline of the universe formation is shown.

As a matter of fact, the distance from which we can receive light is small, since during the first 380,000 years Thomson scattering by the free electrons of the hot cosmic plasma made the cosmos opaque. The light which should reach us includes the photon which are emitted by the recombining plasma itself. Mainly visual and near-infrared photons were emitted by plasma. But due to their redshift these photons today are observed as the Cosmic Microwave Background (CMB), which was discovered in 1965 at radio wavelengths.

### 1.3 The chemistry of the early universe

---

The chemistry of the early universe encompasses several pathways like non-reactive collisions, ion-molecule reactions, reactions driven by electron-collision and two body association reactions. Only a few processes are known to be effective at very low density, where there are no ultraviolet radiation, shocks waves or winds from active stellar objects. Over the last 30 years fairly comprehensive analysis of gas-phase reaction relevant for the physical environment of the expanding universe has been presented by different authors [5,6]. The main molecular species fractional abundances have also been critically analysed [7–10]. Lepp et al [8] identified 200 reactions considered to contribute to the abundance of 23 atomic and molecular species.

In such astrophysical environments lacking dust, molecules can only be formed through two-body radiative process. The first reaction leading to the formation of a molecule was postulated to be the radiative association of  $H^+$  and He



and then the  $HeH^+$  was the first molecule formed in the early universe age. The radiative processes were enhanced by stimulated emission by the background radiation field [11]. Such processes led also to the formation of other molecules such as LiH,

$\text{LiH}^+$ ,  $\text{H}_2^+$ ,  $\text{HD}$ ,  $\text{HD}^+$ ,  $\text{He}_2^+$  and  $\text{LiHe}^+$ . On the contrary,  $\text{H}_2$  (the most abundant species) was formed by associative detachment process



and by a two-steps process which involve the  $\text{H}_2^+$  molecule



The main destroying paths for the molecules under the conditions existing in the early universe environment are the following:

- dissociative recombination  $\text{XY} + \text{e}^- \rightarrow \text{X}^- + \text{Y}$
- reaction path, including also exchange reactions,  $\text{XY} + \text{Z} \rightarrow \text{XZ} + \text{Y}$
- photodissociation  $\text{XY} + h\nu \rightarrow \text{X} + \text{Y}$

The possible presence of even a small fraction of molecular gas allows us to collect molecular spectral data and to better understand the evolution of the universe at the formation of the first galaxies and stars. Hence, because of the high density of their rovibrational states, molecules can absorb thermal energy from the surrounding atomic gas via internal excitations and then release it through emission of photons, thereby efficiently cooling the surrounding clouds. In turn, these photons can increase the density of the CMB, thereby inducing both spectral distortions and spatial anisotropies [12, 13].

---

## 1.4 The first stars and galaxies

---

As pointed out above, at the recombination epoch the Universe was highly uniform, whereas today the Universe has condensed into stars, galaxies, and clusters of galaxies: how and when this transition occurred is one of the still outstanding problems in astrophysics. However, we already know that the first objects (Population III stars) were formed during a collapsing stage that took place within a reasonably local volume, say 1 comoving  $\text{Mpc}^3$ , at redshift  $\sim 30$  [14], and that the process was controlled by events dominated by atomic and molecular physics.

The latest evidence of the existence of galaxies at high redshifts ( $z > 7$ ) [15–17] and the discovery of a low-mass star with an iron abundance as low as  $1/200,000$  of the solar value [18, 19] suggested that Population III stars could still be in existence. The chemical composition of this highly metal-deficient stars largely reflects the composition of the gas from which they were formed. These old stars would thus allow the direct study of the primordial gas originating from the Big Bang [20].

As stated in previous sections embedded in the cooling cosmic gas were fluctuations in density of order  $10^{-5}$  sufficient that they could grow by gravity to create objects of a size that gravitational collapse could occur.

As the density contrast between a spherical gas cloud of mass  $M$  and its cosmic environment grows, there are two main forces which come into play. The first is gravity and the second is pressure. The increase in gas density near the center of the cloud send out a pressure wave which propagates out at the speed of sound. The wave tries to even out the density enhancement, consistent with the tendency of pressure to resist collapse. At the same time, gravity pulls the cloud together in the opposite direction. The characteristic time scale for the collapse of the cloud is given by its radius  $R$  divided by the free-fall speed  $\sim (2GM/R)^{1/2}$  (where  $G$  is the Newton's gravitational constant), yielding  $t_{coll} \sim (G < \rho >)^{-1/2}$  where  $\langle \rho \rangle = M / \frac{4\pi}{3} R^3$  is the characteristic density of the cloud as it turns around on its way to collapse. If the sound wave does not have sufficient time to traverse the cloud during the free-fall time, namely  $R > R_J$ , then the cloud will collapse. Under these circumstances, the sound wave moves outward at a speed that is slower than the inward motion of the gas, and so the wave is simply carried along together with the infalling material. On the other hand, the collapse will be inhibited by pressure for a sufficiently small cloud with  $R < R_J$ . The transition between these regimes is defined by the so-called Jeans radius  $R_J$  corresponding to the Jeans mass

$$M_J = \frac{4\pi}{3} \langle \rho \rangle R_J^3. \quad (1.7)$$

As long as the gas temperature is not very different from the CMB temperature, the value of  $M_J \sim 10^5 M_\odot$  is independent of redshift. This is the minimum total mass of the first gas cloud to collapse  $\sim 100$  million years after the Big Bang which led to the formation of very massive stars of  $100\text{--}500 M_\odot$  (a formation mechanism is shown in figure 1.3). Generally speaking, until stellar densities are reached, there must be a radiative cooling mechanism for the gas to lose its energy and concentrate to ever-higher densities in the halo centers; without cooling, the gas reaches hydrostatic equilibrium (following the virial theorem) in the halo after the gravitational collapse and stays at a fixed density without forming stars. The ability of the gas to cool depends on the chemical composition and on the virialized temperature. The primordial gas in the first halos was mainly composed of atomic H and He with some traces of Li. Atomic H induced radiative cooling only when  $T_{vir} > 10^4$  K, when collisions can excite and ionize H atoms; the gas can readily contract to form galaxies. In the intermediate range  $100 \text{ K} < T_{vir} < 10^4 \text{ K}$ , the gas settles into halo but atomic cooling is not available and, in the absence of the heavy elements that were formed only after massive stars ejected their synthesized nuclei into space, the only available coolants are molecules. It has also long been recognized that the most important coolant at  $T < 10^4$  K in primordial gas is molecular hydrogen,  $\text{H}_2$  [21,22] and that  $\text{H}_2$  becomes increasingly ineffective as we move to higher densities [23]. These findings have indeed motivated several authors to additionally examine the role that might have been played by other molecular coolants at the expected high densities of that environment. The best studied alternative coolant is naturally the HD molecule [24] whose radiative transitions can occur through the  $j=1 \rightarrow 0$  rotational transitions that are located at lower temperatures when compared with  $\text{H}_2$  molecules. As a consequence of such investigative extensions,  $\text{LiH}$ ,  $\text{HeH}^+$ ,  $\text{H}_2^+$  and  $\text{H}_3^+$  have also attracted considerable attention. The low excitation threshold and

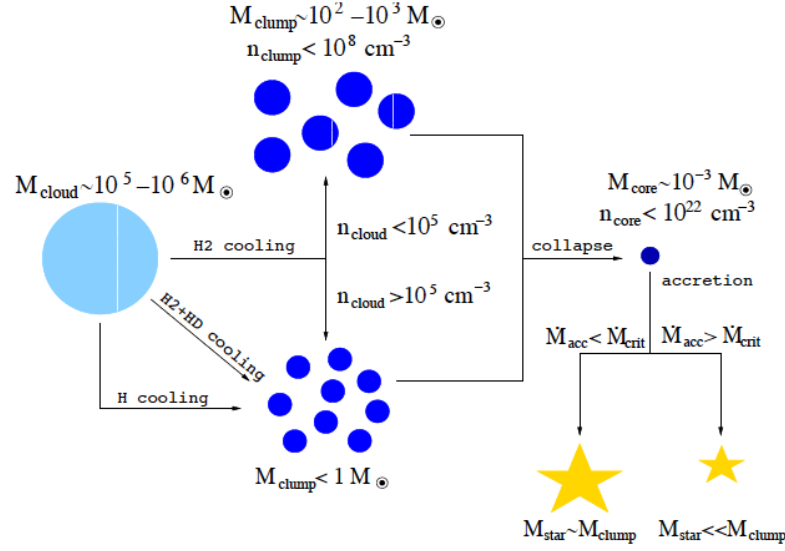


Figure 1.3 Mechanism of the formation of the first stars.

the efficient radiative decay along the rovibrational manifold are, in fact, additional properties that could favor the role of the above molecules as coolants of the primordial gas [25].

## 1.5 Measurements and observations

Because of the finite time it takes light to travel to us from distant sources, we can see images of the universe when it was younger by looking deep into space through powerful telescopes. Since we know very well that our universe is evolving with time, observations of distant astronomical objects allow us to study the history of our cosmos. In the light of the most distant objects we directly see the universe in its earliest stages of development. Existing data sets include an image of the universe when it was 400 thousand years old (WMAP 5), as well as images of individual galaxies when the universe was older than a billion years. In between these two epochs was a period when the universe was dark, stars had not yet formed, and the cosmic microwave background no longer traced the distribution of matter. This is precisely the most interesting period, when the primordial soup evolved into the rich zoo of objects we now see.

What the astronomers do is to collect data coming from ground and space telescopes with high resolution and good sensitivity. A telescope that could help to find the answers about universe formation would have to be giant, sensitive telescope, capable of collecting and discerning the light from very faint galaxies. An historical example, which today represents yet a very good instrument for observations, is the IRAM telescope which measures emission of molecular gas and dust from 1979. It is a 30-m telescope which thanks to its large surface is well adapted to detect weak

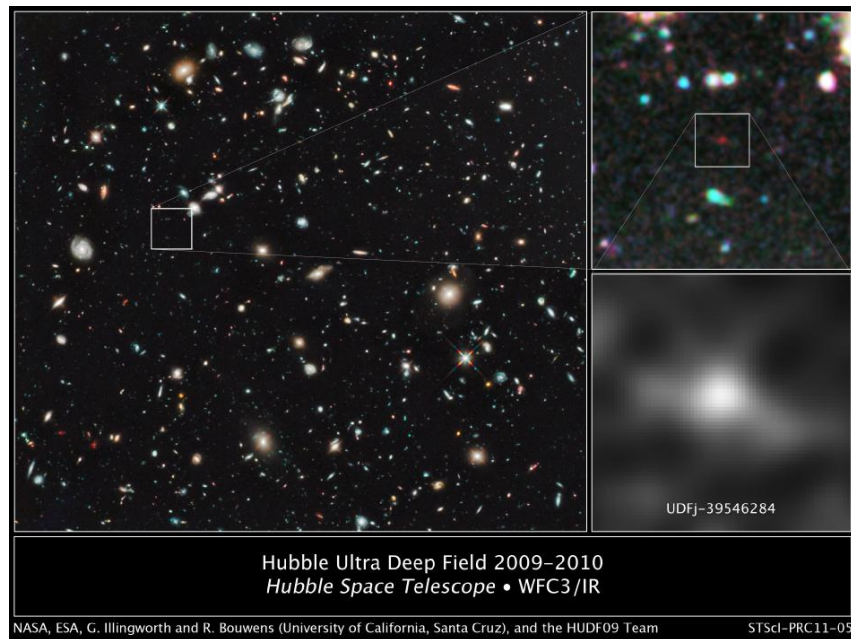


Figure 1.4 The farthest and one of the very earliest galaxies ever seen in the universe appears as a faint red blob in this ultra-deepfield exposure taken with NASA's Hubble Space Telescope

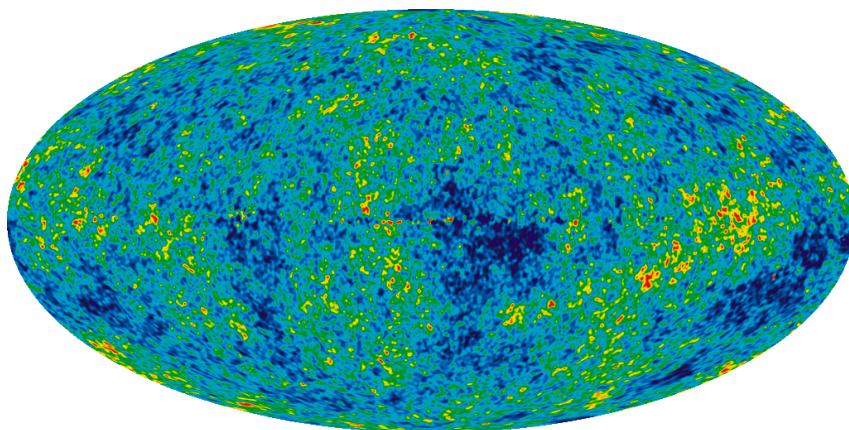


Figure 1.5 The detailed, all-sky picture of the infant universe created from seven years of WMAP data.

sources. The millimeter wavelength range is, in fact, essential to astronomy, since gas-enshrouded cosmic objects remain optically invisible. Using radio techniques, astronomers can push the frontiers, penetrate the most distant galaxies, analyse black holes at the edge of the observable universe and trace the cosmological radiation up to its source, the Big Bang.

HERSCHEL, launched in 2009 with the aim to explore the infrared spectrum of the universe looking at the very distant galaxies, is another powerful and sophisticated instrument available for the astronomers.

Fundamental insights into galaxy formation and evolution come also from Hubble Space Telescope which allowed to discover some of the oldest objects ever seen in the universe. The latest discovery is a magnificent red blob which light traveled 13.2 billion years to reach Hubble, roughly 150 million years longer than the previous record holder. The tiny, dim object is a compact galaxy of blue stars that existed 480 million years after the big bang (figure 1.4). The new research offers surprising evidence that the rate of star birth in the early universe grew dramatically, increasing by about a factor of 10 from 480 million years to 650 million years after the big bang.

Finally, Wilkinson Microwave Anisotropy Probe, more commonly named WMAP, revealed conditions as they existed in the early universe by measuring the properties of the cosmic microwave background radiation over the full sky. The WMAP team has reported the first direct detection of pre-stellar helium, providing an important test of the big bang prediction. WMAP has detected a key signature of inflation and drawn the first map of the early universe with a very high accuracy (figure 1.5).

Nowadays, the observers are moving ahead along several fronts. The first involves the construction of large infrared telescopes on the ground and in space that will provide us with new photos of galaxies in the Universe at intermediate ages. Current plans include ground-based telescopes which are 24-42 m in diameter, and NASA's successor to the Hubble Space Telescope, the James Webb Space Telescope. In addition, several observational groups around the globe are constructing radio arrays that will be capable of mapping the three dimensional distribution of cosmic hydrogen left over from the Big Bang in the infant Universe. These arrays are aiming to detect the long-wavelength (redshifted 21 cm) radio emission from hydrogen atoms.

## 1.6 Aims of this PhD work

---

Since the observers are doing a lot to push our eyes beyond the actual limits of knowledge of the Universe, we think that our theoretical work could be helpful to sketch out some of the several aspects of its chemical evolution. The calculations of the main rate coefficients for the reactions involving the most important molecules thought to be formed during the recombination era and the evaluation of their relative abundances can certainly put a border to the possible role that such molecules had during the collapsing stage for the formation of the first galaxies.

The aim of this work has been, then, that of calculating the rates of the main destruction paths for  $\text{LiH}$ ,  $\text{LiH}^+$  and  $\text{HeH}^+$  molecules and their relative abundances.

The chemistry of Li in the early universe has been discussed in the past, reaching contrasting conclusions (see e.g., [6, 7, 25]). Of critical relevance, is the uncertainty

in the knowledge of reliable reaction rates for the destruction of LiH and LiH<sup>+</sup> molecules via strongly exothermic reactions without entrance barriers:



and



Therefore, it is an accurate knowledge of the reaction rates for the above processes, at low redshift values, that can ultimately tell us what the end-role of the LiH/LiH<sup>+</sup> systems could be as efficient coolants under early universe conditions. The task of the present work is to show that the reaction rates determined from fully ab-initio quantum methods, which also employ accurate interaction forces between partners, have a significant impact on the evolution of LiH and LiH<sup>+</sup> during the post-recombination era of the early universe.

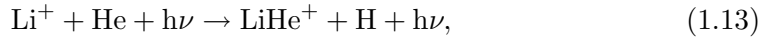
In the second part of my PhD program we studied in detail the destruction path of the HeH<sup>+</sup> molecule



which has never been studied with sufficient accuracy from a theoretical point of view. This allowed us to revise its abundance and its role in the evolution of the early universe.

We think that our work could definitively let us decide on the possible abundances of LiH, LiH<sup>+</sup> and HeH<sup>+</sup> opening the way for future observations, as proved by the last attempts in searching extragalactic LiH [26] and HeH<sup>+</sup> in a high redshift objects [27].

Finally, the lack of informations about LiHe<sup>+</sup>, one of the first molecules formed at the early stage of the universe, has convinced us to study and analyze the formation and destruction processes which can lead to the evaluation of its final abundance and then allow us to further extend the network of reactions which model the evolution of the early universe composition. We, then, calculated the rates for the radiative association processes:



and the destruction pathway with the surrounding hydrogen:



All the aspects of our results will be discussed and analyzed in the following chapters.



# Bibliography

- [1] Loeb A., How did the first stars and galaxies form?, 2010, Princeton University Press
- [2] Appenzeller I., High-redshift galaxies. Light from the early universe, 2009, Springer-Verlag Berlin Heidelberg
- [3] Hartquist T. W. and Williams D. A., The Chemically Controlled Cosmos, 1995, Cambridge University Press
- [4] Dalgarno A., J. Phys.: Conf. Series, **4**, 10, 2005
- [5] Puy D., Alecian G., Le Bourlot J., Léorat J. and Pineau des Forêts G., Astron. Astrophys., **267**, 337, 1993
- [6] Stancil P. C., Lepp S. and Dalgarno A., Astrophys. J., **458**, 401, 1996
- [7] Galli D., & Palla F., A&A, **335**, 403, 1998
- [8] Lepp S., Stancil P. C., & Dalgarno A., J. Phys. B: At. Mol. Opt. Phys., **35**, R57, 2002
- [9] Lepp S. and Shull J. M., Astrophys. J., **280**, 465, 1984
- [10] Kirby K., Physica Scripta, **T95**, 95, 1995
- [11] Stancil P. C., and Dalgarno A., Faraday Discussion, **109**, 61, 1998
- [12] Dubrovich V. K., Astron. Lett., **19**, 53, 1993
- [13] Dubrovich V. K., Sov. Astron. Lett., **3**, 128, 1977
- [14] Glover S. C. O., Space. Sci. Rev., **117**, 445, 2005
- [15] Bouwens R. J. et al., ApJ, **708**, L69, 2010
- [16] Bouwens R. J. et al., ApJ, **709**, L133, 2010
- [17] Bouwens R. J. et al., Nature, **469**, 504, 2011
- [18] Frebel A. et al., Nature, **434**, 871, 2005
- [19] Christlieb N. et al., Nature, **419**, 904, 2002
- [20] Bromm V., Yoshida N., Ann. Rev. Astron. Astrophys., **49**, 373, 2011
- [21] Saslaw W. C., and Zipoy D., Nature, **216**, 976, 1967
- [22] Peebles P. J. E. & Dicke R. H., ApJ, **154**, 891, 1968
- [23] Omukai K., and Nishi R., ApJ, **508**, 141, 1998
- [24] Flower D. R., Le Bourlot J, Pineau de Forêts G., and Roueff E., Mon. Not. R. Astron. Soc., **314**, 753, 2000

## BIBLIOGRAPHY

---

- [25] Bougleux E. and Galli D., *Mon. Not. R. Astron. Soc.*, **288**, 638, 1997
- [26] Friedel D. N., Kembell A., and Fields B. D., *ApJ*, **738**, 1, 2011
- [27] Zinchenko I., Dubrovich V., and Henkel C., *MNRAS*, **415**, L78, 2011

*Good men through the ages  
Tryin' to find the sun  
And I wonder, Still I wonder  
Who'll stop the rain?*

# 2

## Photochemical dynamics: theory and observables

Molecules have been found to exist in a rich variety of astrophysical environments, including stellar atmospheres, comets, planetary atmospheres, and the dense and diffuse clouds in the interstellar medium. An understanding of molecular structure, spectroscopy and photoabsorption processes is thus of critical importance in interpreting many of the current observations, in theoretically modeling these various astrophysical regions, and in judging the reliability of the available molecular data. Even in our own atmosphere, considerations of molecular photoabsorption determine "windows" in the electromagnetic spectrum in which one can carry out ground-based observations.

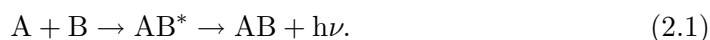
The vibrational and rotational nuclear degrees of freedom add significantly to the spectroscopic complexity of a molecule compared with an atom. As in an atom, transitions between different electronic energy levels in a molecule are generally observed at optical (4000-6000 Å) and ultraviolet (800-4000 Å) wavelengths (figure 2.1), whereas transitions between vibrational energy levels and rotational energy levels generally take place in the infrared region (2-20  $\mu\text{m}$ ) and microwave region (0.2 mm) of the electromagnetic spectrum, respectively.

Molecular photoabsorption may also lead to destruction of the molecule, through dissociation or ionization. Cross section and/or rate constants for such processes are essential in interpreting or predicting observed abundances of various molecular species.

### 2.1 Spontaneous and stimulated association processes

---

As it is well known, the formation of diatomic bound species during the early universe epoch, when the number density and hence the number of collisions were very low, could have been possible only by two-body processes like radiative association encounters (see figure 2.2) between the most abundant atomic components at that time,



This is usually a process with much lower probability than associative recombination via three-body collisions, whereby the residual energy is transferred during the

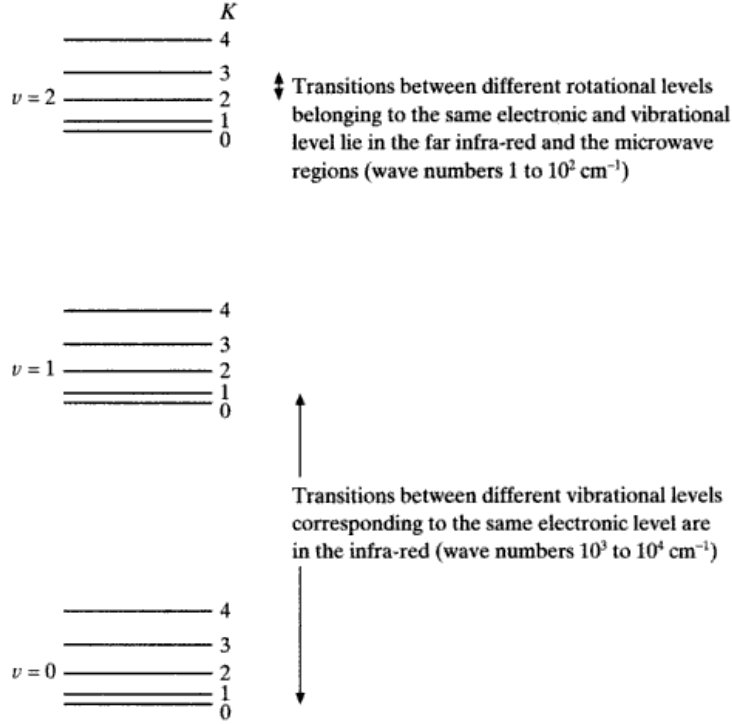


Figure 2.1 Schematic diagram of the energy levels of a diatomic molecule.

encounter, since in the former case the time needed to emit the photon from the excited state ( $10^{-8} \text{ s}$ ) is much longer than the interaction time between partners ( $10^{-13} \text{ s}$ ). When one views the process within the conventional Born-Oppenheimer (BO) approximation, then the relative motion of the interacting partners could either follow adiabatically the single electronic potential energy curve (PEC) of the molecular ground state or could move first along one of the electronically excited PECs of the diatom and then radiatively reach a bound state of the electronic ground state. As the latter process corresponds to a vibronic transition, it usually occurs with a greater probability than the former pure rovibrational transitions

From the computational standpoint, the cross section for direct two-body association, in atomic units, is given by:

$$\sigma_{sp}(E) = \frac{64}{3} \frac{\pi^5}{c^3} \frac{p}{k^2} \sum_{n'J',J} \nu_{E,n',J'}^3 S_{JJ'} M_{n'J',EJ}^2 \quad (2.2)$$

where  $k^2 = 2\mu E$ ,  $E$  being the collision energy,  $p$  the statistical weight of the initial electronic state,  $\nu$  the emitted photon frequency,  $S_{JJ'}$  is the Hönl-London coefficient [1], and

$$M_{n'J',EJ} = \int_0^\infty \phi_{n'J'} \mu(R) f_{EJ}(R) dR \quad (2.3)$$

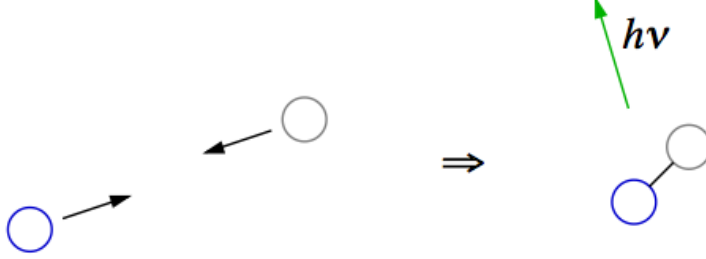


Figure 2.2 Graphical sketch of the radiative association process.

is the matrix element of the transition dipole moment  $\mu(R)$  between the relevant rovibrational bound states  $\phi_{n'J'}$  and the initial energy-normalized continuum function  $f_{EJ}$  [2,3]. V. K. Dubrovich and Stancil & Dalgarno [4] subsequently have suggested that the radiative association may be significantly enhanced by stimulated emission because of the cosmic background radiation with frequency  $\nu_b$ ,

$$A + B + h\nu_b \rightarrow AB + h\nu + h\nu_b. \quad (2.4)$$

The evaluation of the stimulated process is additionally given by the following equation:

$$\sigma_{st}(E) = \frac{8}{3} \frac{\pi^4}{c} \frac{p}{k^2} \sum_{n',J',J} I(\nu) S_{JJ'} M_{n'J',EJ}^2 \quad (2.5)$$

where  $I(\nu)$  is the background radiation field (BRF) characterized by a temperature  $T_b$ :

$$I(\nu) = \frac{4h\nu^3}{c^2} \frac{1}{\exp(h\nu/\kappa T_b) - 1} \quad (2.6)$$

with a photon energy  $h\nu = E - \varepsilon_{n'J'}$ ,  $\kappa$  being the Boltzmann constant. The total, spontaneous plus stimulated, cross section is then given by [4]

$$\sigma(E) = \frac{64}{3} \frac{\pi^5}{c^3} \frac{p}{k^2} \sum_{n',J',J} \nu_{E,n',J'}^3 S_{JJ'} M_{n'J',EJ}^2 \left[ \frac{1}{1 - \exp(-h\nu/\kappa T_b)} \right] \quad (2.7)$$

The general behavior of the individual cross sections and the effect of the various PEC features at low collision energies are functions of the specific system and will therefore behave very differently depending on the particular final diatomic product that we shall consider. Generally speaking, however, one should expect they will drop rather rapidly with collision energy since the corresponding Franck-Condon

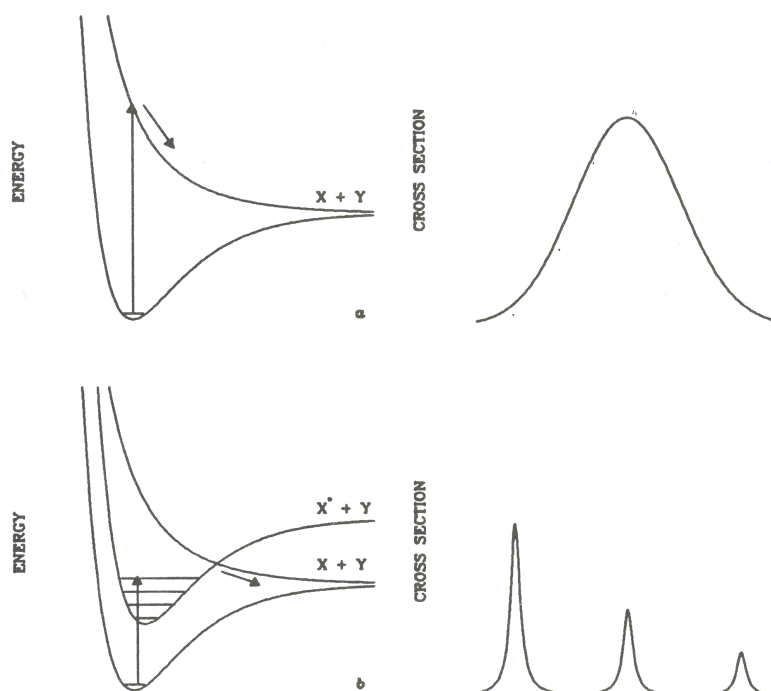


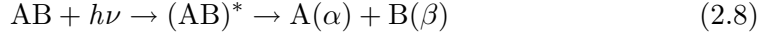
Figure 2.3 Graphical sketch of the direct photodissociation and predissociation processes.

region of maximum effect from the transition moments will play a less important role as the overlap decreases at the shorter relative distances sampled at higher collision energies.

## 2.2 Dynamics of photodissociation processes

---

Photodissociation is the dominant removal process of molecules in any region exposed to intense ultraviolet radiation, this includes diffuse and translucent interstellar clouds, dense photon-dominated regions, high velocity shocks, the surface layers of protoplanetary disks, and cometary and exoplanetary atmospheres. Photodissociation induced by the absorption of single photons permits the detailed study of molecular dynamics such as the breaking of bonds, internal energy transfer and radiationless transitions. Photodissociation ultimately involves a transition onto the repulsive part of a molecular potential curve at energies above the dissociation limit of that state. The photon energy is converted into internal energy of the molecule and if the transferred energy exceeds the binding energy the molecule will break apart. Let consider the dissociation of a molecule  $AB$  into products  $A$  and  $B$ , where  $A$  and  $B$  represent either structureless atoms with internal degrees of freedom of their own



where  $h\nu$  is the energy of one photon with frequency  $\nu$ ,  $(AB)^*$  represents the excited complex before it breaks apart and the labels  $\alpha$  and  $\beta$  specify the particular internal quantum states of the newborn products. The first step indicates absorption of the photons by the molecule and the second step represents the fragmentation of the excited complex.

Dissociation energies vary from a few thousandths of an eV for physically bound van der Waals molecules to several eV for chemically bound molecules. Van der Waals molecules can be fragmented with infrared (IR) photons whereas the fission of a chemical bond requires either a single ultraviolet (UV) or many IR photons.

There are several different dissociating processes which are distinguished by the way in which the dissociating transition occurs [5–9]. The simplest dissociation pathway is through photon absorption into an excited electronic state of the molecule which is unbound with respect to nuclear motion as shown by the upper panel of figure 2.3. The same effect is achieved if the transition occurs onto the repulsive wall above the dissociation limit of a bound molecular state. Rather than re-radiating the photon, the molecule falls apart, creating atoms or fragment species which may be electronically excited or may have excess kinetic energy. The direct photodissociation cross section, as shown in figure 2.3, is continuous as a function of photon energy. The energy dependence of the cross section is governed to first approximation by the Franck-Condon principle, in that the maximum value lies near the vertical excitation energy indicated by the arrow in figure 2.3.

In contrast to direct photodissociation in which photon absorption is continuous, taking place over a range of wavelengths, the indirect photodissociation processes are initiated by line absorption to bound vibrational levels of an excited electronic state. In the case of predissociation a bound excited electronic state is crossed by a third state which is unbound with respect to nuclear motion. The molecule undergoes a radiationless transition and dissociates (lower panel of figure 2.3).

Experimental measurements of photodissociation cross sections and rates for molecules of astrophysical interest are often difficult to make. A number of these molecules are not easy to produce in the laboratory and their photodissociation continua may exist in spectral regions difficult to observe or may be obscured by other stronger absorption features. Most of the cross sections and rate constants used in modeling astronomical environments must be calculated theoretically.

The state-to-state absorption cross section,  $\sigma_{n'J'}(\nu)$ , which describe the molecular dissociation via eq. 2.8, are calculated using the following relation [9]

$$\sigma_{n'J'}(\nu) = \frac{4}{3} \frac{\pi^2}{c} \sum_J \nu S_{JJ'} M_{n'J',EJ}^2 \quad (2.9)$$

where all quantities have already been defined in the previous section. Within the Local Thermodynamic Equilibrium (LTE) scheme the cumulative cross sections can then be obtained by further averaging over a Boltzmann distribution of the molecular states for a given gas temperature  $T_g$  at the selected absorption photon frequency  $\nu$ , as given by the following equation:

$$\sigma(\nu, T_g) = \sum_{n'J'} \sigma_{n'J'}(\nu) p_{n'J'}(T_g) \quad (2.10)$$

where  $p_{n'J'}$  are the probabilities to find the initial, bound molecular ion in the state  $n'J'$  defined as:

$$p_{n'J'}(T_g) = \frac{(2J' + 1) \exp(-\varepsilon_{n'J'}/\kappa T_g)}{\sum_{n'J'} (2J' + 1) \exp(-\varepsilon_{n'J'}/\kappa T_g)}. \quad (2.11)$$

The next step in the calculations now involves knowledge of the absorption rate coefficients for a selected black-body temperature  $T_b$ . It can be obtained from the following convolution over a density-weighted photon distribution [10]:

$$k(T_b) = c \int_{\nu_{th}}^{\infty} \sigma(\nu, T_g) f(\nu, T_b) d\nu \quad (2.12)$$

where  $\nu_{th}$  is the threshold frequency for the process,  $c$  is the speed of light, and  $f(\nu, T_b)$  is the photon density per unit frequency [11]:

$$f(\nu, T_b) = \frac{4\pi}{c} \frac{I(\nu)}{h\nu} \quad (2.13)$$

where  $I(\nu)$  has been defined in eq. 2.6.



# Bibliography

- [1] Schadee A., J. Quant. Spectrosc. Radiat. Transfer, **19**, 451, 1978
- [2] Gianturco F. A. and Gori Giorgi P., Phys. Rev. A., **54**, 1, 1996
- [3] Babb J. F., and Dalgarno A., Phys. Rev. A, **51**, 3021, 1995
- [4] Stancil P. C., and Dalgarno A., ApJ, **479**, 543, 1997
- [5] Shinke R., "Photodissociation dynamics", Cambridge University Press, 1993
- [6] van Dishoeck E. F., Jonkheid B., van Hemert M. C., Faraday Discussion, **133**, 231, 2006
- [7] van Dishoeck E. F., Black J. H., ApJ, **334**, 771, 1988
- [8] van Dishoeck E. F., Visser R., to appear in "Modern Concept in Laboratory Astrochemistry", eds. S. Shlemmer, H. Mutschke and Th. Giesen, Springer, 2011
- [9] Kirby K. P., and Van Dishoeck E. F., Adv. At. Mol. Phys., **25**, 437, 1988
- [10] Black J., and Dalgarno A., ApJS, **34**, 405, 1977
- [11] Draine B. T., "Physics of the interstellar and intergalactic medium", Princeton University Press, 2011



*I went down Virginia  
Seekin' shelter from the storm  
Caught up in the fable  
I watched the tower grow*

# 3

## The theory of reactive scattering

One of the major triumphs of theoretical/computational science has been the development of reactive scattering theory for describing simple gas phase chemical reactions from first principle. On the other hand the first studies on simple reactions showed that studying reactive collisions is a challenge due to the difficult nature of the partial differential equations and associated boundary conditions that are involved. Exact quantum scattering calculations involve both the solution of time independent (TI) or time dependent (TD) Schrödinger equation. The most detailed calculations on differential cross sections for atom-diatom reactions have been obtained in recent years using the hyperspherical method. Due to the nature and size of such coupled equations their solutions are very demanding computationally and reduced dimensionality theories have been proposed and applied, in which close-coupling expansions and the other degrees of freedom are treated approximatively. In this chapter I introduce the hyperspherical approach and some of the reduced dimensionality methods employed in our calculations.

### 3.1 The exact reactive scattering approach

---

#### 3.1.1 The hyperspherical method

The basic idea in the hyperspherical coordinate approach is to transform the reactive scattering problem into a nonreactive-like scattering problem. This is achieved by defining a new set of coordinates called hyperspherical coordinates which consists of a hyperradius  $\rho$  and several hyperspherical angles. The hyperradius  $\rho$  serves as a scattering coordinates that is arrangement-independent while the hyperspherical angles make up the rest of coordinates. In the limit  $\rho \rightarrow \infty$ , the scattering wavefunction can reach all the asymptotic arrangements as the hyperspherical angles sweep through the coordinate space. Thus, one only has to deal with a single continuous scattering coordinate  $\rho$  and the reactive scattering problem formally becomes as inelastic scattering problem in terms of the hyperspherical coordinates.

The hyperspherical coordinates are conveniently defined in terms of the mass-scaled Jacobi coordinates (fig. 3.1). For a triatomic system with atomic masses  $m_\tau$  ( $\tau = A, B, C$ ) the corresponding *mass-scaled* Jacobi coordinates are simply [1–10]:

$$\mathbf{S}_\tau = d_\tau \mathbf{R}_\tau, \quad \mathbf{s}_\tau = d_\tau^{-1} \mathbf{r}_\tau \quad (3.1)$$

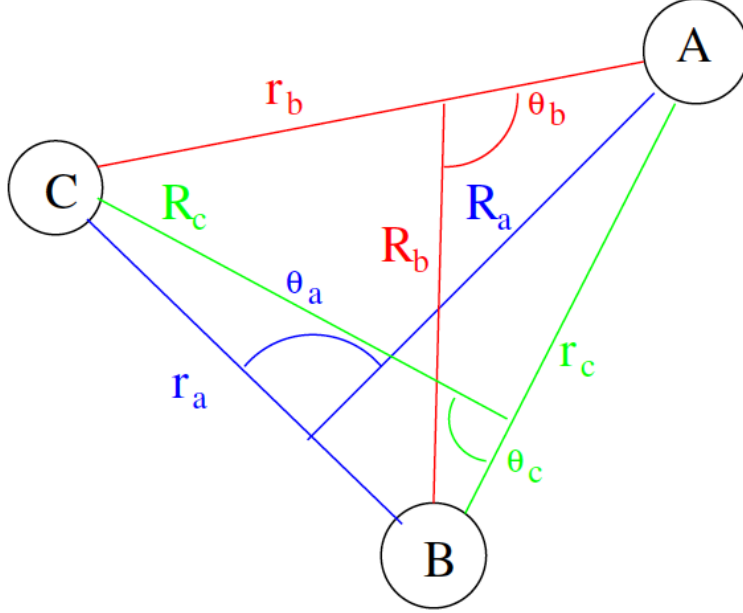


Figure 3.1 Set of Jacobi coordinates for a triatomic system.

where the  $d_\tau$  are the dimensionless scaling factors

$$d_\tau = \left[ \frac{m_\tau}{\mu} \left( 1 - \frac{m_\tau}{M} \right) \right]^{1/2}. \quad (3.2)$$

Here  $\mu$  is a three-body reduced mass,

$$\mu = \left[ \frac{m_A m_B m_C}{M} \right]^{1/2} \quad (3.3)$$

and  $M$  is the total mass of the system

$$M = m_A + m_B + m_C \quad (3.4)$$

It is easy to see from the definitions of the mass-scaled Jacobi coordinates that the kinetic energy operator can be written as [1–3]

$$T = -\frac{\hbar^2}{2\mu} (\nabla_{s_\tau}^2 + \nabla_{s_\tau}^2) \quad (3.5)$$

The coordinate transformation relations between different arrangements are simply kinematic rotations [1, 2],

$$\begin{pmatrix} \mathbf{S}_\zeta \\ \mathbf{s}_\zeta \end{pmatrix} = \begin{pmatrix} \cos(\chi_{\zeta\tau}) \mathbf{1} & \sin(\chi_{\zeta\tau}) \mathbf{1} \\ -\sin(\chi_{\zeta\tau}) \mathbf{1} & \cos(\chi_{\zeta\tau}) \mathbf{1} \end{pmatrix} \begin{pmatrix} \mathbf{S}_\tau \\ \mathbf{s}_\tau \end{pmatrix} \quad (3.6)$$

where  $\mathbf{1}$  is the  $3 \times 3$  unit matrix. This transformation between arrangements is orthogonal, it is equivalent to a rotation in a plane containing the vectors  $\mathbf{S}_\tau$  and  $\mathbf{s}_\tau$ . Thus we obtain the invariant relation [7, 8]

$$\rho = \sqrt{\mathbf{S}_\tau^2 + \mathbf{s}_\tau^2} \quad (3.7)$$

a quantity which is independent of rearrangement.

The main feature of the hyperspherical coordinate method holds in this properties of the hyperradius that allows one to formally transform a reactive scattering problem into an inelastic one with a well defined single scattering coordinate  $\rho$ . The rest of the hyperspherical coordinates describe the bound motions of the molecular system and are called hyperspherical angles

$$\theta_{D_\tau} = \tan^{-1}(s_\tau/S_\tau) \quad (3.8)$$

and the four Euler angles. Using  $(\rho, \theta_{D_\tau}, \Theta_\tau)$  as three internal coordinates the Hamiltonian of the atom-diatom system can be written as

$$H = -\frac{\hbar^2}{2\mu\rho^5} \frac{\partial}{\partial\rho} \rho^5 \frac{\partial}{\partial\rho} + \frac{\Delta^2}{2\mu\rho^2} + V(\rho, \theta_{D_\tau}, \Theta_\tau) \quad (3.9)$$

where  $\Delta^2$ , given by

$$\Delta^2 = -\frac{\hbar^2}{\sin^2 2\theta_{D_\tau}} \frac{\partial}{\partial\theta_{D_\tau}} \sin^2 2\theta_{D_\tau} \frac{\partial}{\partial\theta_{D_\tau}} + \frac{L_\tau^2}{\cos^2 \theta_{D_\tau}} + \frac{J_\tau^2}{\sin^2 \theta_{D_\tau}}, \quad (3.10)$$

is the square of Smith's grand angular momentum [1] operator. The problem is solved as usually propagating the solution matrix in the scattering coordinate  $\rho$  from the origin outward to match the asymptotic boundary conditions for various arrangements. Since  $V(\rho, \theta_{D_\tau}, \Theta_\tau)$  changes rapidly with  $\rho$ , the propagation range is divided into "sectors" and within each sector the local eigenfunctions are calculated. The matching to asymptotic states is usually accompanied by a coordinate transformation from the hyperspherical coordinates to the appropriate Jacobi coordinates because the hyperspherical coordinates are not the correct one to represent the asymptotic wavefunction.

The code which solve the coupled-channel problem in the hyperspherical coordinate approach has been developed in 2000 by Manolopoulos and co-workers [11]. The ABC code is able to treat a single-surface problem and has been tested, over the years, for a large number of reactions [12–18]. The quantum reactive scattering boundary conditions are applied exactly and the coupling between the initial and final orbital and rotational angular momenta is also implemented correctly for each value of the total angular momentum. In each separate run of the ABC program, the reactive scattering Schrödinger equation is solved for a specified values of the total angular momentum quantum number  $J$  and the triatomic parity eigenvalue  $P$ , and in the case of homonuclear molecular partners for a specified value of the diatomic parity eigenvalue  $p$ . The resulting output files contain parity-adapted scattering matrix elements of the form  $S_{nn'}^{J,P}(E)$ , where  $n$  and  $n'$  are composite indices for  $\alpha\nu jk$  and  $\alpha'\nu'j'k'$ , being  $\alpha$  and  $\alpha'$  two different arrangements, and  $\nu j$  and  $\nu' j'$  the roto-vibrational states of the molecules in its reagent or product arrangements.

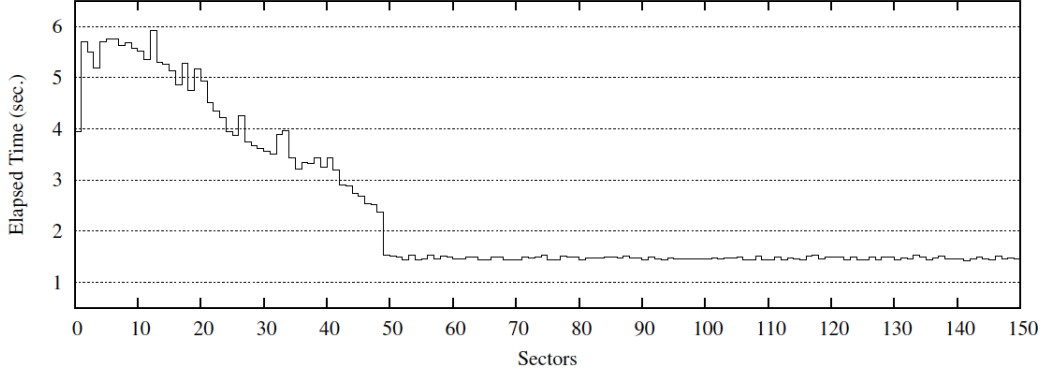


Figure 3.2 Execution time spent by ABC program in each sector

### 3.1.2 ABC program: overview and limits

In the ABC program the integration of Schrödinger equation is performed by dividing into  $n$  sectors the considered range of  $\rho$  values. Within each sector the basis functions  $B_{avj,k}^{JM}$  are computed, and the solution matrix of the expansion coefficients is propagated through all the sectors, from the origin of  $\rho$  up to its asymptotic value (where the wavefunction dependence on  $\rho$  has the form of a planar wave). Finally, under these conditions the value of the  $S$  matrix elements is worked out. At this point the state-to-state scattering probability elements of matrix  $P$ , whose elements are the quadratic module of the corresponding  $S$  matrix elements is determined for an arbitrarily fine grid of  $N$  values of the total energy  $E$ . Most often observable properties are the results of averaging over energies, total angular momenta, quantum states, which means that ABC runs need to be repeated a large number of times.

The limits of ABC code are mainly due to the significant CPU demand which strongly depends on the input parameters. For example, one fixed energy execution of the ABC code can take about 10 hours on a single CPU.

In the calculation steps one, then, should consider various challenges:

- the dimension of the basis set that can be very large in the case of ionic processes
- the number of runs needed to obtain converged cross sections
- the computational cost of one run which could explode.

These problems have partially been tackled and different solutions have been proposed. The implementation of ABC workflow in the Multi-Grid installation of the P-GRADE Portal [19] allowed to execute different input files simultaneously but no gain in the final elapsed time has been made. This implementation, in fact, gives only the possibility of running the ABC code for different sets of parameters during the same time.

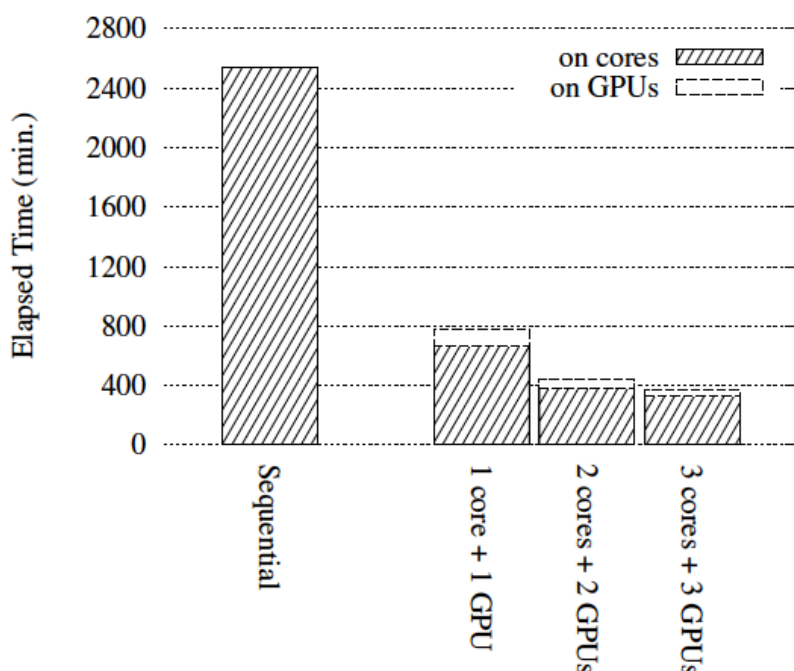


Figure 3.3 Comparison between serial elapsed time and ABC-GPU program version elapsed time.

With the developing of the innovative GPU architectures a new era of the computer sciences began. Baraglia et al. [20] implemented quantum reactive scattering simulations exploiting in combination CPUs and GPUs. Since ABC is made of blocks of recursive sequences of linear algebra matrix operations this step is the only one, at the moment, that improved the cost effective of such calculations. As shown by figure 3.2 the execution time decreases as the channels become less coupled down to a constant value when the channels are completely de-coupled. The percentage of the time spent elaborating matrix operations is about 75 % (summation and multiplications on matrices and inversion matrix: DGEMM and SYMINV LAPACK routines). Implementing a parallel version of DGEMM for GPU (cuBLAS library) permitted them to significantly reduce the ABC program execution time with a speed-up of 4.0 (see figure 3.3).

Nevertheless, an accurate study with the ABC code require very long time and a large number of available computing resources on these new GPU-clusters. If we consider the execution time given in the Baraglia's paper for a single run ( $\sim 13$  hours) and multiply this for a typical dimension of a reactive problem (a given number of  $J$  and a given number of roto-vibrational states) the total time needed for an accurate study is approximatively six months! If we add to this total time the physical limit of the code when studying ion-molecule processes which requires a very huge adiabatic

basis set then it is clear that approximate method (in our own case where only the total final destruction rate is needed and no state-to-state or angular distribution studies are required) are certainly more useful and reasonable.

In the next section I will describe some of the most known approximation introduced over the years for the study of reactive scattering aimed at the dimensionality-reduction and to a less expensive computational cost.

### 3.2 The reduced dimensionality methods

---

Over the past decade several approximate theories of reactive scattering have been developed in which some of the degrees of freedom are decoupled. These methods are called *reduced dimensionality* methods to emphasize the reduction in treating all degrees of freedom exactly. Two theories that have been used extensively also in the inelastic processes treatment involve the internal angular motion of a triatomic system in atom-diatom reactions and led to the sudden and adiabatic approximations. The sudden theory assumes that motion is "frozen" throughout the collision, whereas the adiabatic theory assumes it changes but with preservation of the bending quantum number.

Finally, the most widely used example of the reduced dimensionality approach is termed *J*-shifting.

#### 3.2.1 *J*-shifting approximation

An exact treatment of overall rotation scales nonlinearly with the total angular momentum quantum number  $J$  (as much as  $O(J^6)$ ). Thus for observables, such as the reaction cross section and rate constant, for which values of  $J$  up to several hundred or more are typical, this results in a huge increase in computational effort relative to a  $J = 0$  calculation.

The *J*-shifting approximation was introduced some years ago [21, 22] to circumvent this bottleneck by simply shifting the collision energy in the probability for zero total angular momentum ( $J = 0$ ). Let's  $P^J(E)$  the reaction probability at a fixed total angular momentum  $J$ , the *J*-shifting method gives the approximate value for the reaction probability by employing the approximation

$$P^J(E) \approx P^{J=0}(E - B^\ddagger J(J+1)), \quad (3.11)$$

where  $P^{J=0}(E)$  is the reaction probability for the zero total angular momentum ( $J = 0$ ). In the simplest approach, the shifting constant  $B^\ddagger$  is obtained by evaluating the rotation constant of the collision complex at some perceived transition state.

Of course the equation 3.11 is based on the assumption of separation of overall rotation of the collision system from the reaction dynamics. Physically, it asserts that the  $3N-6$  vibrational degrees of freedom are of paramount importance in the reaction dynamics and the overall rotation is of relatively minor importance, serving mainly as a "sink" for some of the total energy. In this approximation the rate constant is approximatively given by



$$\alpha(T) = \frac{k_B T}{B^\ddagger} \alpha^{J=0}(T) \quad (3.12)$$

Equation 3.12 shows that the standard  $J$ -shifting method yields a rate constant that is inversely proportional to the shifting constant  $B^\ddagger$ . As a result, the rate constant calculated from the standard  $J$ -shifting approximation could not in general be uniformly accurate at all temperatures.

The  $J$ -shifting approximation has been tested and applied to reactions with simple barriers. In general its accuracy for the thermal rate constant is in the 10-20% range.

There are two main deficiencies associated with the standard  $J$ -shifting approach and its variants (that we shall not describe). Firstly, the determination of the shifting constant  $B^\ddagger$  is to some extent arbitrary, and consequently, the compute rate constant has numerical uncertainties associated with it. Secondly, it is impossible in general to obtain a uniformly accurate rate constant at all temperatures by applying the standard  $J$ -shifting approach with a fixed shifting constant  $B^\ddagger$ . Other variants of this approximation have been proposed but shall not be delved in this section .

### 3.2.2 Coupled states approximation

For a triatomic molecule, there are total of three sets of Jacobi coordinates. In terms of anyone of the three sets such as the one shown in fig. 3.1, the kinetic energy operator is diagonal, and the triatomic Hamiltonian (in atomic units) is given by the following

$$\hat{H} = -\frac{1}{2\mu} \nabla_R^2 + \frac{\hat{L}^2}{2\mu R^2} - \frac{1}{2m} \nabla_r^2 + \frac{\hat{j}^2}{2mr^2} + \hat{V}(r, R, \vartheta) \quad (3.13)$$

where  $\hat{L}$  and  $\hat{j}$  are, respectively, the orbital and diatomic angular momentum operators. Here the reduced masses are defined by

$$m = \frac{m_B m_C}{m_B + m_C} \quad (3.14)$$

$$\mu = \frac{m_A(m_B + m_C)}{m_A + m_B + m_C} \quad (3.15)$$

Since the total angular momentum  $\hat{J} = \hat{L} + \hat{j}$  is conserved, we can use an angular momentum basis in the coupled-angular momentum representations to expand the wavefunction. There are two equivalent and widely used representations; the space-fixed (SFF) or body-fixed (BF) representation. In the SF representation, the basis functions are eigenfunctions of  $(J^2, J_Z, j^2, L^2)$  operators where  $J_Z$  is the projection of  $J$  along the space-fixed Z-axis. In the BF representation, the basis functions chosen are eigenfunctions of  $(J^2, J_Z, j^2, J_z)$  operators where  $L^2$  is replaced by the projection of  $J$  along the body-fixed  $z$  axis. Usually, the body-fixed  $z$  axis is the same as that of  $j$  because  $L$  has zero projection along the  $R$  axis.

The orbital angular momentum is expressed

$$L^2 = (J - j)^2 = J^2 + j^2 - 2J_z j_z - J_+ j_- - J_- j_+ \quad (3.16)$$

where the various angular momentum operators are defined in the BF frame. The operator  $L^2$  is composed of a part which is diagonal in the  $\Omega$  and a part which is not

$$[L^2]_{\Omega\Omega} = J(J+1) + j(j+1) - 2\Omega^2 \quad (3.17)$$

and

$$[L^2]_{\Omega\Omega'} = -\delta_{\Omega'\Omega\pm 1}[(J \pm \Omega + 1)(J \mp \Omega)]^{1/2} j_{\mp} \quad (3.18)$$

Here,  $j_{\mp}$  are the raising (+) and lowering (-) operators for the rotator,  $\Omega$  is the projection of  $J$  along the BF  $z$ -axis, and  $J$  is the total angular momentum quantum number.

Within the CS approximation [23–27] the orbital angular momentum operator  $\hat{L}^2$  is assumed to be equal to  $\hat{J}^2 + \hat{j}^2 - 2\hat{J}_z\hat{j}_z$ . In this way the coupling between different projections of the rotational angular momentum  $\Omega$  along the body-fixed axis, represented by eq. 3.18 is neglected, reducing the dimensionality of the problem. Thus, the CS approximation works extremely well for  $j = 0$  as the initial and/or the final state. In the rotating frame, the potential is found to be rigorously diagonal in  $\Omega$  so that neglecting the off-diagonal  $\Omega$  coupling in  $L^2$ , a drastic reduction in the number of states coupled was achieved. The reduction in the number of coupled equations resulting is a square root, so that for a collision with 10000 coupled channels arising from a given vibration-rotation manifold, only 100 coupled states arise. Such a procedure thus completely transforms totally impossible problems to ones amenable to solution with presently existing close-coupling algorithms.

### 3.3 The Negative Imaginary Potential method

---

Since the first paper of Baer et al. [28] introducing the use of negative imaginary potentials, many different versions of this method have been proposed [29,30]. All of them combine inelastic scattering calculations and the presence of a negative imaginary potential (NIP) which "absorbs" the reactive flux into the product channels or defines the initial conditions of the propagation as in the case of the adiabatic capture method proposed by Rackham et al. [31]. The main advantage of this approach stems on the fact that the close-coupling calculations simplify basically to an inelastic scattering calculation. Since, reactive flux is absorbed fairly near to the strong interaction region, one solves the problem considering only one (although somewhat perturbed) rearrangement channel. On the other hand, the method, as originally formulated, is only capable of providing total reaction S-matrix elements and the calculation becomes more complicated since complex algebra must be then considered. Nevertheless, this approximated method is the most powerful and feasible one that we can use to obtain the total reactive rate coefficients for astrochemical reactions in a reasonable computational time and with good accuracy.

Our theoretical approach follows the Baer's original work under the coupled states approximation discussed in the previous section.

### 3.3.1 Theoretical approach

We start by solving the usual Schrödinger equation:

$$\hat{H}\Psi^{J,\Omega}(R, r, \vartheta) = E\Psi^{J,\Omega}(R, r, \vartheta) \quad (3.19)$$

with  $R$ ,  $r$ , and  $\vartheta$ , being the Jacobi coordinates. As shown in the section 3.2.2 the employing of a CS approximation is a powerful approach to study reactive scattering processes reducing the dimensionality of the problem. We shall show below that, in the present context, such simplified angular momentum couplings plays a limited role in comparison with full coupled-channel (CC) calculations. The Hamiltonian of the triatomic system in the Body Fixed (BF) frame, within CS approximation, reads:

$$\hat{H} = -\frac{1}{2\mu}\nabla_R^2 + \frac{\hat{J}^2 + \hat{j}^2 - 2\hat{J}_z\hat{j}_z}{2\mu R^2} - \frac{1}{2m}\nabla_r^2 + \frac{\hat{j}^2}{2mr^2} + \hat{V}(r, R, \vartheta) + \hat{V}^{NIP}(r, R, \vartheta) \quad (3.20)$$

where  $\mu$  and  $m$  are respectively the triatomic and diatomic reduced masses as defined by eq.s 3.15 and 3.14,  $\hat{V}(r, R, \vartheta)$  is the interaction potential operator, and  $\hat{V}^{NIP}(r, R, \vartheta)$  represents the absorbing negative imaginary potential. Several model forms of NIP have been proposed over the years [32–35], one of the most usual being given by a monomial of order  $n$ :

$$\hat{V}^{NIP}(r, R, \vartheta) = -iu_0 \left[ \frac{r - r_{min}}{r_{max} - r_{min}} \right]^n \quad r_{min} \leq r \leq r_{max} \quad (3.21)$$

where the range of  $R$  is unlimited and the parameter  $u_0(\gamma)$  must fulfill the conditions:

$$\frac{E^{1/2}}{\Delta r \sqrt{8\mu}} \ll u_0 \ll \Delta r \sqrt{8\mu} E^{3/2} \quad (3.22)$$

with  $\Delta r = r_{max} - r_{min}$  and  $E$  being the collision energy in the product arrangement. The left-hand inequality guarantees that all the flux entering the range of the NIP potential will be absorbed and the right-hand one guarantees that no artificial reflection takes place due to the early interaction of the wave function with the imaginary potential.

In order to solve the equation (3.19) we divide the range of integration over the  $R$  coordinate into  $N$  sectors. At the mid-point ( $\bar{R}_k$ ) of each sector the total wave function  $\Psi^{J,\Omega}(r, R, \vartheta)$  is expanded over a local roto-vibrational adiabatic basis-set (RVABS):

$$\Psi_a^{J,\Omega}(r, R, \vartheta) = \sum_a G_a^{J,\Omega}(R) \varphi_a(r, \vartheta; \bar{R}_k) Y_J^\Omega(\vartheta, \phi) \quad (3.23)$$

where the subscript "a" is a collective index which indicates a selected roto-vibrational state of the target molecule. The local roto-vibrational adiabatic basis-set is thus constructed by solving the following molecular Schrödinger equation:

$$\hat{h}_{\bar{R}_k} \varphi_a(r, \vartheta; \bar{R}_k) = \varepsilon_a \varphi_a(r, \vartheta; \bar{R}_k) \quad (3.24)$$

where:

$$\hat{h}_{\bar{R}_k} = -\frac{1}{2m}\nabla_r^2 + \frac{\hat{j}^2}{2mr^2} + \hat{V}(r, \vartheta; \bar{R}_k) \quad (3.25)$$

A discrete variable representation (DVR) method based on the Colbert and Miller paper [36] for the "r" coordinate is chosen to represent the vibrational functions  $\chi_i(r)$ , while the angular degrees of freedom are fully accounted by the expansion over the spherical harmonics  $Y_j^\Omega(\vartheta, \phi)$

$$\varphi_a(r, \vartheta; \bar{R}_k) = \sum_j Y_j^\Omega(\vartheta, \phi) \sum_i^{n_{dvr}} c_{ij}^a \chi_i(r) \quad (3.26)$$

For simplicity in the mathematics of the problem is preferable to use the Dirac notation

$$|\varphi_a\rangle = \sum_j^{j_{max}} |j\Omega\rangle \sum_i^{n_{dvr}} c_{ij}^a |i\rangle. \quad (3.27)$$

The three-dimensional potential  $\hat{V}(r, \vartheta; \bar{R}_k)$  is expanded, as usually, in Legendre polynomial

$$V(r, \vartheta, \bar{R}_k) = \sum_\lambda V_\lambda(r, \bar{R}_k) P_\lambda(\cos \vartheta) \quad (3.28)$$

then the matrix elements of the intermolecular potential take the form

$$\{V_{ij, i'j'}\}_{ab} = \sum_\lambda \langle j'\Omega | P_\lambda(\cos \vartheta) | j\Omega \rangle \langle i' | V_\lambda(r) | i \rangle \quad (3.29)$$

$$= \sum_\lambda f_\lambda(j\Omega, j'\Omega) V_\lambda^{ii'}(b, a, r_i) \quad (3.30)$$

where the  $f_\lambda(j'\Omega, j\Omega)$  are the Percival-Seaton coefficients, analytically known in terms of 3-j coefficients

$$f_\lambda(j'\Omega, j\Omega) = (-)^\Omega [(2j+1)(2j'+1)]^{1/2} \begin{pmatrix} j & \lambda & j' \\ 0 & 0 & 0 \end{pmatrix} \begin{pmatrix} j & \lambda & j' \\ -\Omega & 0 & \Omega \end{pmatrix} \quad (3.31)$$

Once we obtained the molecular eigenfunctions  $\varphi_a$  and their eigenvalues  $\varepsilon_a$ , we can construct the total wave-function  $\Psi_a^{J,\Omega}$  (eq. 3.23). The  $G_a^{J,\Omega}(R)$  coefficients in the expansion 3.23 are the solution functions needed to obtain the scattering observables we are interested in. By applying the total hamiltonian 3.20 to the total wave-function 3.23 leads to the usual coupling matrix

$$\begin{aligned} \{W(\bar{R}_k)\}_{ab} = 2\mu \{U(\bar{R}_k)\}_{ab} = \delta_{ab} & \left[ \frac{J(J+1) - 2\Omega^2}{\bar{R}_k^2} - k_a^2(\bar{R}_k) \right] \\ & + \frac{1}{\bar{R}_k^2} \{\hat{j}^2\}_{ab} + 2\mu \{\hat{V}^{NIP}\}_{ab} \end{aligned} \quad (3.32)$$

with

$$k_a^2 = \frac{2\mu}{\hbar^2} (E - \varepsilon_a) \quad (3.33)$$

The  $\{\hat{j}^2\}_{ab}$  and  $\{\hat{V}^{NIP}\}_{ab}$  coupling elements can be explicitly written as following

$$\{\hat{j}^2\}_{ab} = \sum_{jj'}^{j_{max}} \sum_{ii'}^{n_{dvr}} \delta_{ii'} c_{ij'}^{*b} c_{ij}^a \langle j' \Omega | \hat{j}^2 | j \Omega \rangle \quad (3.34)$$

and

$$\{\hat{V}^{NIP}\}_{ab} = \sum_{jj'}^{j_{max}} \sum_{ii'}^{n_{dvr}} \delta_{ii'} \delta_{jj'} c_{ij'}^{*b} c_{ij}^a V^{NIP}(r_i) \quad (3.35)$$

where we have considered an expansion over the Legendre polynomial also for the absorbing potential  $V^{NIP}(r, \theta) = V^{NIP}(r) P_0(\cos \theta)$ .

The above formulation describes the NIP-RVABS treatment of the present reactive modelling of the quantum dynamics.

It is worth noting that the presence of the  $V^{NIP}$  makes the coupling matrix complex symmetric. The set of coupled equations that describes the scattering processes can be written in matrix notation as:

$$\frac{d^2}{dR^2} \mathbf{G}^{(k)}(R) = \mathbf{W}(\bar{R}_k) \mathbf{G}^{(k)}(R) \quad (3.36)$$

#### 3.3.2 Generalized R-matrix Propagation

The eq.s 3.36 are solved using the R-matrix method [37], which propagates the inverse logarithmic derivative of the solution:

$$\mathbf{R} = \mathbf{G} \mathbf{G}'^{-1}. \quad (3.37)$$

The R-matrix propagation is based on the construction of local (sector)  $R$  matrices which iteratively lead to the global final  $R$ -matrix; as mentioned in the previous section, the range of integration is divided into  $N$  sectors. At the center of each sector the value of the scattering coordinate is  $R = R_k$ , and its width is  $h_k$ . Assuming that the coupling matrix is constant within a sector, and diagonalizing it at the center of each sector, we eliminate all coupling in the differential equations, thereby obtaining a new local translational function  $F^{(k)}$  with complex eigenvalues  $\lambda$ :

$$(\mathbf{T}^{(k)})^{-1} \mathbf{W}(\bar{R}_k) \mathbf{T}^{(k)} = \lambda^2(k) \quad (3.38)$$

$$\mathbf{G}^{(k)}(R) \mathbf{T}^{(k)} = \mathbf{F}^{(k)}(R). \quad (3.39)$$

As already noted above, the presence of the NIP scheme introduces a complex algebra and the original R-matrix propagator [37] must be modified to take this feature into account. As also reported in [29], the transpose matrix  $(\mathbf{T}^{(k)})^\dagger$  is replaced by the inverse  $(\mathbf{T}^{(k)})^{-1}$  and the coupling matrix  $\mathbf{W}(\bar{R}_k)$  is no longer real symmetric. The assembling iterative algorithm is thus the following

$$\mathbf{R}^{(k)} = \mathbf{r}_4^{(k)} - \mathbf{r}_3^{(k)} \mathbf{Z}^{(k)} \mathbf{r}_2^{(k)} \quad (3.40)$$

which connects a new sector R-matrix,  $\mathbf{r}^{(k)}$ , to an old global R-matrix,  $\mathbf{R}^{(k-1)}$ , to give the new global  $\mathbf{R}^k$ , where

$$\mathbf{Z}^{(k)} = \left[ \mathbf{r}_1^{(k)} + \mathbf{Q}(k, k-1) \mathbf{R}^{(k-1)} \mathbf{Q}(k-1, k) \right]^{-1} \quad (3.41)$$

and the two  $\mathbf{Q}$ -matrices are expressed as:

$$\mathbf{Q}(k-1, k) = (\mathbf{T}^{(k-1)})^{-1} \mathbf{\Theta}(k-1, k) \mathbf{T}^{(k)} \quad (3.42)$$

$$\mathbf{Q}(k, k-1) = (\mathbf{T}^{(k)})^{-1} \mathbf{\Theta}^T(k-1, k) \mathbf{T}^{(k-1)} \quad (3.43)$$

The  $\mathbf{Q}(k-1, k)$  and  $\mathbf{Q}(k, k-1)$  matrices take into account fully the basis set evolution between sectors ensuring the continuity of the solution matrix during the propagation. In the eq.s 3.42 and 3.43  $\mathbf{\Theta}(k-1, k)$  is the overlapping matrix between functions at the boundary of two different sectors defined as

$$\{\mathbf{\Theta}(k-1, k)\}_{ab} = \int_{\vartheta} \int_r \varphi_a^*(r, \vartheta; \bar{R}_{k-1}) \varphi_b(r, \vartheta; \bar{R}_k) \sin \vartheta d\vartheta dr \quad (3.44)$$

and the local sector matrices are

$$\left\{ \mathbf{r}_1^{(k)} \right\}_{ab} = \left\{ \mathbf{r}_4^{(k)} \right\}_{ab} = \delta_{ab} \frac{1}{\lambda_a} \frac{e^{\lambda_a h_k} + e^{-\lambda_a h_k}}{e^{\lambda_a h_k} - e^{-\lambda_a h_k}} \quad (3.45)$$

$$\left\{ \mathbf{r}_2^{(k)} \right\}_{ab} = \left\{ \mathbf{r}_3^{(k)} \right\}_{ab} = \delta_{ab} \frac{1}{\lambda_a} \frac{2}{e^{\lambda_a h_k} - e^{-\lambda_a h_k}} \quad (3.46)$$

As in any numerical problem involving a propagator, an initial condition is needed. Here it is given as

$$\left\{ \mathbf{R}^{(1)} \right\}_{ab} = \delta_{ab} \frac{1}{\lambda_a}. \quad (3.47)$$

The initial value R-matrix is then propagated using the algorithm sketched above, up to the numerical asymptotic region where the final  $\mathbf{R}$ -matrix is obtained from the following transformation:

$$\mathbf{R} = \mathbf{T}^{(N)} \mathbf{R}^{(N)} (\mathbf{T}^{(N)})^{-1} \quad (3.48)$$

### 3.3.3 Asymptotic Matching

At the end of propagation the scattering information is extracted, as usual, by the asymptotic matching conditions. We first obtain the  $\mathbf{K}$ -matrix from the final  $\mathbf{R}$ -matrix:

$$(\mathbf{R}\mathbf{N}' - \mathbf{N}) \mathbf{K} = (\mathbf{R}\mathbf{J}' - \mathbf{J}) \quad (3.49)$$

where  $\mathbf{J}$  and  $\mathbf{N}$  are the well known Riccati-Bessel and Riccati-Neumann matrices [38] given, for open channels, by the following eq.s:

$$\{\mathbf{J}\}_{ab} = \frac{1}{\sqrt{k_a}} \sin(k_a R_{end}) \quad (3.50)$$

$$\{\mathbf{N}\}_{ab} = -\delta_{ab} \frac{1}{\sqrt{k_a}} \cos(k_a R_{end}). \quad (3.51)$$

The corresponding relations for closed channels are:

$$\{\mathbf{J}\}_{ab} = \delta_{ab} \frac{1}{\sqrt{2\pi k_a}} \left(1 - e^{-2k_a R_{end}}\right) \quad (3.52)$$

$$\{\mathbf{N}\}_{ab} = -\delta_{ab} \sqrt{\frac{\pi}{2k_a}}. \quad (3.53)$$

The final scattering matrix  $\mathbf{S}$  is obtained as

$$\mathbf{S} = (\mathbf{I} + i\mathbf{K})(\mathbf{I} - i\mathbf{K})^{-1} \quad (3.54)$$

Because of the flux-absorbing effect of the NIP, the resulting final  $\mathbf{S}$ -matrix is non unitary and its default to unitarity is the (state-to-all) reaction probability:

$$P_{(a \rightarrow all)}^{J\Omega} = 1 - \sum_b |S_{ab}^{J\Omega}|^2 \quad (3.55)$$

From the reaction probability one can in turn obtain the reactive cross section

$$\sigma_{(a \rightarrow all)}(E) = \frac{\pi}{(2j_a + 1)k_a^2} \sum_J \sum_{\Omega} (2J + 1) P_{a \rightarrow all}^{J\Omega} \quad (3.56)$$

and then the rate coefficients

$$\alpha(T) = \left(\frac{8k_B T}{\pi \mu}\right)^{1/2} \frac{1}{(k_B T)^2} \int_0^{\infty} \sigma_{a \rightarrow all}(E) \exp(-E/k_B T) E dE \quad (3.57)$$





# Bibliography

- [1] Smith F. T., J. Chem. Phys., **21**, 1352, 1959
- [2] Smith F. T., Phys. Rev., **120**, 1058, 1960
- [3] Hirschfelder J. O., and Dahler J. S., Proc. Natl. Acad. Sci., **42**, 363, 1956
- [4] Hirschfelder J. O., Int. J. Quantum Chem. Symp., **3**, 17, 1969
- [5] Yang K. H., Hirschfelder J. O., and Johnson B. R., J. Chem. Phys., **75**, 2321, 1981
- [6] Smith F. T., J. Math. Phys., **3**, 735, 1962
- [7] Delves L. M., Nucl. Phys., **9**, 391, 1951
- [8] Delves L. M., Nucl. Phys., **20**, 275, 1960
- [9] Johnson B. R., J. Chem. Phys., **73**, 5051, 1980
- [10] Johnson B. R., J. Chem. Phys., **79**, 1906, 1916, 1983
- [11] Skouteris D., Castillo J. F. and Manolopoulos D. E., Comp. Phys. Comm., **133**, 128, 2000
- [12] Millard A. H., Manolopoulos D. E., Werner H.-J., J. Chem. Phys., **113**, 11084, 2000
- [13] Balakrishnan N., Dalgarno A., Chem. Phys. Lett., **341**, 652, 2001
- [14] R. T. Skodje, D. Skouteris, D. E. Manolopoulos, S.-H. Lee, F. Dong, and K. Liu, Phys. Rev. Lett., **85**, 1206, 2000
- [15] Aoiz F. J. et al., Phys. Rev. Lett., **86**, 1729, 2001
- [16] Bodo E., Gianturco F. A., and Dalgarno A., J. Phys. B: At. Mol. Opt. Phys., **35**, 2391, 2002
- [17] Zhu C., Krems R., Dalgarno A., Balakrishnan N., ApJ, **577**, 795, 2002
- [18] Balakrishnan N., J. Chem. Phys., **119**, 195, 2003
- [19] Skouteris D., Costantini A., Laganá A., Gergely Sipos, Balaskó A., Kacsuk P., ICCSA (1), 1108, eds. Gervasi et al., Springer, 2008
- [20] Baraglia R., Bravi M., Capannini G., Lagan A., Zambonini E., ICCSA (3), 412, eds. Murgante et al., Springer, 2011
- [21] Qi J., and Bowman J. M., Chem. Phys. Lett., **276**, 371, 1997
- [22] Zhang D. H. and Zhang J. Z. H., J. Chem. Phys., **110**, 7622, 1999
- [23] McGuire P., Chem. Phys. Lett., **23**, 575, 1973

## BIBLIOGRAPHY

---

- [24] McGuire P., and Kouri D. J., J. Chem. Phys., **60**, 2488, 1974
- [25] Kouri D. J., and McGuire P., Chem. Phys. Lett., **29**, 414, 1974
- [26] McGuire P., Chem. Phys., **13**, 81, 1976
- [27] Pack R. T., and Parker G. A., J. Chem. Phys., **87**, 3888, 1987
- [28] Baer M., Ng C. Y., Neuhauser D., & Oreg Y., J. Chem. Soc. Faraday Trans., **86**, 1721, 1990
- [29] Huarte-Larranga F., Gimenez X., & Aquilar A., J. Chem. Phys., **109**, 5761, 1998
- [30] Takayanagi T., & Kurosaki Y., J. Chem. Phys., **113**, 7158, 2000
- [31] Rackham E. J., Huarte-Larranga F., & Manolopoulos D., Chem. Phys. Lett., **343**, 356, 2001
- [32] Riss U. V., and Meyer H. -D., J. Chem. Phys., **105**, 1409, 1996
- [33] Manolopoulos D. E., J. Chem. Phys., **117**, 9552, 2002
- [34] Neuhauser D., Baer M., J. Chem. Phys., **93**, 2862, 1989
- [35] Neuhauser D., Baer M., J. Chem. Phys., **90**, 4351, 1989
- [36] Colbert D. T., and Miller W. H., J. Chem. Phys., **96**, 1982, 1992
- [37] Stechel E. B., Walker R. B., & Light J. C., J. Chem. Phys., **69**, 3518, 1978
- [38] Press W., Flannery B., Teukolsky S., Vetterling W., Numerical Recipes, Cambridge Press University, 2003

*Five year plans and new deals  
Wrapped in golden chains  
And I wonder, Still I wonder  
Who'll stop the rain?*

# 4

## Writing the NIP code

### 4.1 Structure of the program

---

The NIP program, developed during the second year of my PhD thesis, is organized with an input file, a main program and a set of subroutines and functions. The entire code is implemented in fortran 95 with programming style object oriented. A total of 18,000 lines of code have been written including the mathematics libraries (CERN libs) and some other support routines. The usual LAPACK and BLAS external libraries are largely used and different architecture are supported by the code (AMD/Opteron, Intel/Core and IBM/Power6).

The input file feeds to the main program all the information that define the physical and computational features of the problem of interest. The input parameters are organized through several *namelists*:

- **propagator**: which defines the step-size and the range of integration
- **dvrgrid**: which defines the parameters needed by the DVR subroutines to generate the roto-vibrational basis set
- **moldata**: containing all the physical parameters which define the scattering partners
- **scatdata**: including the collision energy grid
- **nipparams**: allow to decide the parameters of NIP reported in eq. 3.21
- **parallelenv**: to define the parallel environment, contains information about MPI and OPENMP processes

Here below an input example:

## Writing the NIP code

---

```
&propagator
rstart=0.750d0,
rend=10.0d0,
mtr=5000 /

&custompred
rswitch1=6.00d0,
rswitch2=12.00d0,
dh1=0.01d0,
dh2=0.10d0,
dh3=0.50d0 /

&dvrgrid
rmin=0.750d0,
rmax=15.0d0,
ndvr=100 /

&moldata
homo=.true.,
symmetric=.true.,
ma=1.0078250320d0, mb=1.0078250320d0, mc=2.01355321270d0,
system_id=2, reactant_de=0.17447440045655613d0, exothermicity=+0.0d0 /

&basisset
nbasis=150,
numax=15,
jmax=18,
omega=0,
jtot=0,
asymptotic_rk=500.0d0 /

&scatdata
nu_init=0, j_init=0, reag_escat=0.0583d0,
use_total_energy=.true. /

&nipparams
nip_on=.true., rmatrix_real=.false.,
nip_rmin=3.50d0, nip_rmax=7.50d0, nip_order=2,
nip_strength=1000.0d0, nip_id=1,
nip_rk_boundary=.false., nip_rk_min=0.0d0, nip_rk_max=0.0d0 /

&parallelenv omp_num_threads=4, omp_eigv_threads=4, mpi_proc_out=0 &end
&mpigrd log_enrg_scale=.f., enrg_start=0.4d0, enrg_step=0.1,
nenrg=20, mpi_initial_state=1 /
```

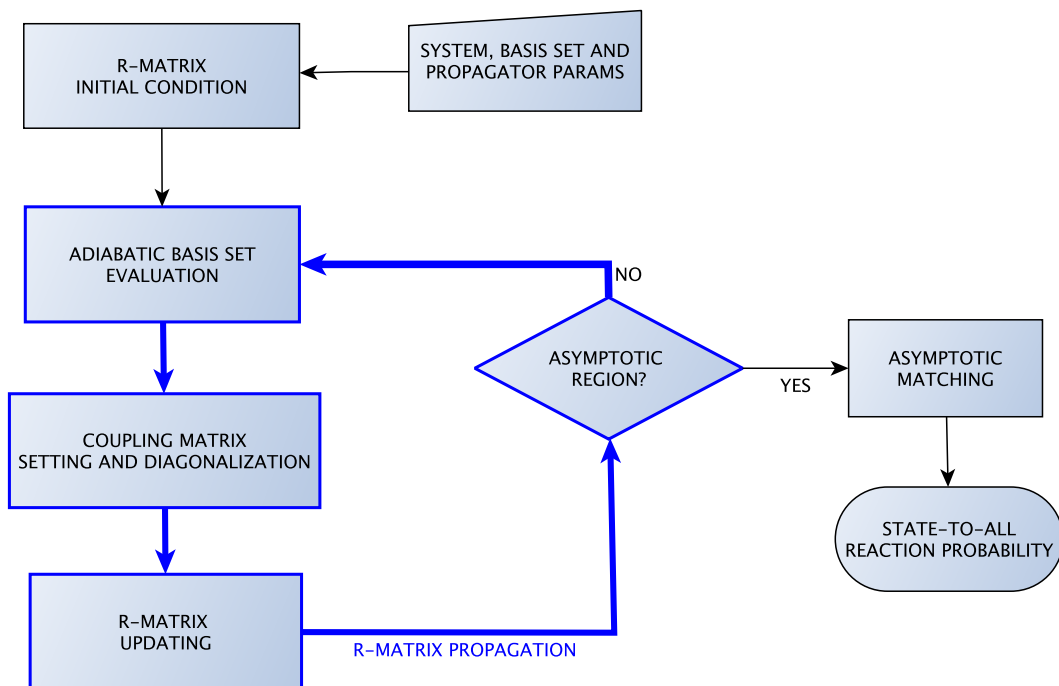


Figure 4.1 Functional flowchart for the NIP program.

The single reactive potential energy surface (PES) employed in the study of a typical reaction problem is implemented in a standard module organized to be consistent with the rest of the code. Then, it is easily possible to include in this PotentialEnergySurfaces.f90 routine any new PES involving a new process that is desirable to study.

The functional flowchart for the NIP program is depicted in figure 4.1. The code solves a typical Cauchy problem imposing an initial condition over the R-matrix which should be propagated up to the asymptotic region to give the final observables of interest. As it is clear from the flowchart, the code, at its heart, loops over a radial grid to integrate the coupled-channel differential equations. The equation of R-matrix propagator has been given in section 3.3.1; following those equations it becomes possible to outline this part of the code as follows:

1. Evaluation of the  $V^{NIP}$  over the DVR grid
2. Evaluation of the total potential  $V(r, \vartheta; R_k)$  at a fixed  $R_k$ , it means obtaining the  $V_\lambda$  coefficients of the expansion 3.28
3. Evaluation of the roto-vibrational basis set  $(\varphi_a)$  by diagonalizing the molecular hamiltonian, as explained in section 3.3.1
4. Setting up of the coupling matrix  $W$  (eq. 3.32)
5. Diagonalization of  $W$  which gives the  $T, T^{-1}$  matrices and the eigenvalue  $\lambda$  (eq. 3.38)

6. Evaluation of the sector matrices  $r_{14}$  and  $r_{23}$  (eqns 3.45, 3.46)
7. Evaluation of the overlap matrix  $\Theta$  (eq. 3.44)
8. Evaluation of the  $Q$  and  $Q^{-1}$  matrices (eqns 3.42, 3.43)
9. Updating of the global  $R$  matrix

The NIP-code is essentially a serial code which implements at its heart an R-matrix non-hermitian propagator. The R-matrix propagation scheme consists in assembling recursively the sector R matrices, starting from the sector nearest to the origin and continuing toward the asymptotic region where the matching procedure can be done in order to obtain the relevant scattering quantities. N-steps of propagation have to be done (where N usually is about 900). If we consider the R-matrix at the  $i$ -th step as a function of the R-matrix evaluated at the  $i-1$ -th step:

$$R_i = \phi(R_{i-1}) \quad (4.1)$$

then it is clear that we can speed-up the calculation only if we are able to minimize the time spent in evaluating the  $\phi(R_{i-1})$  function. The  $\phi$  function evaluation needs several matrix-matrix multiplications, two matrix inversions and one matrix diagonalization (these operations are carried out by ZGEMM, ZGESV and ZGEEV blas and lapack routines respectively) which, as the profiling with gprof confirms, are the most time-consuming routines of the whole code. It should be noted that some important CPU time is spent during a propagation step in evaluating the coupling matrix elements and the basis set overlap matrix. Two distinct phases can be recognized during the R-Matrix propagation which differ depending on the typical dimensions of the matrices involved and hence for the computational resources needed to accomplish the task:

### 1. Basis Set Evaluation

- typical matrix dimension: 4000-10000
- main linear algebra problem(s): real symmetric eigenproblem

### 2. R-Matrix Update

- typical matrix dimension: 400-1000
- main linear algebra problem(s):
  - complex non-hermitian eigenproblem
  - complex general matrix inversion
  - complex general matrix mult-add

N	n	Phase-1 (s)	Phase-2 (s)	Total (s)
2500	250	11.3	1.3	12.6
5000	500	88.5	9.3	97.8
7500	750	285.2	29.6	314.8

Table 4.1 NIP-RVABS propagation step wall clock time on an Intel Core2 Duo E7400@2.80GHz CPU. Two MKL threads has been used.

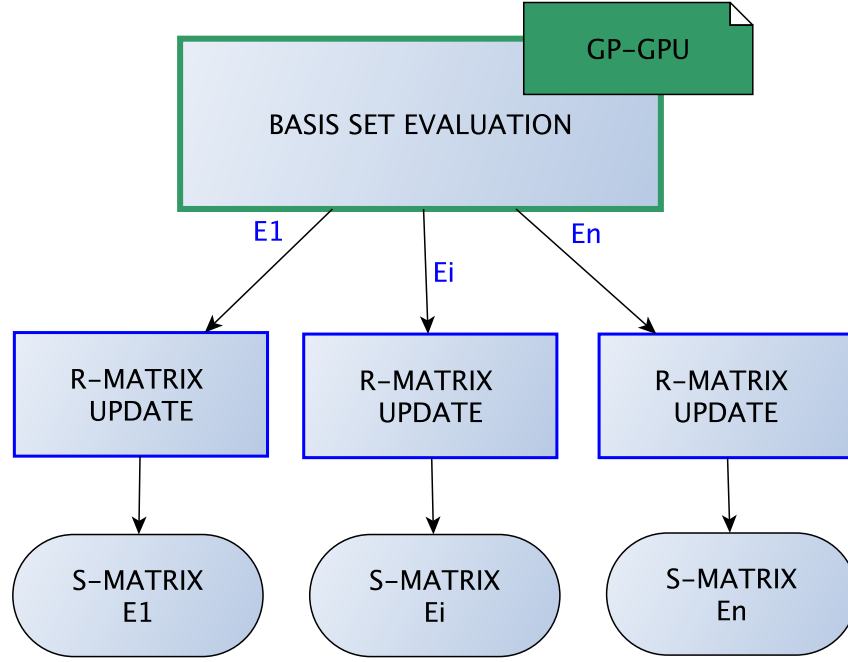
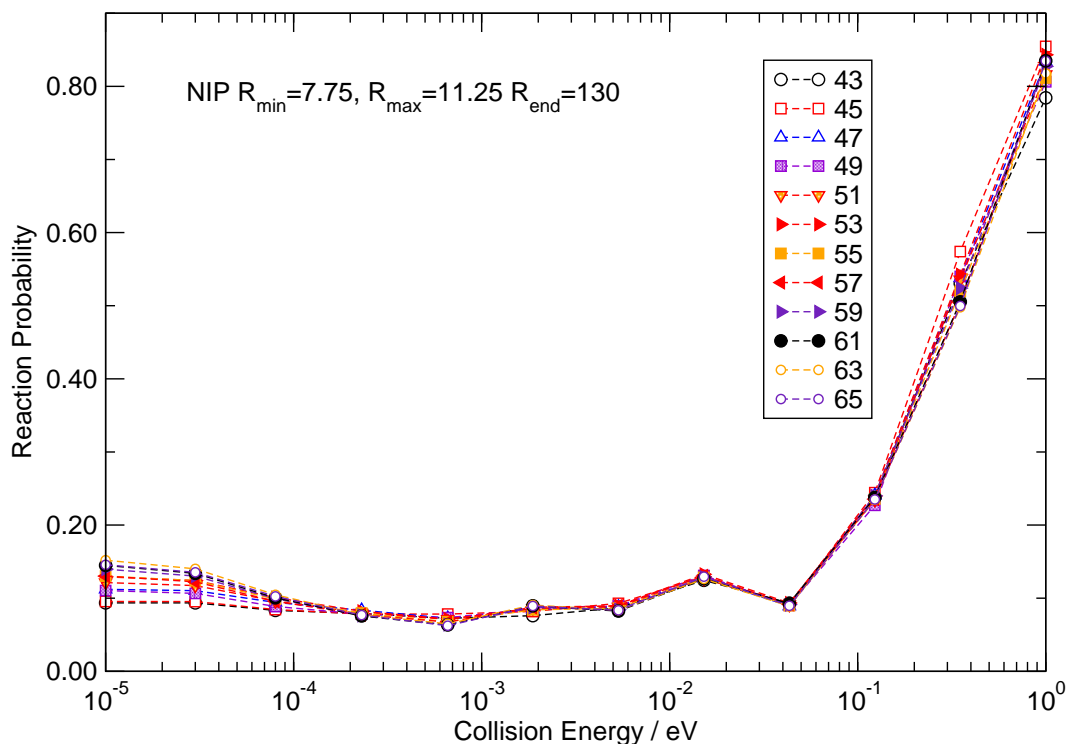


Figure 4.2 Scheme of the optimization steps for the NIP code.

#### 4.1.1 The optimization procedure

Due to the dimensions of the matrices involved, the phase-1 is much more computationally demanding. Table 4.1 reports the elapsed time for a single R-Matrix propagation step on a Intel Core2 Duo E7400@2.80GHz CPU. The phase-1 wall clock time is about one order of magnitude greater than the one for phase-2. It is also worth noting that phase 1 is *collision energy independent*. On the other hand, phase-2 is *collision energy dependent* and it has negligible execution time when compared to that for the phase-1. If we further consider that our principal interest is usually to study the reactivity over a fairly broad range of energies we easily come to the partitioning of the calculation workload as sketched by figure 4.2. In the scheme of figure 4.2 the most computational demanding symmetric eigenvalue problem of phase-1 is solved by using multi-threaded (MKL) or GP-GPU enabled (MAGMA) linear algebra subroutines. The phase-1 calculation is carried out by the master MPI process and then broadcasted to  $n-1$  MPI slave processes that can proceed through phase-2. In this way  $n$  collision energies R-Matrix propagations can be done in

Figure 4.3 The  $j_{\max}$  parameter convergence tests

parallel.

#### 4.1.2 How to make a calculation

When we start to tackle a reactive scattering problem with our NIP code we need to evaluate the time spent for the convergence step. In previous section we reported a typical input needed to run the program, from that is clear how much parameters we need to test to reach a convergence within the 1%. Some of the parameters are less demanding than other to reach convergence (e.g. NIP and propagator). Most of the time is spent to test "nbasis" and "jmax" whose both depend on the "dvr" number of points. In the figures 4.3, 4.4, and 4.5 we report some of the test we did for an accurate study of a reactive system to show the stability of our code.



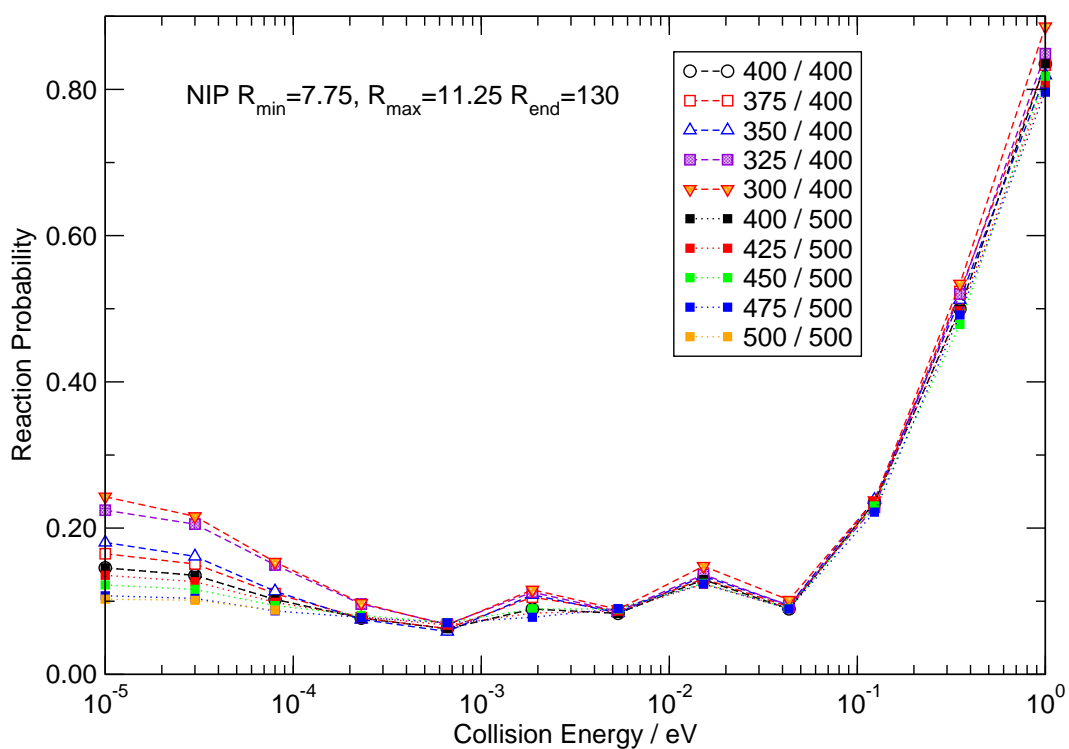


Figure 4.4 The "nbasis" parameter convergence tests. In the inset the label 400/400 means the number of functions used over the total available basis functions.

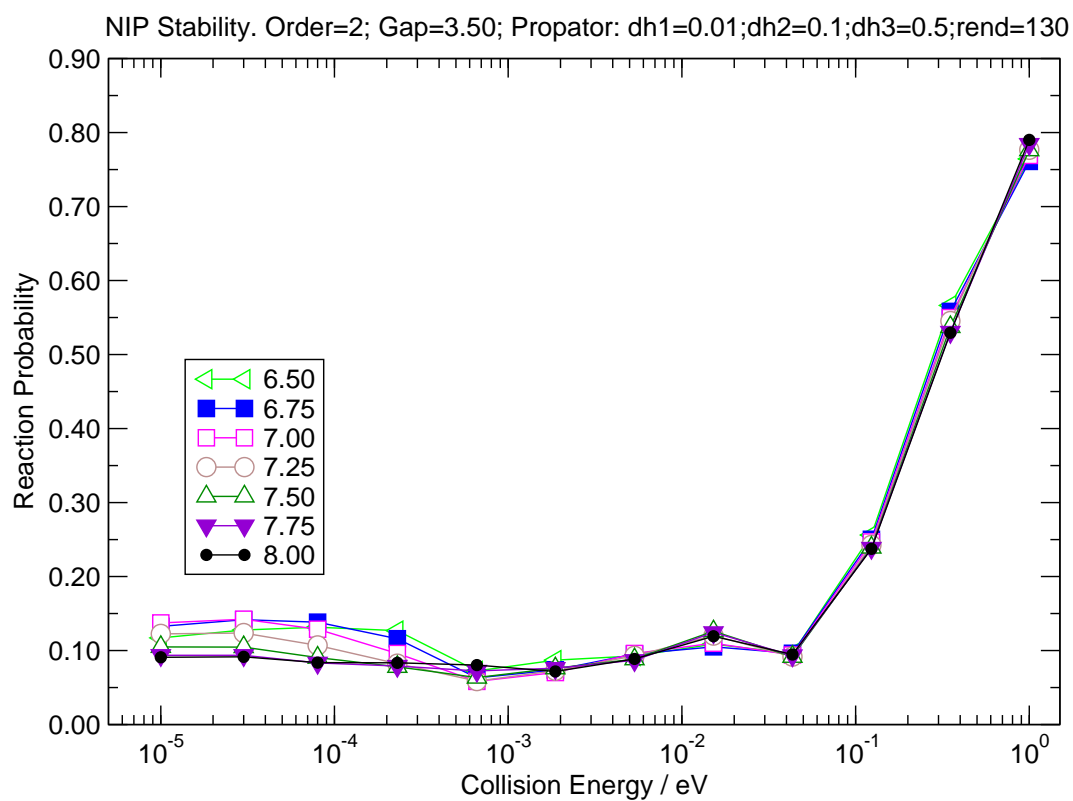


Figure 4.5 NIP stability convergence test.

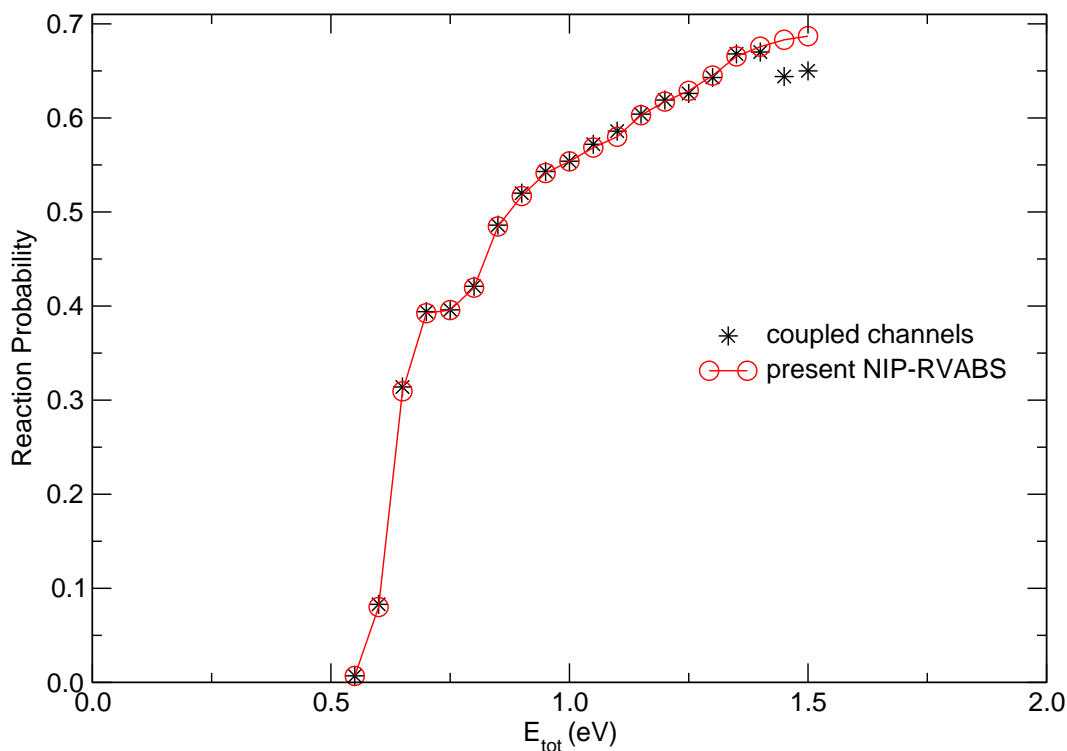


Figure 4.6 Computed reaction probabilities for the  $\text{H}_2 + \text{D} \rightarrow \text{HD} + \text{H}$  reaction. The present NIP results are given by the open circles while the exact coupled-channels calculations are from ref. [1].

## 4.2 Benchmarks

### 4.2.1 $\text{H}_2 + \text{D}$ benchmark

Because of its popularity as a testing ground for computational methods that deal with reactive collisions, we have tested our NIP implementation in its form where a rovibrational adiabatic basis-set (RVABS) is employed (as described in section 3.3.1) on the reaction probability for the exchange model reaction  $\text{H}_2 + \text{D} \rightarrow \text{HD} + \text{H}$ , comparing our findings with those given by the accurate close-coupling calculations of ref. [1]; we also employ the same potential energy surface (PES) discussed in that work and fully referenced therein.

The results of the two calculations are shown in figure 4.6, where we clearly see that, at least for a weakly interacting system without complex formation, our present results are remarkably close to the exact calculations, indicating a small departure from them only at the highest available energies.

### 4.2.2 The $\text{LiH} + \text{H}$ neutral reaction: validating the method

The neutral lithium hydride molecule, as explained and discussed in the Introduction, is one of the key molecules that is expected to be involved in the molecular

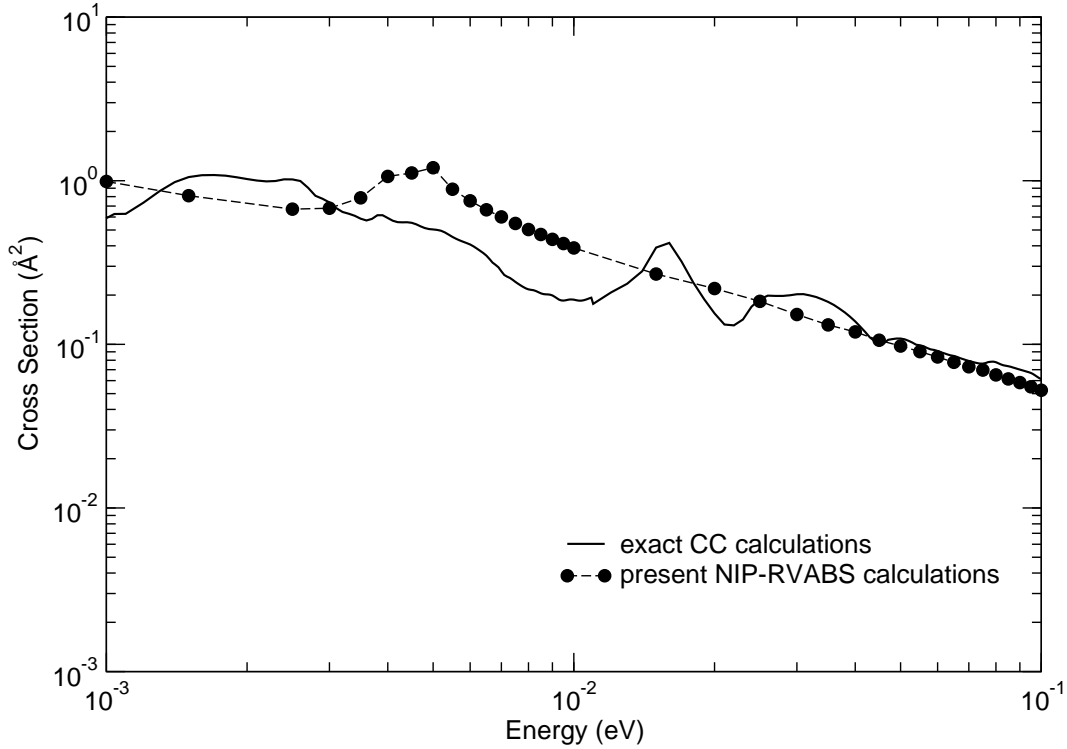


Figure 4.7 Computed reactive cross sections ( $J = 0$ ) for the  $\text{LiH} + \text{H} \rightarrow \text{Li} + \text{H}_2$  process over a broad range of energies. The solid line reports the data from ref. [5] while the filled-in circles show the result obtained with the NIP approach.

cooling processes under early universe conditions [2, 3].

Its possible destruction via an exothermic reaction with the hydrogen atoms of the environment



is therefore an important process that we studied during this Phd program, using an ab-initio PES [4] and an exact solution of the quantum scattering problem. The results reported by figure 4.7 indeed allow us to further test the reliability of the present computational method by comparing the NIP-RVABS results with our earlier, exact quantum results of [5]. The comparison shows again remarkable agreement between the two methods, especially in the higher range of energies. Since the NIP approach uses an absorbing potential method, it is natural to expect that some of the finer, resonant features of the exact quantum method are averaged over and therefore do not explicitly appear: we see, however, a property crucial for computing the final rates, remains indeed the same in both methods.

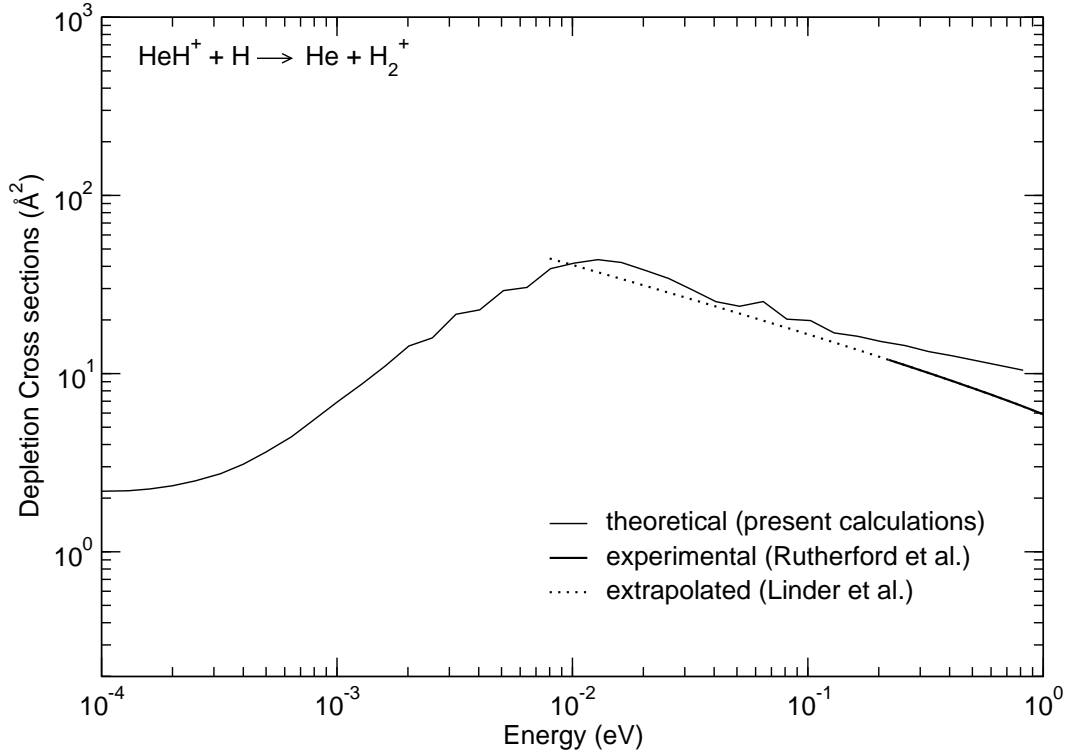


Figure 4.8 Computed integral cross-sections as a function of energy. The thick line represents the fitted experimental data from [6]. The dotted line is obtained from the formula given by Linder et al. [7] by extrapolating the Rutherford's data.

#### 4.2.3 HeH<sup>+</sup>: a key reaction to test our NIP method

The most surprisingly result we obtained with our implementation of the NIP approach involve a very important reaction



Crossed-beam experimental data for energies larger than 0.2 eV have been presented by Rutherford & Vroom [6], fitted by Linder et al. [7] and then included in the early universe model calculations of Schleicher et al. [8], but no direct calculations have been made available thus far.

Our results are reported in figure 4.8 together with the experimental results. The agreement between our theoretical results and the experimental findings, both measured and extrapolated, is reassuringly good and confirms the physical reliability of the present NIP method for handling ionic reactions. No measured data are available at the lower collision energies as crossed beam experiments with ionic partners become increasingly difficult in that range.



# Bibliography

- [1] Zhang J. Z. H., J. Chem. Phys., **91**, 1528, 1989
- [2] Maoli R., Melchiorri F., and Tosti D., ApJ., **425**, 372, 1994
- [3] Stancil P. C., Lepp S., and Dalgarno A., ApJ., **458**, 401, 1996
- [4] Wernli M., Caruso D., Bodo E., and Gianturco F. A., J. Phys. Chem. A, **113**, 1121, 2009
- [5] Bovino S., Wernli M., and Gianturco F. A., ApJ., **699**, 383, 2009
- [6] Rutherford J. A., and Vroom D. A., J. Chem. Phys., **58**, 4076, 1973
- [7] Linder F., Janev R. K., and Botero J., Atomic and Molecular Processes in Fusion Edge Plasmas, ed. R. K. Janev (NY: Plenum Press), 397, (1995)
- [8] Schleicher, D. R. G., Galli, D., Palla, F., Camenzind, M., Klessen, R. S., Bartelmann, M., & Glover, S. C. O. A&A, **490**, 521, 2008





*Heard the singers playing  
How we cheered for more  
The crowd had rushed together  
Tryin' to keep warm*

# 5

## Results for the chemical routes

### 5.1 The lithium chemistry

The suggestion that chemical processes involving lithium could play a role in the evolution of the early universe in the post-recombination era has been put forward several years ago [1–3], starting from the consideration that Li is produced a few minutes after the Big Bang and the formation of other light atoms like H, D and He [4, 5]. The fractional abundances of these elements are sensitive to the baryon density of the universe and set constraints on its actual value [6]. As the universe expanded, its radiation temperature decreased and the atomic ions originating from the above elements gave rise to neutral atoms by recombination with electrons, thus initiating the formation of molecular species by radiative association: H<sub>2</sub>, HD and LiH. The latter molecule, because of its large dipole moment and low ionization potential, may induce spatial and/or spectral distortions in the cosmic background radiation (CBR), as originally suggested by Dubrovich [7] and as experimentally surmised by the pionering work of Maoli et al. [8]. Eventually, during the gravitational collapse leading to the formation of the first stars, the low excitation threshold and the efficient radiative decay along the rotovibrational manifold are additional properties that could favor the role of LiH and LiH<sup>+</sup> as molecular coolants of the primordial gas [9]. The nonequilibrium level population in the presence of a different gas and radiation temperature may have a possible signature in protogalactic clouds, imprinting small fluctuations in the CBR spectrum [10].

The chemistry of Li in the early universe has been discussed in the past, reaching contrasting conclusions [2, 3, 9, 11]. It has been suggested that the lithium chemistry was initiated by the recombination of lithium, which occurred near  $z = 450$  through radiative recombination



mutual neutralization,



and radiative association,



With the production of neutral lithium, lithium hydride could be formed by radiative association



## Results for the chemical routes

```

INPUT:
-----
mass =          7.016          1.008          1.008
jtot =                      0
ipar =                      1
jpar =                     -1
jmax =                      21
kmin =                      0
kmax =                      0
rmax =                      30.000
drho =          0.5000000000000000E-01
emax =                      3.500
enrg =                      0.10000000
dnrg =                      0.01000
nnrg =                      100
nout =                      10
jout =                      20
-----
mtr=          554
-----
PARSET:
-----
rmin =                      2.29
mro =                      91
mvi =                      133
nvi =                      77
smax =                      5.93
-----

```

Figure 5.1 ABC input parameters for the reaction  $\text{LiH} + \text{H}$ .

There are many other pathways of formation of  $\text{Li}$  and  $\text{Li}^+$  and  $\text{LiH}$  and  $\text{LiH}^+$  molecules that we shall discuss in the next chapter. Of critical relevance, is the uncertainty in the knowledge of reliable reaction rates for the destruction of  $\text{LiH}$  and  $\text{LiH}^+$  molecules via strongly exothermic reactions without entrance barriers:



and



### 5.1.1 $\text{LiH} + \text{H}$ depletion

In the last 20 years a great deal of effort has been spent to calculate accurate rate coefficients for the reaction 5.5. Stancil et al [2] conjectured a temperature-independent rate coefficient of  $2 \times 10^{-11} \text{ cm}^3\text{s}^{-1}$  by assuming the absence of an activation barrier and therefore postulated the insignificant role of  $\text{LiH}$  in erasing primary anisotropies in the CBR field. Dunne et al [12], using a quasi-classical dynamics and Defazio et al [13], with a real wave-packet method, obtained rate coefficients in a range of temperatures  $0 < T < 4000 \text{ K}$ . However, the potential energy surface (PES) used by

T(K)	$\alpha(T)_{ortho}(\text{cm}^3\text{s}^{-1})$	$\alpha(T)_{para}(\text{cm}^3\text{s}^{-1})$
10	1.57 - 11	1.71 - 11
20	4.05 - 11	4.40 - 11
40	8.14 - 11	8.74 - 11
80	1.56 - 10	1.61 - 10
100	1.94 - 10	2.00 - 10
200	3.65 - 10	3.69 - 10
500	7.66 - 10	7.16 - 10
1000	1.14 - 09	9.41 - 10
2000	1.28 - 09	8.12 - 10
4000	8.05 - 10	3.03 - 10
5000	5.64 - 10	1.63 - 10
7000	2.47 - 10	4.26 - 11
8000	1.58 - 10	2.10 - 11
10000	6.20 - 11	4.90 - 12

Table 5.1 Computed rate coefficients summed over all final states of the products. The notation 1.57 - 11 corresponds to  $1.57 \times 10^{-11}$ .

T(K)	$\alpha(T)_{\nu=0}(\text{cm}^3\text{s}^{-1})$	$\alpha(T)_{\nu=2}(\text{cm}^3\text{s}^{-1})$	$\alpha(T)_{\nu=4}(\text{cm}^3\text{s}^{-1})$
10	1.57 - 11	3.33 - 13	6.83 - 13
20	4.05 - 11	1.48 - 12	2.27 - 12
40	8.14 - 11	6.28 - 12	4.29 - 12
50	1.00 - 10	9.88 - 12	9.35 - 12
80	1.56 - 10	2.47 - 11	2.00 - 11
100	1.94 - 10	3.72 - 11	2.90 - 11

Table 5.2 Calculated rate coefficients, summed over all final o-H<sub>2</sub> states, for different vibrational initial states of LiH.

those calculations (the one generated by Dunne et al [12]) presented a rather deep well in the product valley which would cause unphysical trapping and resonance effects in the dynamics within partners which are instead interacting via mainly van der Waals forces. We therefore carried out new calculations solving the quantum coupled-channel hyperspherical equations involving a new 3D-surface [14] recently calculated and fitted with very good accuracy. The exothermicity of the reaction was estimated to be 2.258 eV, and it now correctly proceeds without a barrier into the exothermic products of eq. 5.5.

The main improvements introduced by our newly calculated PES for the ground electronic state of reaction 5.5 have been the correct description of long-range forces among product partners and the elimination of barrier features in the entrance channel of the reagents, as discussed in more detail by Wernli et al [14].

The reaction probability and rate coefficients were thus calculated for  $J = 0$  using the reactive program ABC [15] and carefully testing all convergence-controlling computational parameters in order to yield a confidence level on the final cross sections below 1%. In figure 5.1 the input file of ABC program used in the calculations is shown. Following a uniform  $J$ -shifting approach as introduced in sec. 3.2.1, we further obtain the full rate coefficients from our knowledge of the  $J = 0$  rate ( $\alpha^{J=0}(T)$ ):

$$\alpha(T) \simeq \frac{k_B T}{B} \alpha^{J=0}(T) \quad (5.8)$$

where  $T$  is the temperature,  $k_B$  is the Boltzmann constant and  $B$  is obtained by evaluating the rotational constant of the collision complex at the estimated geometry of the transition state of our PES. In our case  $B = 0.84 \text{ cm}^{-1}$ , a value which slightly differs from the earlier suggestions [16]. The main physical reasons for choosing the above approximation to generate the full rate coefficients rest on the reasonable assumption that higher  $J$  values are chiefly modifying the shape of the transition states through changes of the centrifugal potential of the reaction complex. This is certainly a realistic description of an exothermic reaction that proceeds without a barrier in the entrance channels, as is indeed the case here.

To start assessing the outcomes of the quantum calculations described in the previous section, we report in table 5.1 the LiH reaction rates, summed over all final states, for the formation of both  $\text{oH}_2$  and  $\text{pH}_2$  as product molecules. The range of temperatures covers all the values expected to be relevant for the corresponding range of  $z$  of astrophysical interest. Several comments could be made about these results:

- the rates turn out to be rather large over the whole range of  $T$  and to be largely independent of yielding either  $\text{pH}_2$  or  $\text{oH}_2$  as products. Most importantly, our new values from accurate ab initio methods turn out to be close to the educated estimates of Stancil et al [2], although extending and improving on their temperature dependence. We therefore confirm with the present calculations the likely occurrence of a rapid disappearance of any newly formed LiH because of its reaction with the surrounding hydrogen. This is an important result which now comes exclusively from non-empirical calculations;

- above 200 K the rates were obtained by using the functional form

$$\alpha(T) = aT \times e^{(-bT)}, \quad (5.9)$$

as suggested by Stancil et al [2] in their kinetic model of lithium reaction in the primordial gas. Our calculated parameters are  $a=2.05 \times 10^{-12} \text{ cm}^3 \text{ s}^{-1} \text{ K}^{-1}$  and  $b=0.00058 \text{ K}$  for  $\text{oH}_2$  and  $a=2.18 \times 10^{-12} \text{ cm}^3 \text{ s}^{-1} \text{ K}^{-1}$  and  $b=0.00084 \text{ K}$  for  $\text{pH}_2$ . The values employed by Defazio et al [13] and by Padmanabam and Mahapatra [16] were obtained by using the same formula but turned out to be slightly different and to yield different final rates. However, given the fact that they employed a different reaction PES (from Dunne et al [12]) this result is not surprising.

The further calculations reported by table 5.2 show another interesting facet of the present reaction since we give there the low-T rates obtained for the formation of  $\text{oH}_2$  starting from different vibrational levels of the LiH molecule; one clearly sees that the initial process of LiH destruction changes when the LiH reacting molecule is internally "hot". Such states could be the result of the occurrence of only partial relaxation of the latter species whenever is formed during the recombination process indicated by eq. 5.4. In any event, the order of magnitude of the rates does not vary dramatically when we change the vibrational energy content of the initial molecular partner. The results of the tables are pictorially given by the two panels of figure 5.2, where we show on the top panel the temperature dependence of the LiH destruction rates leading to the formation of both  $\text{pH}_2$  and  $\text{oH}_2$  and, in the lower panel, the  $\text{oH}_2$  formation (caused after the LiH destruction) for different vibrational content of the initially formed LiH partner obtained through eq. 5.4. One sees there that the  $\text{oH}_2$  formation is the favoured process outside a very small T-values region, as one should expect to find by nuclear multiplicity consideration. Furthermore, the presence of vibrationally "hot" LiH molecules can cause the depletion rates to become smaller, in favour of the simpler hydrogen exchange reaction.

The data of table 5.3 additionally present the computed rates for the depletion reaction 5.5 leading to the formation of  $\text{H}_2$  molecules in different, final rotovibrational states. This information is important for establishing the differences in the probabilities of producing internally excited hydrogen molecules which in turn can decay by radiative processes. The results cover the range of temperatures that also map the redshift values of relevance for the early Universe study, and clearly suggest that the individual  $\text{H}_2$  formation rates change only little by changing the final rotovibrational level of the newly formed molecule: the examples of Table 5.3, in fact, indicate a variation of about one order of magnitude from forming  $\text{H}_2$  ( $\nu'=0, j'=1$ ) to producing instead  $\text{H}_2$  ( $\nu'=3, j'=9$ ). One should also note that the  $\text{H}_2$ -formation reaction becomes endothermic for the situations where it is forming  $\text{H}_2$  in vibrational states above  $\nu'=4$  (see also Wernli et al [14]).

The general behaviour shown by the data of Table 5.3 is further presented in a pictorial form by the two panels of figure 5.3, where we show as a function of the temperature, and of the redshift values, the relative behaviour of a selection of rates of  $\text{H}_2$ -formation into different, final rotovibrational states for the  $\text{H}_2$  molecule. All rates appear to behave very similarly and to largely remain of the same order of

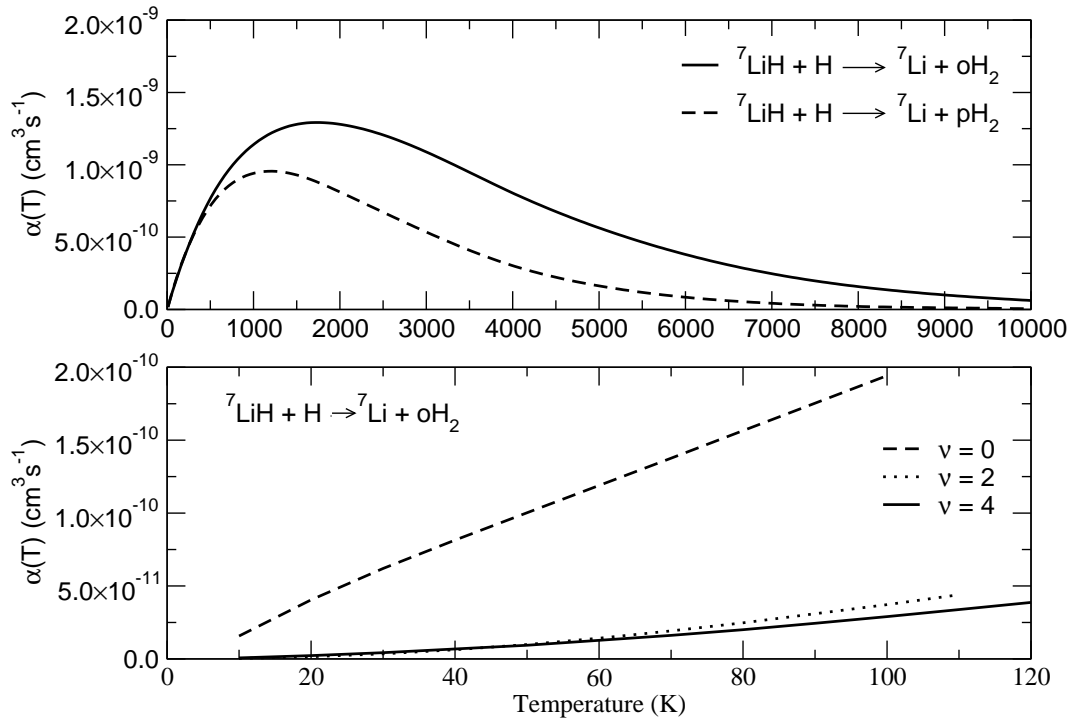


Figure 5.2 Computed quantum reaction rates of LiH destruction. The top panel shows the dependence on the spin state of the final  $\text{H}_2$  molecule over a very broad range of  $T$ , while the lower panel indicates, at the lower temperatures, the rate dependence on the initial vibrational state of LiH.

magnitude, although we see that the production of internally excited species, e.g. see the formation of  $\text{H}_2$  ( $\nu'=0$ ,  $j'=11$ ) in the upper panel and of  $\text{H}_2$  ( $\nu'=3$ ,  $j'=9$ ) in the lower panel, corresponds to smaller rates. Hence, the present, state-specific results indeed suggest that the newly formed  $\text{H}_2$  molecules should be preferentially formed in their ground rovibrational level, with a reduced probability for further contributing to radiative emissions.

The relative behaviour of the two chief processes, i.e. the hydrogen exchange reaction (termed here LiH survival) and the  $\text{H}_2$  formation (called the LiH destruction) are reported in figure 5.4 over a log-log scale in the main plot, while the same processes are shown on the temperature and redshift scales in the inset. The energy dependence clearly indicates that the H exchange is the dominant process at low collision energies, as expected because of the steric hindrance created by the bulkier Li atom to the low- $T$  insertion reaction, while the destruction of the LiH initially formed is seen to occur for the majority of the collisional events once the temperature (and the energy) becomes larger than about 300 K. In this temperature range, as we can see in the inset,  $z$  is estimated (Puy et al [17]) to be greater than 250. This means that the destruction process is dominant in the main molecular formation range; we can then assert that, since the fractional abundance is dramatically reduced, the exchange reaction is likely to be negligible.

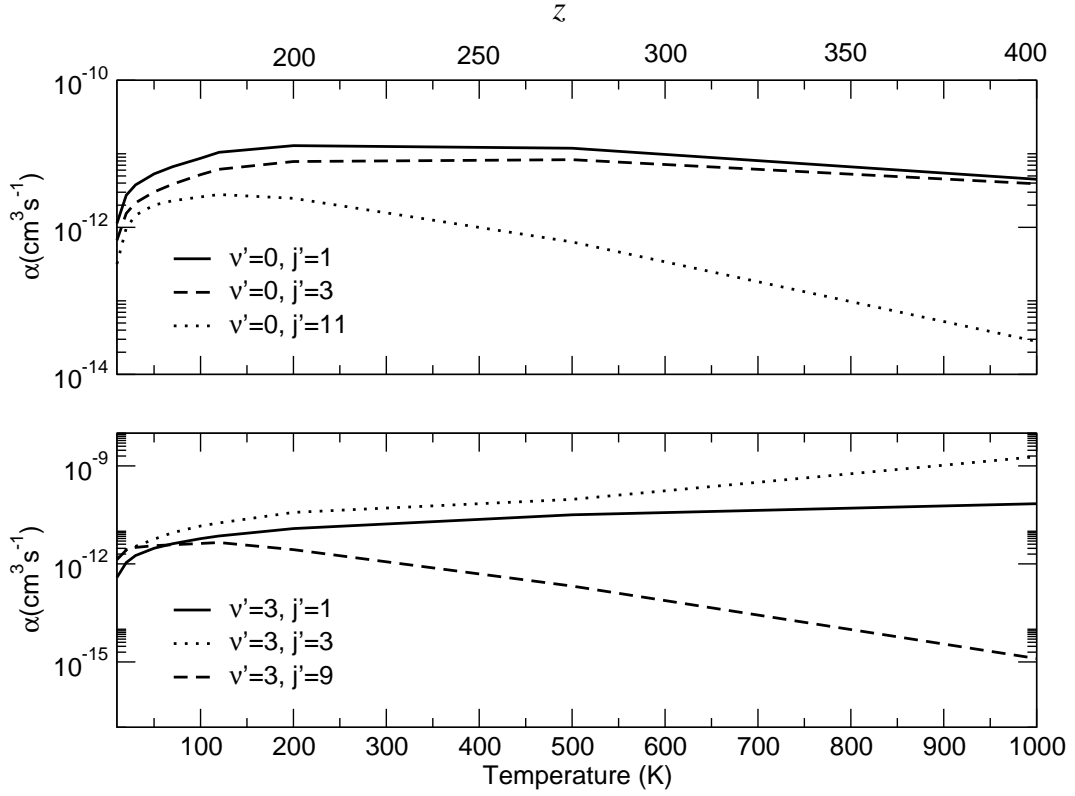


Figure 5.3 Computed rates for  $\text{H}_2$ -formation reaction as a function of the temperature and of the redshift values, for different final, rotovibrational states of the  $\text{H}_2$  molecule.

T(K)	$\nu'=0$			$\nu'=3$		
	$j'=1$	$j'=3$	$j'=11$	$j'=1$	$j'=3$	$j'=9$
10	1.13-12	6.65-13	3.18-13	3.85-13	1.51-12	1.34-12
20	2.73-12	1.55-12	9.73-13	1.10-12	2.70-12	2.65-12
30	3.78-12	2.15-12	1.46-12	1.80-12	3.44-12	2.20-12
50	5.31-12	3.03-12	2.01-12	3.01-12	5.70-12	3.62-12
70	6.68-12	3.86-12	2.30-12	4.15-12	9.04-12	3.85-12
100	8.70-12	5.21-12	2.59-12	5.93-12	1.45-11	4.24-12
120	1.05-11	6.15-12	2.79-12	7.15-12	1.80-11	4.52-12
200	1.29-11	7.86-12	2.48-12	1.21-11	3.78-11	2.73-12
500	1.19-11	8.33-12	6.33-13	3.19-11	9.45-11	2.10-13
1000	4.51-12	3.91-12	2.81-14	6.97-11	1.92-09	1.27-13

Table 5.3 Computed rates of  $\text{H}_2$  formation into different rotovibrational states. Only the o $\text{H}_2$  case is being presented. All units are  $\text{cm}^3\text{s}^{-1}$ .

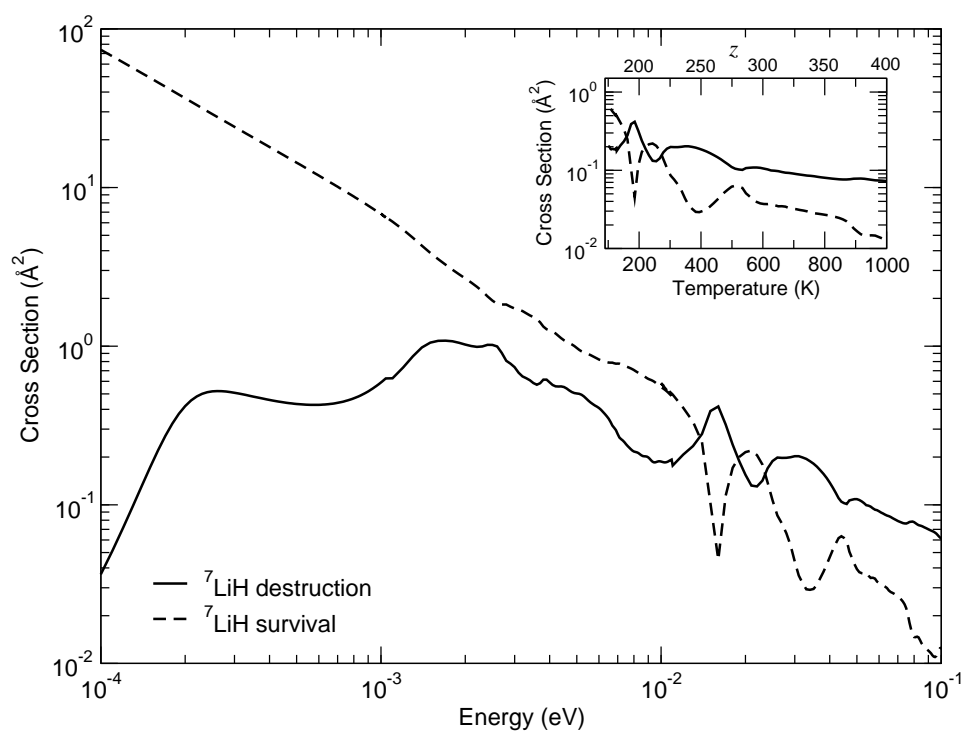


Figure 5.4 Computed hydrogen-exchange reaction (dashed line) and o-H<sub>2</sub> formation (solid line) over a large energy range (in the main plot) and over the first 1000 K (in the inset).



The final figure 5.5 reports now the general behaviour of the quantum reaction rates for the destruction process as a function of redshift, a quantity which covers the expected range relevant for early Universe evolution. One clearly sees once more that the rates around  $z=500$  are indeed fairly large and unequivocally suggest that one should expect rapid disappearance of any newly formed LiH molecules by reaction with the H atom present in the astronomical environment during the recombination era.

The present calculations are the first quantum results in regions of astrophysical interest which employ both the "exact" coupled-channel dynamics and the best, thus far, reactive potential energy surface obtained from ab-initio computations (Wernli et al [14]). They allow us to make the following points:

- over the range of relevant  $z$  the destruction reaction dominates over the LiH "survival" of the hydrogen replacement channel (see figs 5.4 and 5.5);
- to have the initial molecule still excited in any of its internal vibrational states does not modify the above result, although showing an increase of the simple H-replacement rates as  $\nu$  increases (see fig. 5.2);
- the analysis of the rates of H<sub>2</sub> formation into different rotovibrational levels (fig. 5.3) indicates that such species is preferentially formed into its lower ( $\nu'$ ,  $j'$ ) states, although the formation of internally "hot" H<sub>2</sub> molecules is far from negligible;
- formation of either oH<sub>2</sub> or pH<sub>2</sub> changes very little the computed rate values, thereby not influencing the above findings;
- the computed rates with the present PES turn out to be larger than the earlier calculations with a less accurate form of reactive interaction [13,16] and similar in size to the earlier, empirical estimates by Stancil et al [2].

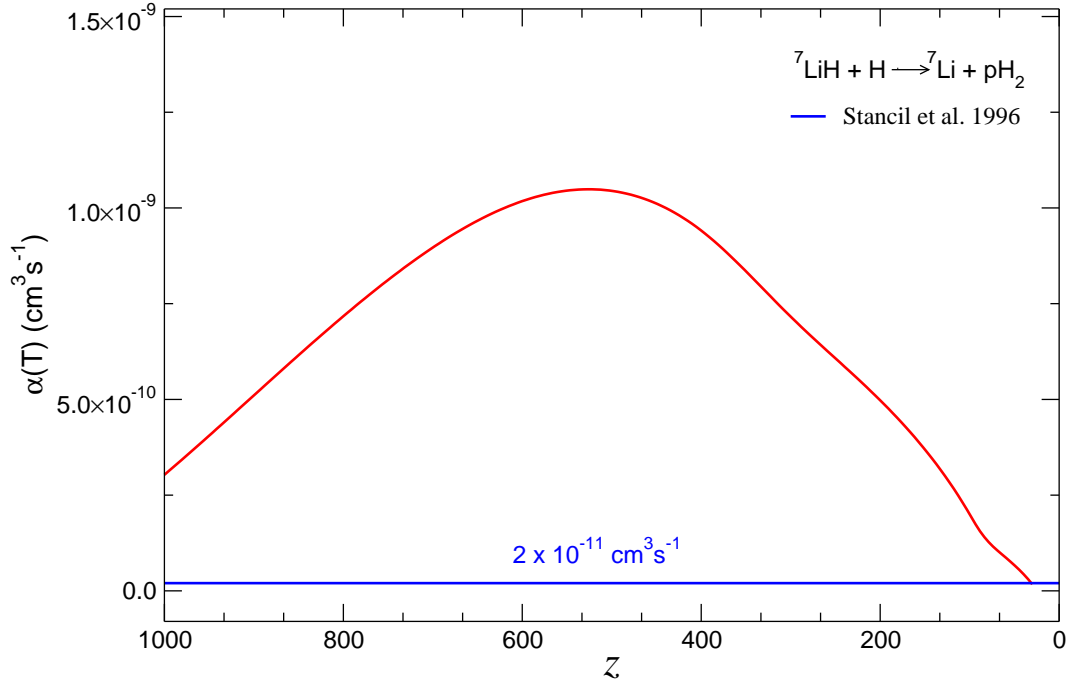


Figure 5.5 Computed quantum LiH destruction rates, into p-H<sub>2</sub> formation, as a function of the  $z$  values.

### 5.1.2 LiH + H<sup>+</sup> depletion

The calculations were carried out by solving the coupled channels equations under the additional effects of a negative imaginary potential (NIP), over a wide range of energies ( $10^{-4}$ -1.0 eV): the present choice for the best NIP parameters was based on accurate analysis of the PES and on the general suggestions reported in the earlier papers [18,19]. The value of  $r_{min}$  has been chosen so that any further increase of it does not affect the final results:  $r_{min} = 4.50$  a.u. and the monomial order  $n$  equal 2. The NIP was extended to  $r_{max} = 8.50$  a.u. to be sure that all flux is absorbed during reaction. The strength  $u_0$  is automatically calculated by our new code to fulfill the conditions given in section 3.3.1. We used a DVR grid of 300 points to represent the vibration coordinate, ranging from 0.5 a.u. to 20.0 a.u. and the R-matrix propagator as introduced by Light and coworkers [20]. The maximum propagation distance was 30.0 a.u. and convergence was tested as a function of the propagator step size. To reach the convergence for the probability values a basis set of 585 roto-vibrational functions (45 vibrational and 13 rotational) was included in the adiabatic basis set.

Fig. 5.6 shows the total reaction probability at  $J = 0$  as a function of collision energy for different initial vibrational state of LiH ( $\nu = 0, 1, 2, 5$ ) and for a fixed value of its rotational quantum number ( $j = 0$ ). As can be seen from that figure, the  $P^{J=0}(E_c)$  exhibits a large number of Feshbach-type resonances in the low energy range, which are especially marked for  $\nu = 0$ . This behaviour is clearly due to the presence of rather strongly bound collision complexes in the reactants and products channels which consequently activate the dynamical couplings, during the

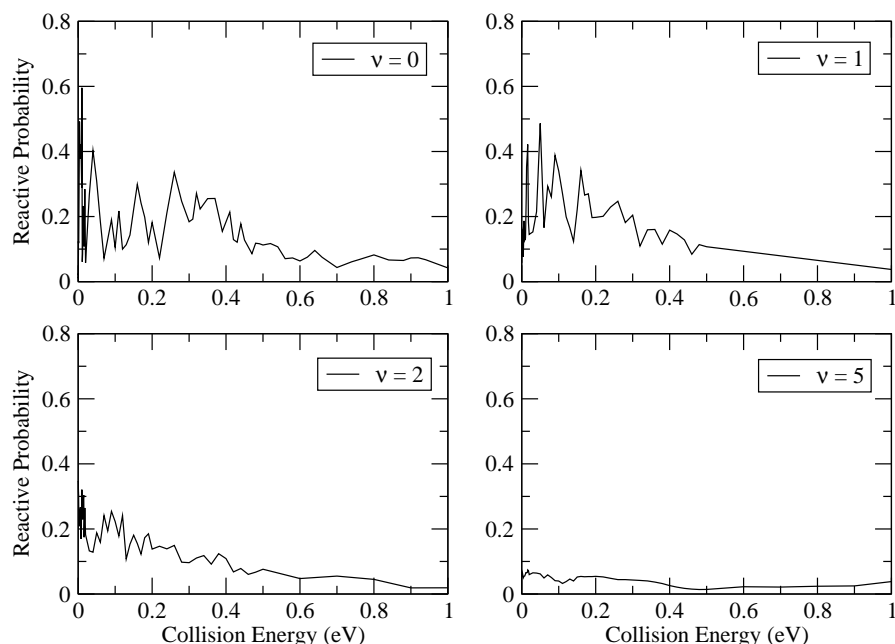


Figure 5.6 Computed  $J=0$  reaction probabilities for reaction (2). The panels show the calculations for different initial vibrational states of LiH.

low-energy scattering events, with the closed channels that open up over the well regions of the complexes. The resonant structure is clearly becoming weaker in the high energy region, as expected with the corresponding changes in the density of available closed channels. The panels of fig. 5.6 further indicate that the reactive probabilities for such a strongly exothermic process are affected very little by the vibrational energy content of the initial molecule, although the corresponding Feshbach resonances become less significant. The fact that the present  $J=0$  destruction reaction probabilities are found to be rather small for ionic reactive processes can partly be explained with the help of the recent findings from a stereodynamics study of Li et al. [21] which showed a strong dominance of backward scattering in the selected energy range, a feature that obviously implies smaller contributions from the  $J = 0$  dynamics shown by fig. 5.6. Another important result from the data of fig. 5.6 relates to the decreasing of the reactive probabilities at very low energies; as also suggested by Li et al. [21] one may argue that the process at very low energies is dominated by an indirect mechanism where the reactants remain trapped in the complex formation which could survive several picoseconds before breaking-up into one of the possible channels, including the reverse reaction that would then preserve the LiH molecule.

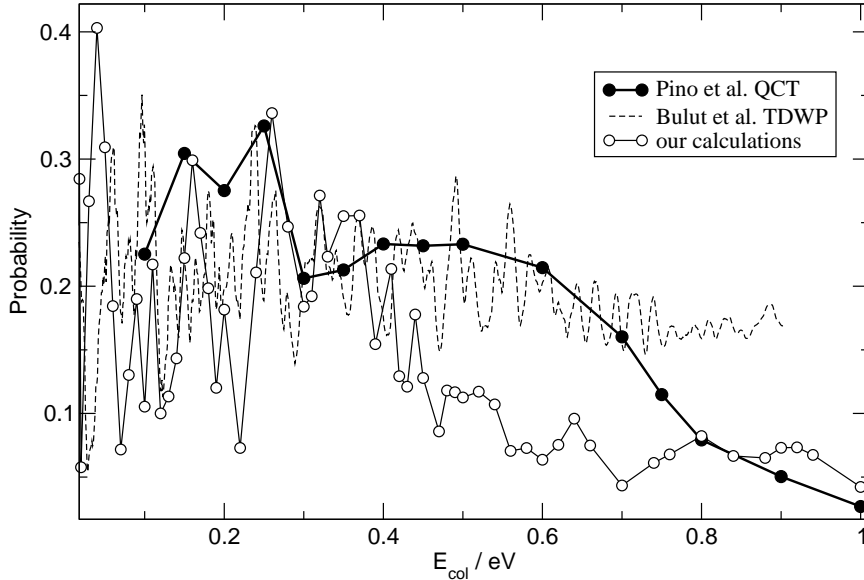


Figure 5.7 A comparison of computed  $J=0$  reaction probabilities for  $\text{LiH}(v=0)$  reactants in reaction (2). Previous calculations from Pino et al [23] and from Bulut et al [24] are also shown. See main text for further details.

In fig. 5.7 we further carry out a comparison with previous quantum and QCT calculations over the available energy range: the agreement is very good for the higher collision energies, beyond about 0.8 eV, where the wavepacket and semi-classical approaches are known to be more realistic. In the very low energies from threshold to about 0.2 eV we know that semiclassical calculations have problems, as well as the wavepacket evolutions. Our time-independent coupled-channel approach is seen therefore to follow closely the quantum resonances of the wave packet but to yield an overall lower set of probability values. In the intermediate range of energies we see that the calculations, as should be expected from the previous discussion on the feature of the PES, yield fairly low probability values since the destruction reaction with  $\text{H}_2^+$  formation should correctly come out with less flux than the survival reaction of the  $\text{LiH}$  reactant. Both wavepacket and semiclassical calculations do appear to fail in reproducing this expected behaviour at the intermediate energies.

$J$ -converged integral cross sections are finally presented in fig. 5.8 for the two considered processes involving the initial  $\text{LiH}$  partner: they are termed here the survival and destruction processes since we are chiefly concerned with the fate of the initial  $\text{LiH}$  concentration at the Early Universe conditions. A total of 150  $J$  angular

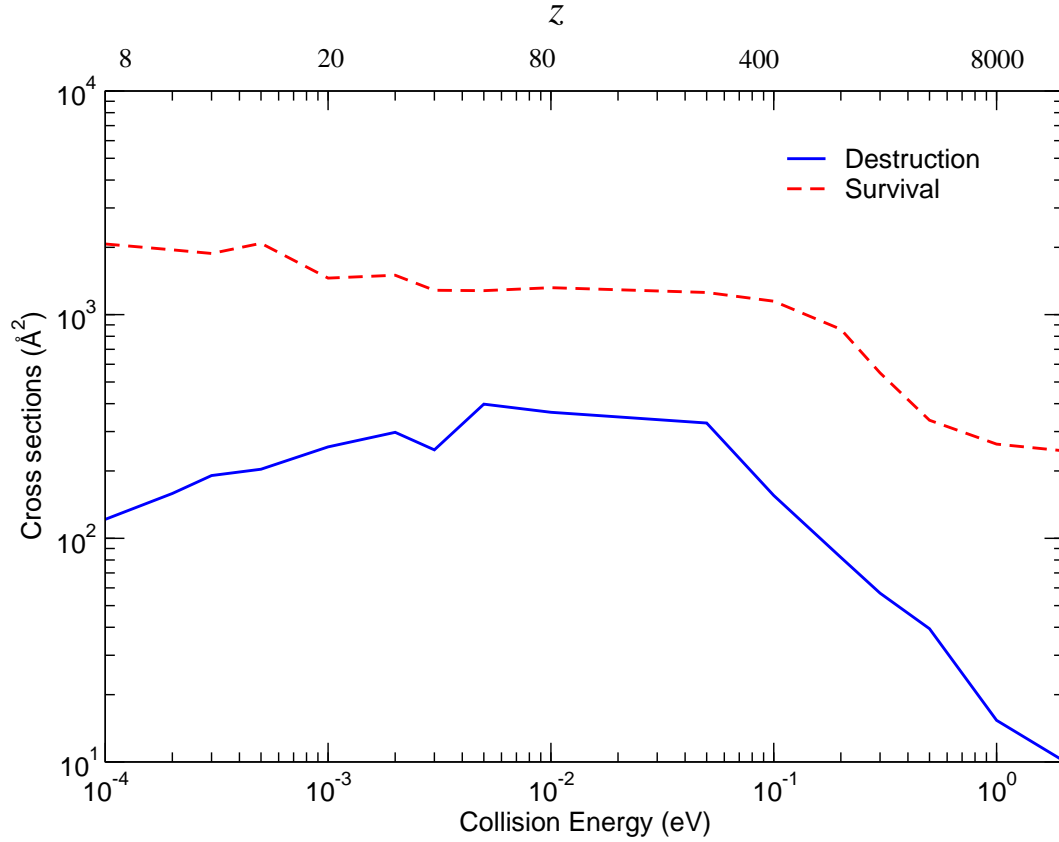


Figure 5.8 Computed final cross sections for the two different channels of reaction (2): destruction refers to  $\text{H}_2^+$  formation while survival refers to LiH preservation. See main text for details.

momenta has been used for the highest energy value (1.0 eV) to reach convergence for the corresponding cross sections. As can be seen from that figure the LiH survival process is the most likely one to occur at the considered energies, although the destruction of the LiH with  $\text{H}_2^+$  formation also yields fairly large cross sections. This suggests that reaction 5.6 is providing an additional (secondary) chemical evolution for the LiH molecule in relation to the primary destruction rates given by its reaction with neutral hydrogen atoms discussed in the previous section and given by eq. 5.5. This situation is seen to hold over the whole range of redshifts considered and we suggest it to be mainly caused by the presence of a stable complex formation near the reactants' region, the effect of which decreases the probability of final LiH destruction. The existing lower abundance of  $\text{H}^+$  compared to  $\text{H}$  also suggests this additional reaction likely to be less important than the primary destruction pathway [22]. On the other hand, the pathways indicated by eq. 5.6 can also provide a reactive channel leading to the formation of  $\text{H}_2^+$  molecules, a branch reaction that has not been considered in detail before but which our present calculations show to be associated with rather large reaction rates, as indicated by table 5.4.

Our computed thermal rate coefficients as function of both  $T$  and  $z$  are reported

T(K)	$\alpha(T)(\text{cm}^3\text{s}^{-1})$	T(K)	$\alpha(T)(\text{cm}^3\text{s}^{-1})$
10	1.18-09	300	5.44-09
20	2.07-09	500	6.27-09
30	2.75-09	800	6.09-09
50	3.34-09	1000	5.83-09
70	3.38-09	1200	5.61-09
100	3.29-09	1800	5.15-09
200	4.23-09	2000	5.04-09

Table 5.4 Computed rate coefficients summed over all final states of the products. The notation 1.20-09 corresponds to  $1.20 \times 10^{-09}$ .

by fig. 5.9 and listed in table 5.4: our values turn out to be slightly different from those estimated by Stancil [2] and those calculated by Pino et al. [23] and Bulut et al. [24]. Indeed, while their rates are nearly constant with energy in the energy range studied, we instead note that ours have a slight dependence on the temperature. In any event, over the redshift range relevant for Early Universe lithium chemistry ( $20 < z < 400$ ) our computed rates are also seen to be (panel in figure 5.9) nearly constant and to reach a value not much larger than that proposed by Stancil et al [2]: our value of  $5 \times 10^{-9} \text{ cm}^3 \text{ s}^{-1}$  is to be compared with his of about  $1 \times 10^{-9} \text{ cm}^3 \text{ s}^{-1}$ , one obtained from an indirect estimate.

The thermal rates at temperatures higher than 2000 K can be extrapolated by the following equation,

$$\alpha(T) = A_0(T)^a + A_1 \times (T)^b \exp\left(\frac{c}{T}\right) \quad (5.10)$$

with the following coefficients:  $A_0 = -1.23024 \times 10^{-7} \text{ cm}^3\text{s}^{-1}\text{K}^{-1}$ ,  $a = 1.45383$ ,  $A_1 = 1.23023 \times 10^{-7} \text{ cm}^3\text{s}^{-1}\text{K}^{-1}$ ,  $b = 1.45383$  and  $c = 0.00450459 \text{ K}$

All the features we found here indicate a sizeable but limited disappearance of LiH in collision with  $\text{H}^+$ , also a very abundant species in the redshift range considered. Although these findings confirm the above to be a likely secondary destruction mechanism, the final abundance of LiH may however not be markedly different from the one surmised by eq. 5.5, although still further reduced by reaction 5.6. Furthermore, the present reaction could also enrich the estimated abundances of  $\text{H}_2^+$ , a crucial molecule for the formation of  $\text{H}_2$ , and also considered often as alternative coolant. The rates we reported are found to be larger than those associated with the reactions reported by eq. 5.5, a finding which suggests that the destruction of LiH by  $\text{H}^+$  is in any event still a likely process to occur in the Early Universe chemical scheme.

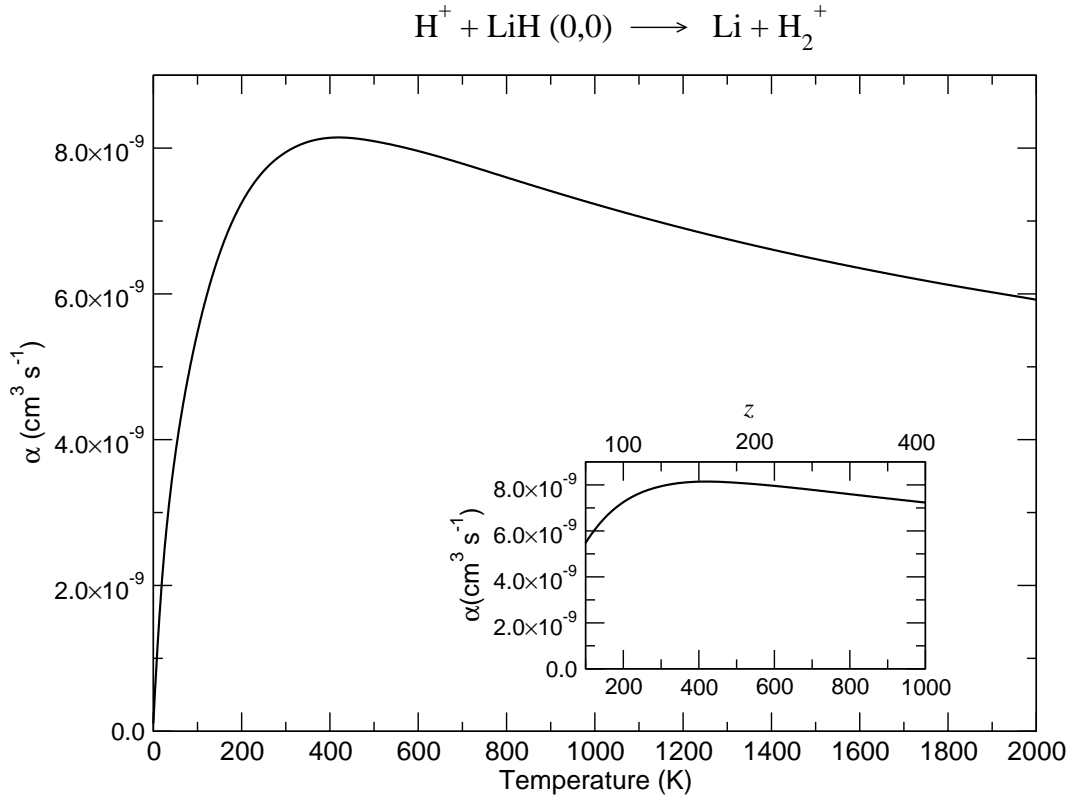


Figure 5.9 Computed thermal rate coefficients, as a function of temperature and redshift values, for the  $\text{H}_2^+$  formation channel in reaction 5.6. The redshift values are taken from Puy et al. [17]

### 5.1.3 $\text{LiH}^+ + \text{H}$ depletion

In the present instance we have analysed in some detail, and always employing a quantum treatment of the relevant processes, the different probabilities for the dynamical evolution of the molecular cation  $\text{LiH}^+(^2\Sigma^+)$  in collision with hydrogen atoms,  $\text{H}(^2\text{S})$ .

The questions which we intend to answer with the quantum reaction (that we consider as occurring on the lowest potential energy surface (PES) described earlier), are the following:

1. how probable is the disappearance of the initial cation by exothermic reaction with the surrounding H atoms?
2. are there other channels that preserve/reduce the presence of  $\text{LiH}^+$  as alternative pathways to the primary reactions? if so, how important are they in the range of redshift values of interest?
3. more technically, is the choice of different angular momentum coupling schemes affecting the above findings enough to be changing significantly our present conclusions?

The results reported in the two panels of figure 5.10 provide an answer to the above questions by showing the computed values of reactive (depletion) and elastic (survival) cross sections obtained through the computational schemes outlined in section 3.3.1. The energy range of interest here is very close to threshold, since it maps the region of the expected redshift ( $z$ ) values of the lithium chemistry in the early universe ( $z < 400$ ). The convergence of the locally adiabatic, coupled states approximation (CSA) rovibrational states has been checked and found to be reached for a basis set of 150 states (10 rotational states for each of the 15 vibrational states). The calculations have been made also by considering the convergence over  $J$  (ranging from 6 to 40 for the highest energy). After studying the potential range, we set the  $V_{\text{NIP}}$  parameters  $r_{\text{min}} = 4.0$  and  $r_{\text{max}} = 7.5$  atomic units to be sure to absorb all reactive flux and to minimize total reflection of products. It is worth noting that these calculations were made employing a rather different code which implements a simpler version of the NIP approach compared with our.

The panel on the left in figure 5.10 shows results for which both the centrifugal sudden (CS) and the energy sudden (ES) approximations have been employed during the reactive dynamics, i.e. the assumptions have been made that rotational/vibrational channel spacings affect cross sections only marginally and that there is no rotor re-orientation during the collisional events (reactive IOSA-NIP scheme). Both approximations greatly simplify the computational efforts, while their possible validity in the present case will be further analysed below.

At the R-IOSA level of quantum recoupling, therefore, we see that the survival (elastic) probability for  $\text{LiH}^+$  (dotted line) is the markedly dominant process: in other words, the strong exothermicity of the reaction imparts a very large kinetic energy increase between product partners after formation, thereby favouring fast recoil of the light species that reduces bonding rearrangements.



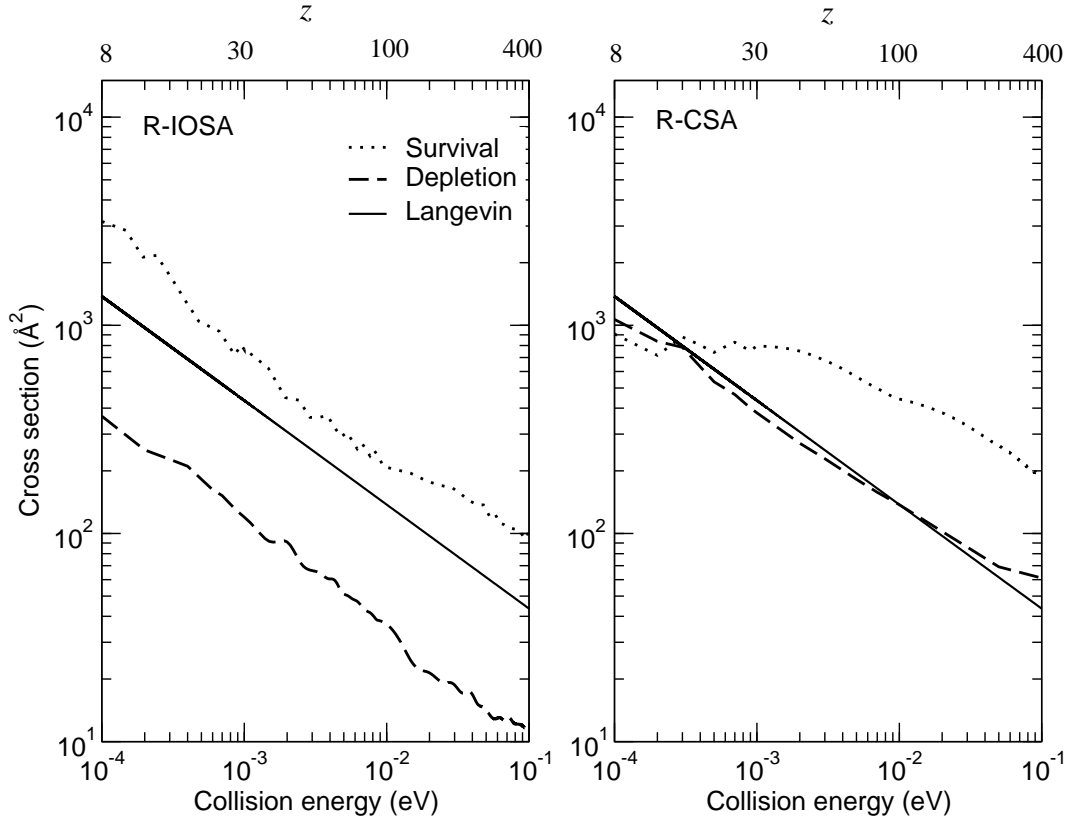


Figure 5.10 Reactive scattering cross sections for R-IOSA (left) and R-CSA (right) methods. We report in the same figure the Langevin cross sections estimated according to Levine [25]. Redshift ( $z$ ) values are extracted from Puy et al [17].

The solid line, on the same left panel of figure 5.10, clearly shows at low energies, the strongly exothermic nature of the present reaction as given by the simple modelling of the process which corresponds to the Langevin capture approximation [25]; this reactive model is well-known to usually provide an upper bound to the more realistically calculated cross sections and we indeed see here that the Langevin model yields values which are much larger than those given by the computed reactive process, i. e. by the dashed line reporting the probability of the depletion reaction.

When we now improve on the quantum dynamics by removing the ES approximation from our calculations, we obtain the R-CSA results shown on the right panel of figure 5.10. The same three types of processes are described there, with the same notation as that of the left-side panel. We can now make the following comments:

1. the survival reaction still remains the dominant process;
2. the disappearance of  $\text{LiH}^+$  and the  $\text{H}_2$  formation, the depletion process of eq. 5.7, now becomes markedly bigger: it is now about four times larger than that from the R-IOSA calculations and follows closely the estimates from the Langevin approximation.

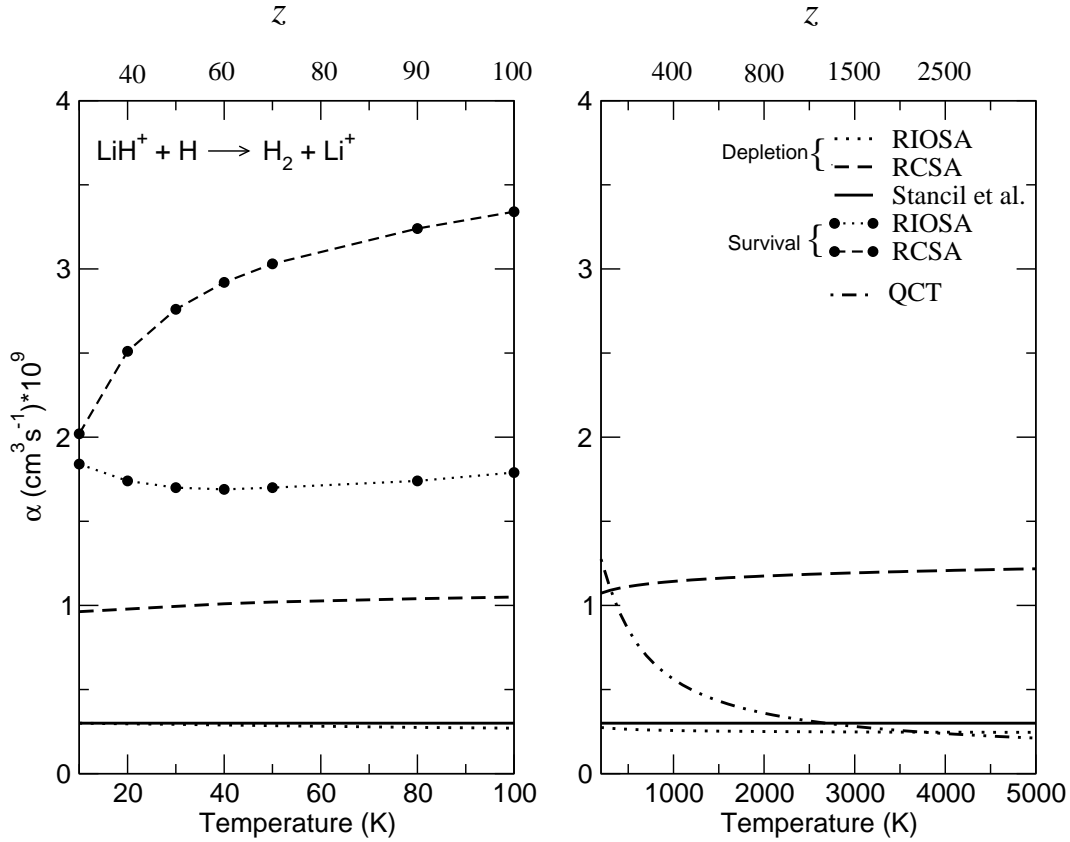


Figure 5.11 Comparison of computed rate coefficients from different methods, indicated by the caption on the right panel. The QCT reactive rates are from [23]

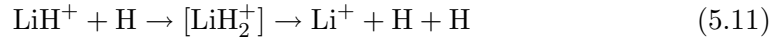
In other words, to employ the more accurate RCSA scheme makes for a more realistic treatment of the reaction dynamics and greatly favours the product redistribution over the final, well separated, different states of  $\text{H}_2$  which become energetically open during the reaction. On the other hand, the survival (elastic) probability is not greatly affected by improving on the RIOSA simplification and persists in remaining the process with the largest associated cross sections, especially at  $z$  values from 40 to 400 (the  $z$  values present in fig. 5.10 and fig. 5.11 are those provided by Puy et al [17]).

In order to make possible an even more direct comparison with reaction (depletion) rates, and over a larger range of temperatures, we report in the two panels of figure 5.11 our present calculations and the earlier estimates [2]. The two different coupling schemes are seen to yield different results: the depletion rates from the IOS scheme (the R-IOSA results: dots) and those using the CS scheme (the R-CSA data: dashes) differ at low temperatures ( $z < 400$ ) by about a factor of 4, although remaining in both cases of the order of  $10^{-9} \text{ cm}^3 \text{ s}^{-1}$ . The earlier estimates by Stancil et al [2] (solid line) are very close to the RIOSA calculations while smaller than the data from the more accurate quantum dynamics (R-CSA). No semiclassical results exist at such low temperatures. On the other hand, the R-CSA/R-IOSA calcula-

tions for the elastic (survival) rates are clearly providing the largest probabilities reported at low T. The actual, computed values of the rates at low temperatures are also given by Table 5.5, showing both the elastic (survival) and reactive (depletion) values discussed here.

The further extrapolation to higher temperatures is shown by the data on the right-side panel in the same figure 5.11. We see there that the relative differences between depletion rates indicated at low T still persist and that the dynamically more realistic R-CSA rates remain by far the process with the largest values. Recent semiclassical calculations using the same PES (Pino et al. 2008) show a stronger T-dependence in the higher temperature region becoming essentially coincident with our R-IOSA results at T values from around 3000 K and above. On the other hand, at the higher temperatures the more realistic R-CSA coupling scheme still remains the best and provides depletion rates which are consistently larger. In sum, all calculations indicate depletion rates in the range of  $10^{-9} \text{ cm}^3\text{s}^{-1}$ , to depend little on temperature changes and to remain smaller than the survival rates of the  $\text{LiH}^+$  cationic species. This is therefore an important piece of quantitative information on the title reaction that is being made available by the present ab-initio calculations.

It is also interesting to note here that the semiclassical calculations [23] were able to provide information on the three-body break-up channel:

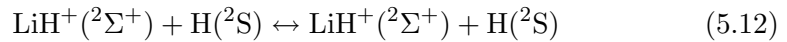


since the energy gained during the exothermic process is only slightly less than the full fragmentation of the partners, i.e. than the collision-induced dissociation (CID) channel. They found there that the CID channel is essentially important as a high energy, high temperature channel which becomes dominant with respect to depletion only above 1000 K. Hence, we can say that formation of  $\text{LiH}^+$  at small  $z$  values implies that its survival remains the more probable process with respect to reactive depletion, while at higher T values the CID pathway gains importance and significance, thereby successfully competing with survival of the  $\text{LiH}^+$  molecular ion.

These results, as further discussed below, have direct implications on the possible observational data at low- $z$  for the early universe model.

Our present findings could be summarized in the following way:

- The survival process, whereby  $\text{LiH}^+$  does not get destroyed by reactions with the surrounding H atoms



is found to be the most likely process at low-T, indicating that, because of specific features of their reactive PES [14], the two partners undergo essentially repulsive interaction at short-range in the product region, due to the marked increase of the products' relative kinetic energy, while the more stable bound complex ( $\text{LiH}_2^+$ ) is formed within a range of distances which correspond to the reactants' region [26]

- The depletion reaction (eq. 5.7), remains however an important reactive process which leads to the disappearance of  $\text{LiH}^+$  cations initially formed during

T(K)	$\alpha^d(T)_{RIOSA}(\text{cm}^3\text{s}^{-1})$	$\alpha^d(T)_{RCSA}(\text{cm}^3\text{s}^{-1})$	$\alpha^s(T)_{RIOSA}(\text{cm}^3\text{s}^{-1})$	$\alpha^s(T)_{RCSA}(\text{cm}^3\text{s}^{-1})$
10....	3.00-10	9.63-10	1.84-09	2.02-09
20....	2.96-10	9.78-10	1.74-09	2.51-09
30....	2.93-10	9.94-10	1.70-09	2.76-09
40....	2.89-10	1.01-09	1.69-09	2.92-09
50....	2.85-10	1.02-09	1.70-09	3.03-09
80....	2.75-10	1.04-09	1.74-09	3.24-09
100..	2.70-10	1.05-09	1.79-09	3.34-09

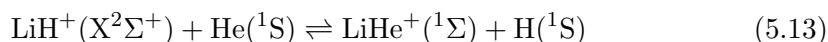
Table 5.5 Computed depletion (summed over all final states of the products) and survival (elastic) rate coefficients,  $\alpha^d$  and  $\alpha^s$ , respectively. The notation 3.00-10 corresponds to  $3.00 \times 10^{-10}$ .

the recombination era. In other words, we find from our calculations that the exothermic process is indeed the dominant reactive process that leads to density reduction for the cationic hydride;

- As the temperature increases, the 3B break-up process has been shown to become more important, as surmised by the calculations of Pino et al [23], thereby leading to the disappearance of the  $\text{LiH}^+$  that survived the exothermic depletion reaction discussed before.

#### 5.1.4 $\text{LiH}^+ + \text{He}$ depletion and inverse reaction

In our approach the reactive scattering involving the forward and backward reactions



reduces to the solution of two separate inelastic scattering problems: one in the conventionally labelled reagent arrangement (left side of eq. 5.13) and the other in the product arrangement (right side of eq. 5.13). This means that two separate sets of parameters have to be tested in order to reduce the relative error of the calculated reactive cross sections within 1%. Starting with the reagents' arrangement, the length of the basis set expansion given by eq. 3.23 is 400 leading to an equal number of coupled equations. At each propagation sector, a converged set  $\varphi_a$  of molecular basis functions has been obtained by variationally solving eq. 3.24 and expanding the  $\varphi_a$  over a direct product of a Colbert-Miller discrete variable representation (DVR) of 150 points (ranging from  $0.75 a_0$  to  $15.0 a_0$ ) and a set of 43 spherical harmonics. In the case of the reagents' arrangement the R-Matrix has been propagated to  $45.0 a_0$  by using 654 sectors. Considering now the inverse reaction for the products' arrangement, the total wave function reported by eq. 3.23 is represented by a linear expansion of 500 elements giving an equal number of coupled equations. A converged  $\varphi_a$  basis has been obtained at each sector by using a direct product of a Colbert-Miller discrete variable representation (DVR) of 150 points (ranging from  $0.75 a_0$  to  $15.0 a_0$ ) and a set of 65 spherical harmonics. In this case the R-Matrix has been propagated up to  $130.0 a_0$  by using 843 sectors. The calculations were carried out over a wide range of energies, from  $10^{-5}$  to  $1.0$  eV, and for total angular momentum values ( $J$ ) ranging from 10 to 135 for the highest energy of the direct reaction and up to 65 for the inverse one. The NIP parameters were tested following the Baer criteria [27]: the NIP stability has been reached for  $r_{\min} = 7.75a_0$ ,  $r_{\max} = 11.25a_0$ , and the NIP order  $n = 2$  in both cases.

We have employed the NIP approach to generate first the corresponding reaction probabilities for the destruction reaction involving  $\text{LiH}^+$



and the data collected by figure 5.13 report these probabilities over a broad range of collision energies (given in eV) and for different values of the reagent molecule's vibrational energy content: one should notice here that the  $v=1$  and  $2$  initial states overcome the endothermic barrier into the products (e.g. see figure 5.12) and therefore the probability values can be obtained from the zero energy threshold.

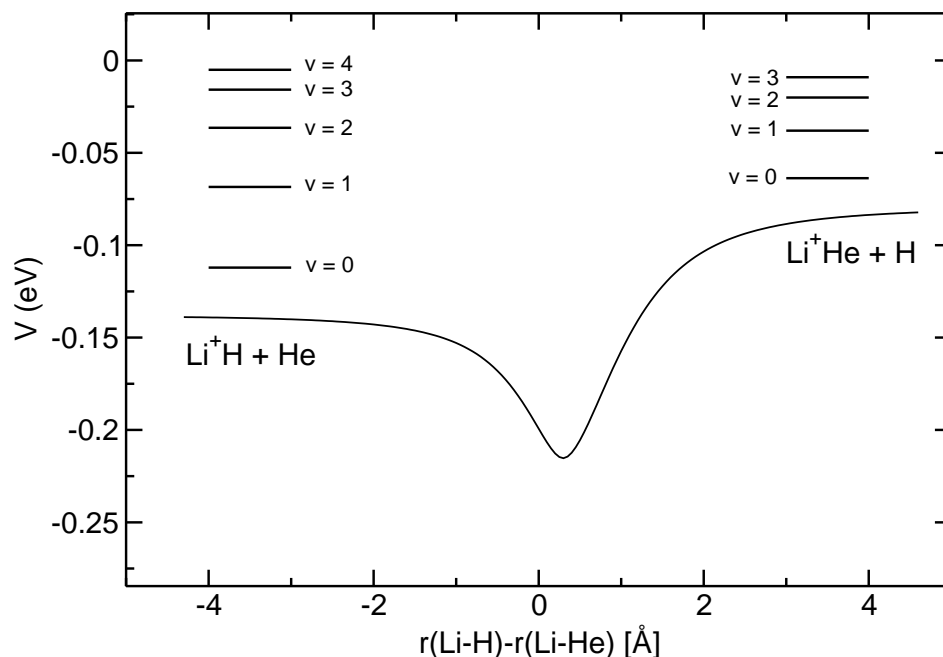


Figure 5.12 Collinear profile of the RPES computed in ?? for the present system. On the two sides of the reaction the energy spacings of the diatomic partners are shown:  $\text{LiH}^+$  ( $X^1\Sigma^+$ ) left and  $\text{LiHe}^+$  ( $^1\Sigma^+$ ), right. See text for further details.

Two interesting features are detected from that figure: (i) the presence of strong resonant oscillations near threshold for the  $v=0$  case, and (ii) the marked increase of the probability values at low energies as  $v$  changes from  $v=0$  to  $v=2$ .

The threshold resonances in the  $J=0$  channel will be further discussed in the next section in greater detail, while the marked increase of the reaction efficiency for vibrationally excited molecular partners indicates the presence of an insertion reaction, i.e. the incoming He atom chiefly interacts with the ionic side of the molecule, inserting itself between  $\text{Li}^+$  and H. This mechanism therefore favors a more efficient H atom detachment when that bond is stretched and the  $\text{Li}^+$  becomes a more "isolated" partner for the helium atom.

We followed a similar study for the inverse reaction that leads to the production of  $\text{LiH}^+$ , presenting the results in figure 5.14



One of the first differences for the probabilities of the inverse reaction is provided by greater values of such probabilities in the low-energy region in comparison with those of figure 5.13. These data indicate that exothermicity does play a significant role and

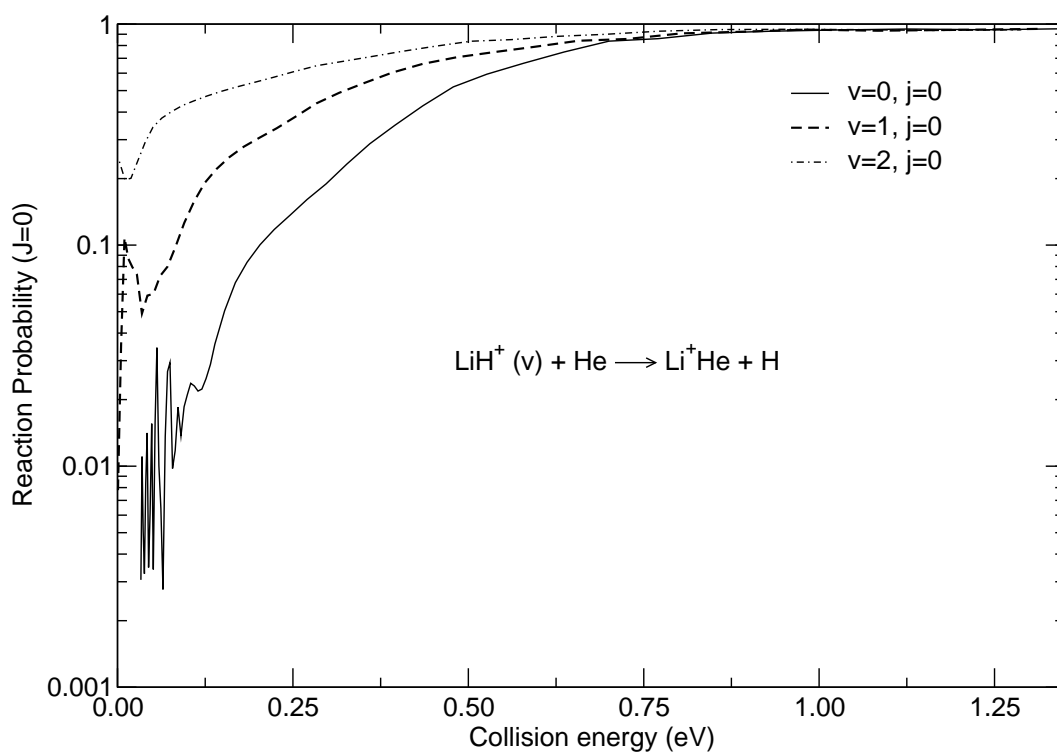


Figure 5.13 Computed reactive probabilities ( $J = 0$ ) for the  $\text{LiH}^+$  depletion reaction at low collision energies. The curves correspond to different vibrational states of the ionic partner in the reactant region. See text for further details.

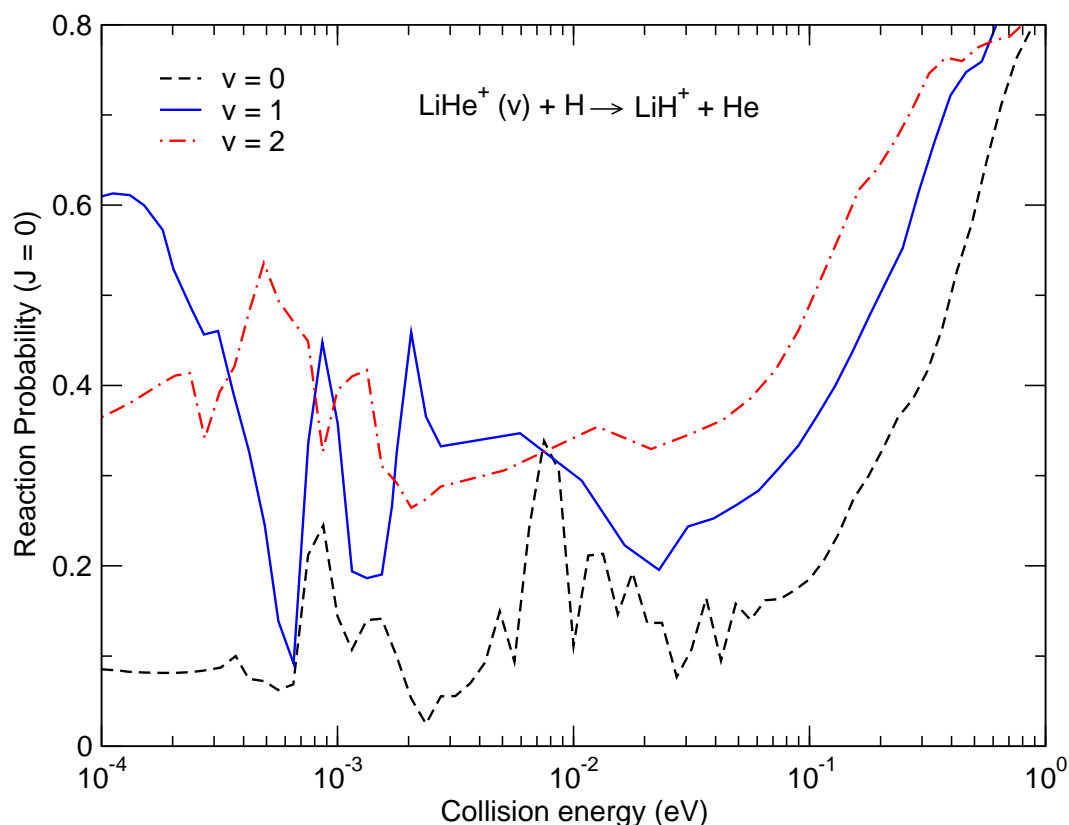


Figure 5.14 Computed reaction probabilities for the inverse, exothermic reaction leading to  $\text{LiH}^+$  formation. The different curves correspond to different vibrational states of the reagent ion  $\text{LiHe}^+$ . See text for further details.

that the fact that the reaction can start right up from zero collision energy implies a greater efficiency of the product formation. Furthermore, the inverse reaction is still an insertion reaction since the probabilities markedly increase as the vibrational energy content of the initial  $\text{LiHe}^+$  increases: this time is the H atom which interjects the existing bond, separating the nearly neutral He atom from the ionic partner  $\text{Li}^+$ . Additionally, we see the clear presence of resonant structures at very low energies (i.e. between  $10^{-3}$  and  $10^{-1}$  eV), all features that we shall be discussing below in more detail.

The corresponding reaction cross sections, i.e. the dynamical quantities which are now summed over all the contributing  $J$  values, as mentioned before, are now given in figures 5.15 and 5.16.

The data of figure 5.15 show very clearly the difference between a reaction with an energy threshold (i.e. the process with  $\text{LiH}^+$  in its  $v=0$  initial state) and one without, which is obviously fairly efficient at low collision energies and remains always larger than the reactions with the  $v=0$  initial state of the cation.

On the other hand, the inverse reaction that involves the formation of  $\text{LiH}^+$  from existing  $\text{LiHe}^+$  quantities, shown by the data of figure 5.16, clearly indicates how



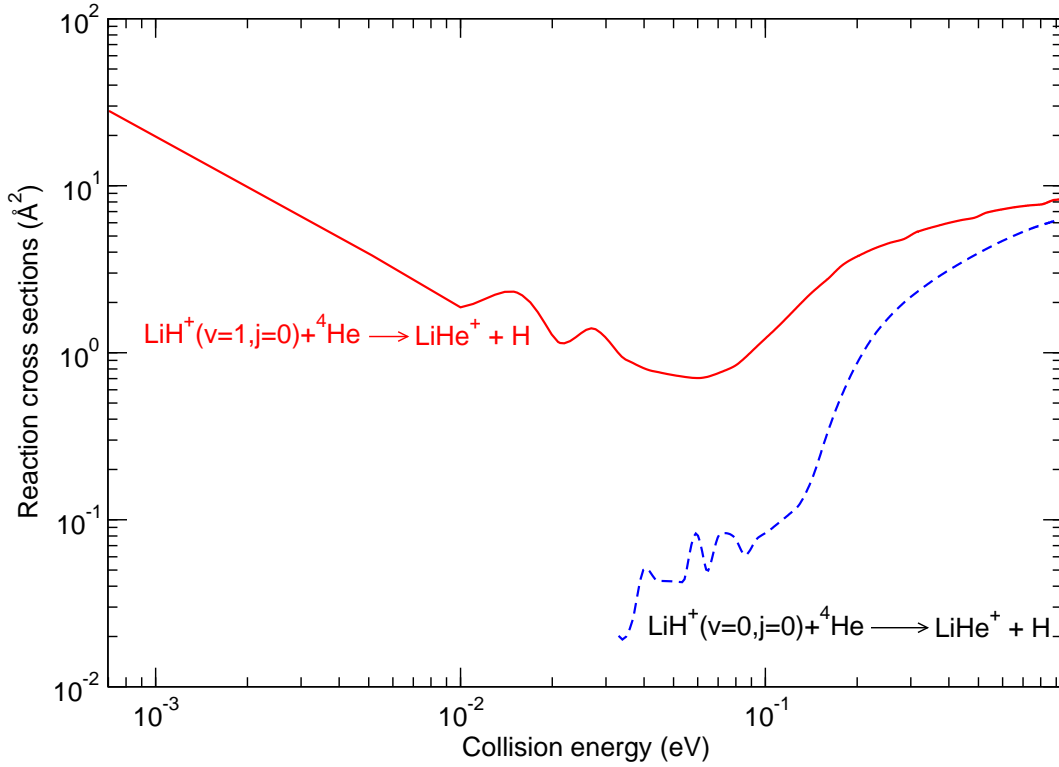


Figure 5.15 Computed reaction cross section for the depletion reaction of  $\text{LiH}^+$  with He. Two different initial states of the ionic reagent are shown. See text for further details.

much larger these cross sections are when compared with the destruction process: between  $10^{-2}$  and  $10^{-3}$  eV of energies, in fact, one sees that the formation process is on average two orders of magnitude larger than the depletion reaction depicted by figure 5.15.

Furthermore, we see that the cross sections for the formation process of the lithium hydride cation also suggest very strong oscillating structures at low energies which do not exist for the same range and to the same extent in the case of the  $\text{LiH}^+$  ( $v=1$ ) depletion process. We shall analyse such features later on, while noticing now the clear importance of complex formation during this exothermic process.

On the whole, therefore, we see that the formation reaction for  $\text{LiH}^+$  via the He-route outlined here corresponds to a much more favorable process than the one involving depletion of  $\text{LiH}^+$  ( $v=1$ ) via the same route, a feature that will be further discussed below.

Another important quantity that one needs to consider when modeling possible chemical paths involving  $\text{LiH}^+$  and other chemical species in the early universe environment is the behavior of the computed reaction rates from the available cross sections:

$$\alpha(T) = \left( \frac{8k_B T}{\pi \mu} \right)^{1/2} \frac{1}{(k_B T)^2} \int_0^\infty \sigma_{a \rightarrow \text{all}}(E) \exp(-E/k_B T) E dE \quad (5.16)$$

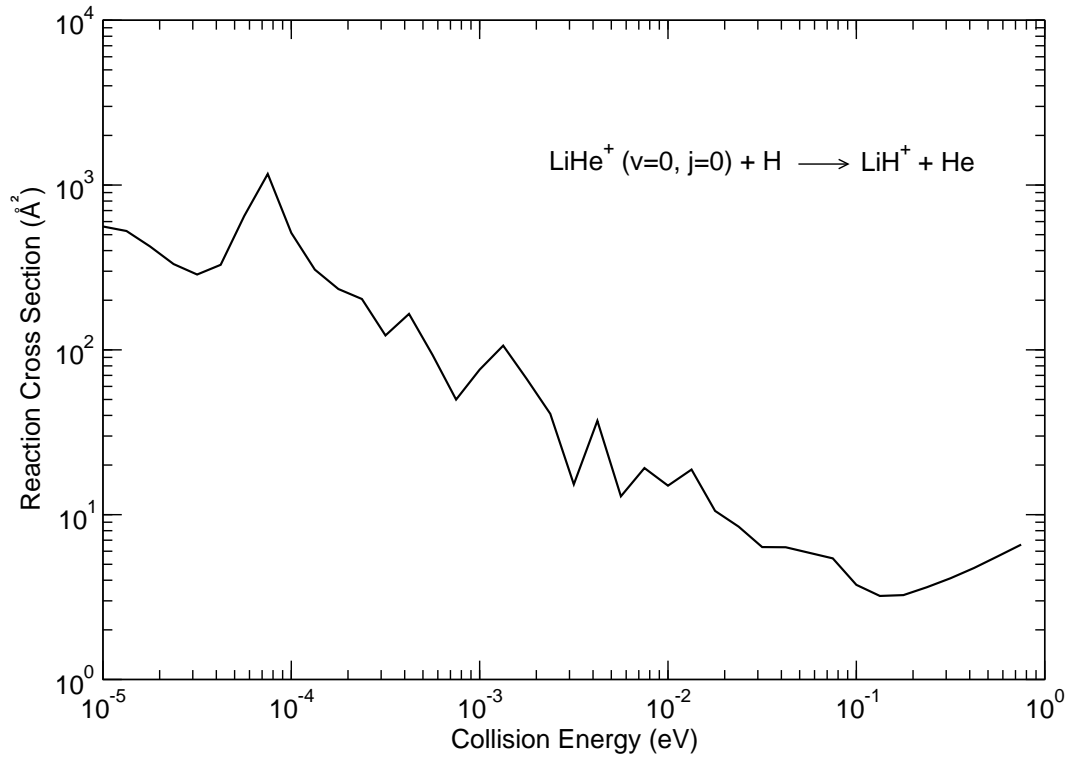


Figure 5.16 Computed reaction cross sections for the exothermic formation process of  $\text{LiH}^+$  from  $\text{LiHe}^+$  cations. See text for further details.

where  $\sigma_{a \rightarrow \text{all}}$  stands for the computed values of the reactive cross sections indicated in the previous subsection,  $|a\rangle$  labeling the initial states of the reaction partners and "all" indicating all the final states of the reaction contributing to the flux losses in the S-matrix as obtained from the NIP approach discussed in the section 3.3.1. In the present examples only the initial vibrational state of the ionic molecular reaction may change, while no changes of the electronic state are considered in the present study: they are all out of reach for the temperatures we are considering in this study.

The results of figure 5.17 and 5.18 report the calculated values of reaction rates (in units of  $\text{cm}^3\text{s}^{-1}$ ) over temperature ranges between 0.1 and 1000 K.

The data reported by figure 5.17 show again the marked effect of the energy threshold: below 50 K only having  $\text{LiH}^+$  in its  $v=1$  initial level contributes to the depletion process, which is now coming from an exothermic reaction and appears to be very efficient.

It is interesting to note, in fact, that our calculated rates for  $\text{LiH}^+$  depletion in reaction with H (sec. 5.1.3) in the same range of temperatures as those of figure 5.17, also depend very little on T and are of the order of  $10^{-9} \text{ cm}^3\text{s}^{-1}$ , while the present value for  $\text{LiH}^+$  ( $v=1$ ) is around  $7 \times 10^{-11}$ , i.e. more than one order of magnitude slower. In other words,  $\text{LiH}^+$  ( $v=1$ ) is certainly not very abundant in the early universe environments and the present study further indicates its depletion by He to be a less efficient process than that caused by the more abundant H atoms in

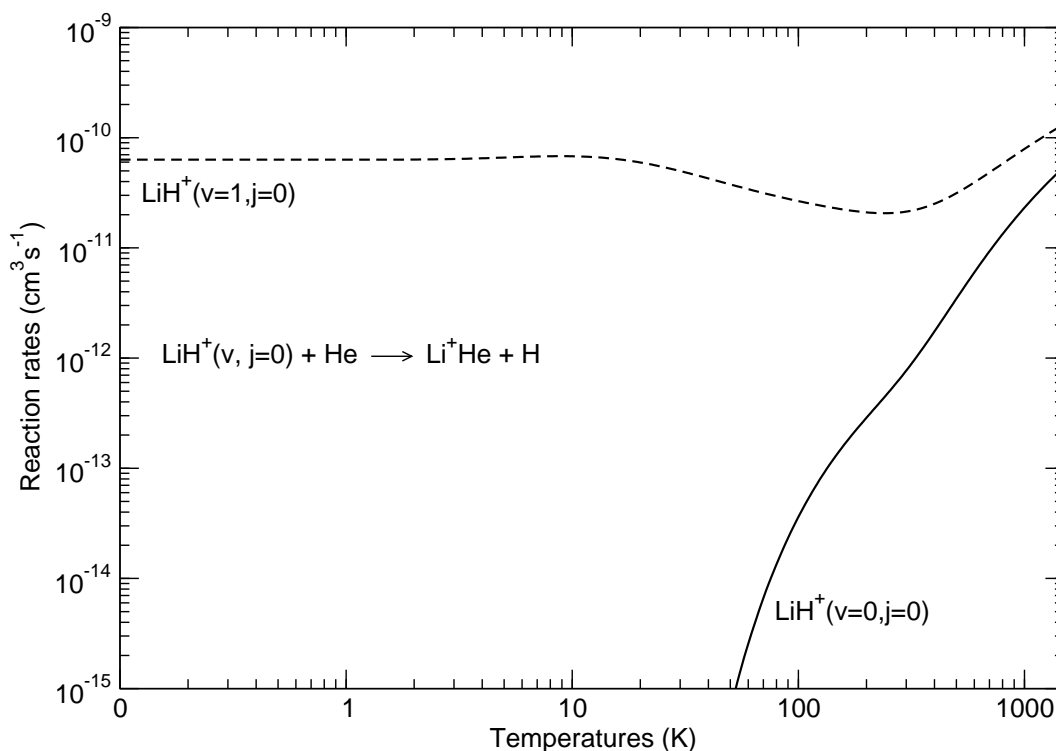


Figure 5.17 Computed reaction rates for the  $\text{LiH}^+$  depletion reactions as a function of the initial vibrational state of  $\text{LiH}^+$  and for the considered range of temperatures. See text for further details.

that environments. Thus, the present chemical route could be considered not to be seriously competing chemical route to the disappearance of the initially formed  $\text{LiH}^+$  molecular ions.

The corresponding rates for the fully exothermic inverse reaction, that of the lithium hydride cation formation, are reported by our data in figure 5.18, for two different initial states of  $\text{LiHe}^+$ . The slow dependence of this ionic reaction on  $T$  over that range of the chosen values is clear from the figure and confirms the findings for  $\text{LiH}^+$  5.1.3: the rates vary by less than a factor of three over a  $T$  span of about three orders of magnitude.

Our data also indicate that formation of  $\text{LiH}^+$  from this route is an interesting possibility as the rates are of about the same order of magnitude as those shown by the corresponding  $\text{LiH}^+$  destruction by  $\text{H}$  (see sec. 5.1.3) and nearly two order of magnitude larger than the  $\text{LiH}^+$  destruction by  $\text{He}$ . Thus, one may say that once  $\text{LiHe}^+$  is formed in any reasonable amount, its chemical route to  $\text{LiH}^+$  formation in reaction with  $\text{H}$  would be a barrierless, exothermic reaction with rather substantial rates that should be considered for the evaluation of fractional abundances of both  $\text{LiH}^+$  and  $\text{LiHe}^+$ .

Because of the current general interest in ionic reactive processes at low and ultralow energies, we thought it to be useful to carry out a more detailed analysis

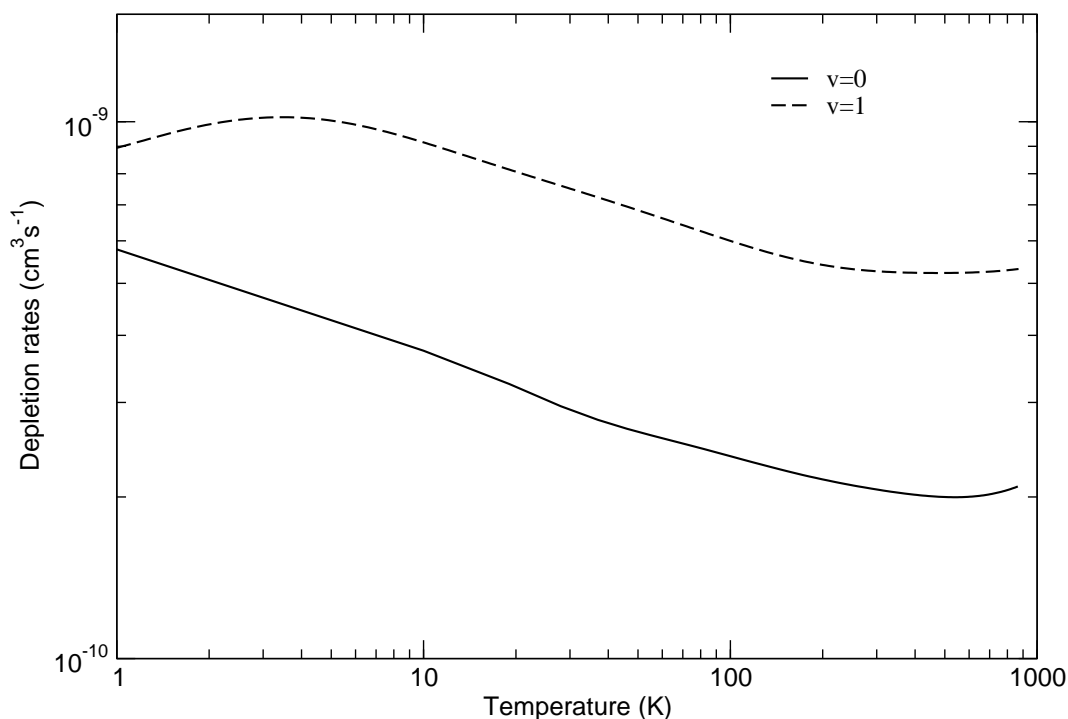


Figure 5.18 Computed reaction rates, as a function of  $T$ , for the formation of  $\text{LiH}^+$  from  $\text{LiHe}^+$  in reaction with  $\text{H}$ . Two different initial vibrational states of  $\text{LiHe}^+$  are considered.

of the possible features of the pure reaction probabilities for the  $J = 0$  component, which is the dominant one at energies from and below the meV range, in order to connect our findings with the specific properties of the RPES in the strongest interaction region between reacting partners.

We have already seen from fig. 5.14 that the reaction probabilities for the  $\text{Li}^+\text{He}$  formation channel, i.e. the one exhibiting an energy threshold of about 50 meV, showed strong oscillatory structures in the region from about 38 to about 100 meV, with marked intensity peaks appearing at specific energy locations. Such structures are shown more in detail by the data reported by figure 5.19, where we see the energy range for which those marked peaks are present.

Additionally, the destruction reaction for the same molecule, the one already analysed in the previous subsections, also showed marked oscillatory behaviour of its  $J = 0$  reactive cross sections and such features are reported more in detail by figure 5.20

To better understand the molecular-level mechanisms presiding over those structural features, it is important to realize first that, as shown by figure 5.12, both reacting partners' arrangements for the two reactions of figures 5.19 and 5.20 go via a complex formation stage where the local interaction added to the asymptotic molecules is quite important. Such additional interactions, viewed as generating a set of adiabatic potentials for each reactive arrangement, i.e. both for  $[\text{LiH}^+ \cdots \text{He}]$

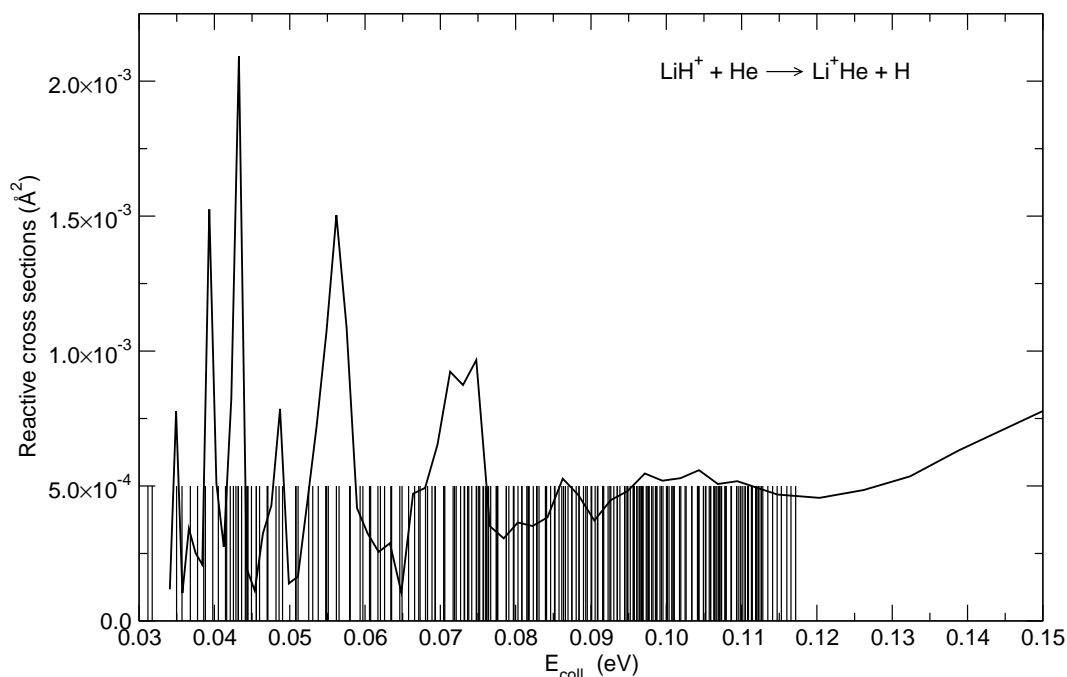


Figure 5.19 Computed reactive cross sections ( $J = 0$ ) for the formation reaction of  $\text{LiHe}^+$  at low collision energies. See main text for further details.

and  $[\text{LiHe}^+ \cdots \text{H}]$ , can be involved in the occurrence of Feshbach resonances at low collision energies, where it is more likely that the attractive energy added by the interactions at short ranges will cause the scattering complex to become locally bound as the system moves through the different adiabatic (vibrationally adiabatic) potentials for  $\text{LiH}^+ \cdots \text{He}$  in the formation reaction and for  $\text{LiHe}^+ \cdots \text{H}$  for the destruction reaction.

The data of figure 5.21 show pictorially the large set of such adiabatic potentials involving the vibrational states of the  $\text{LiH}^+$  partner.

One clearly sees there that over the shown range of collision energies the potentials which are asymptotically accessible become bound at short range, thereby causing the occurrence of probability-enhancing Feshbach resonances in the product channels. Due to the large number of such states supported by the potentials of figure 5.21, we only indicate in figure 5.19 their energy location without attempting any nanoscopic classification: it is clear from the data that several hundreds of such bound states exist and several of them can cause reaction probability enhancements at specific collision energies. As that energy increases, however, the system moves too far above the well depths and therefore the coupling necessary to generate such features decreases, causing the enhancement effects to disappear.

When a similar analysis is carried out for the destruction reaction structures of figure 5.20, the corresponding adiabatic potentials are given by figure 5.22. The different vibrational structure of  $\text{LiHe}^+$  is now causing a much larger number of adiabatic potentials to exist and therefore the corresponding structures in the reactive

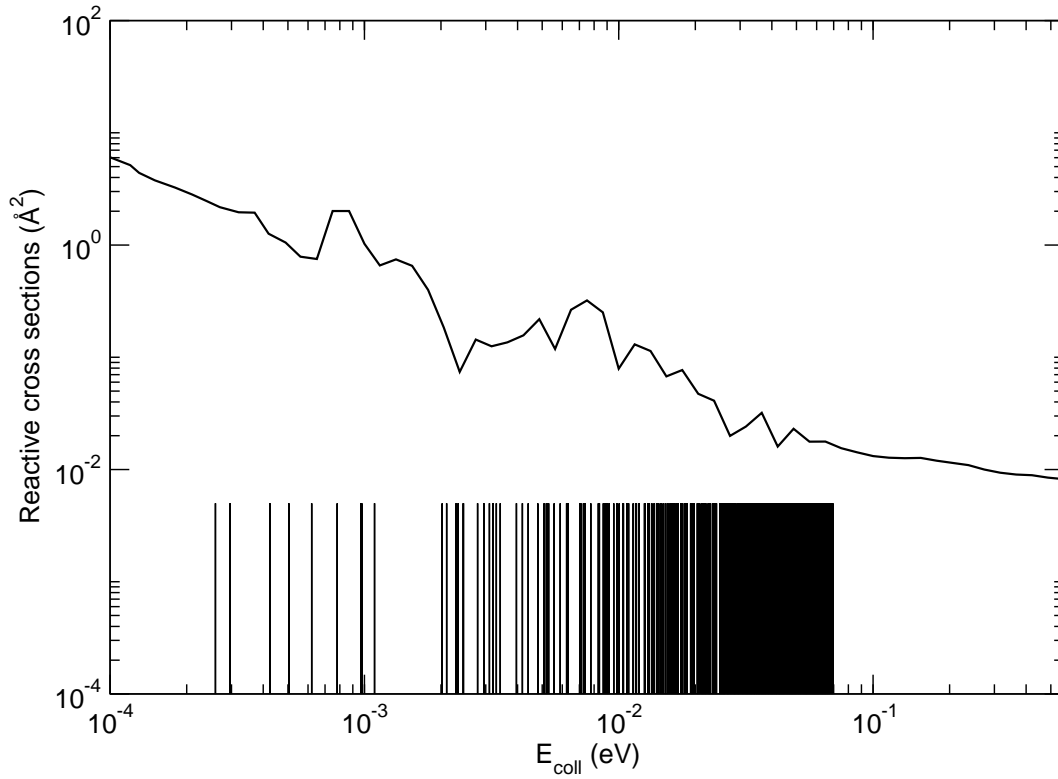


Figure 5.20 Same calculations as in figure 5.19, but this time for the inverse, destruction reaction for  $\text{LiHe}^+$ . See main text for further details.

cross sections can extend over a larger range of energies. Their positions are given by figure 5.20 and one indeed sees that they now cover a much larger energy range, causing much larger enhancements in the corresponding cross sections. One could therefore say that both complex-forming ionic reactions indicate the occurrence of several Feshbach-type resonances at vanishing collision energies for the  $J = 0$  case, some of which could also survive as structures when final cross sections are obtained (see figs 5.15 and 5.16).

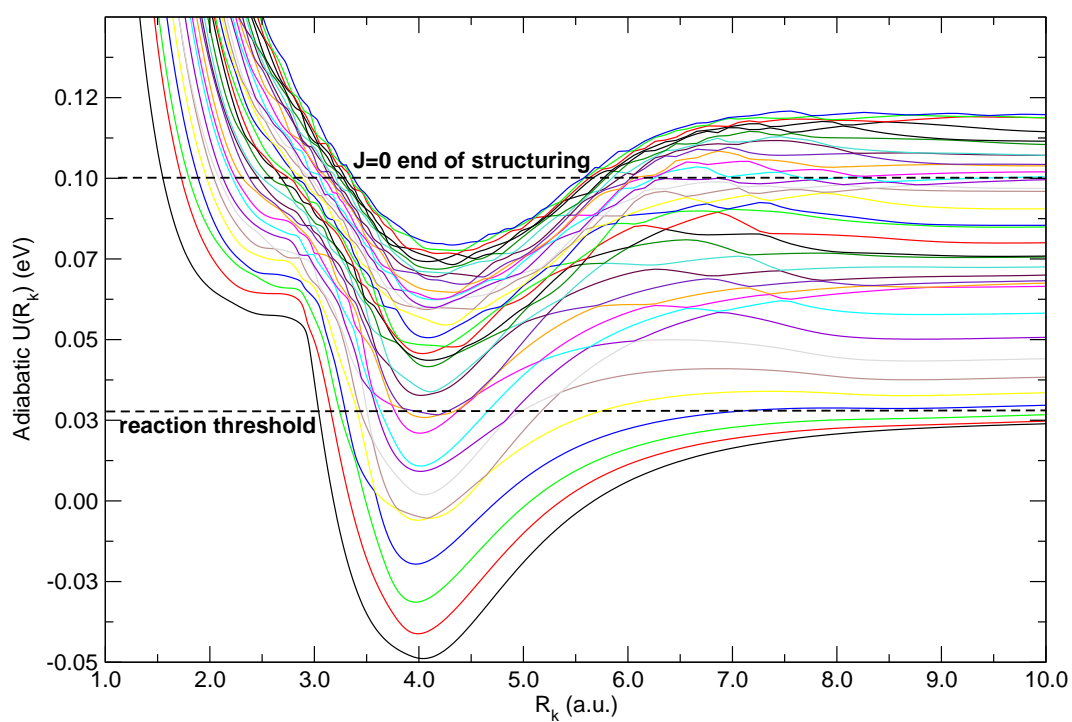


Figure 5.21 Computed adiabatic potential curves for the  $\text{LiH}^+ + \text{He}$  reaction. The two dotted lines indicate the range of energy covered by the reactive cross section structures in figure 5.19

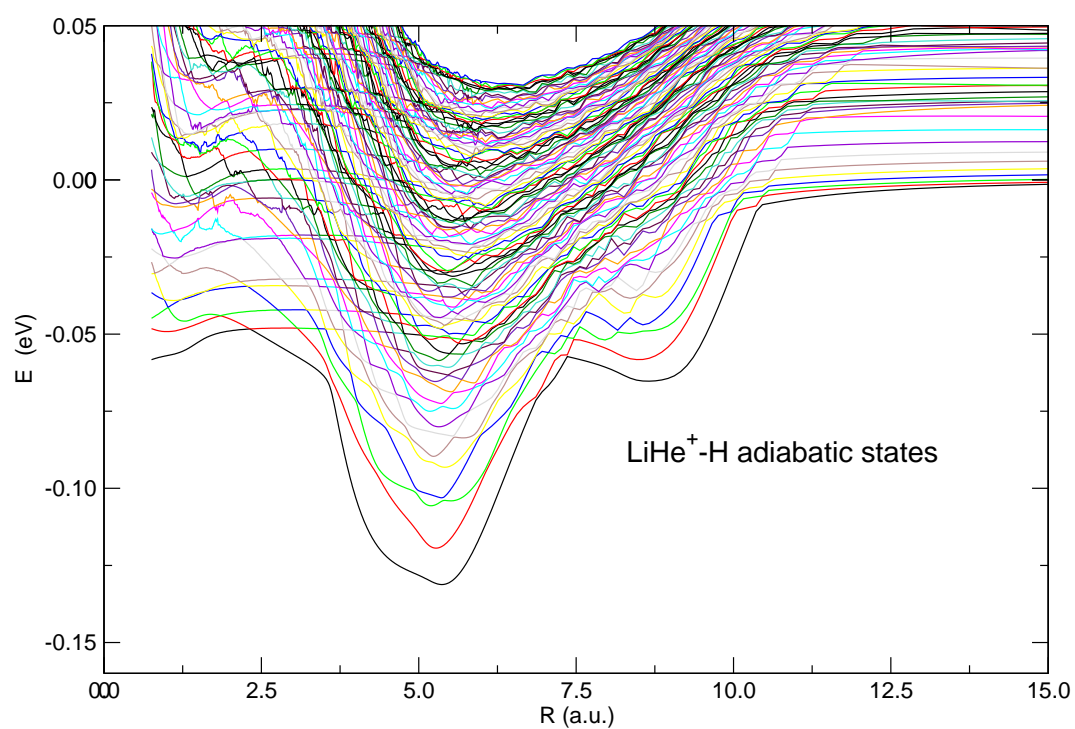


Figure 5.22 Same as in figure 5.21 but for the destruction reaction of  $\text{LiHe}^+ + \text{H}$ . See text for further details.



## 5.2 The $\text{HeH}^+$ : first molecule in the universe

The existence of  $\text{HeH}^+$  in astrophysical environments has been extensively discussed in several papers. Roberge & Dalgarno [28] surmised that  $\text{HeH}^+$  is produced in planetary nebulae and in dense molecular clouds under the presence of X-ray and extreme UV ionization sources. Liu et al. [29] investigated the possible detection of  $\text{HeH}^+$  in NGC 7027, a very high electron density nebular object, via its  $j = 1-0$  strong rotational line at  $149.14 \mu\text{m}$ , concluding that its identification is complicated by the accidental near-coincidence of that transition frequency with the  $149.09$  and  $149.39 \mu\text{m}$  lines of CH.

In the past few years, the presence of  $\text{HeH}^+$  in low temperature and low density helium-rich white dwarfs has been investigated. Harris et al [30] demonstrated that this molecule is the dominant positive ion in these objects and strongly affects their opacity. Engel et al [31], finally, showed that it might also be possible to detect  $\text{HeH}^+$  in cool helium stars such as those studied by Saio et al [32].

All models predict  $\text{HeH}^+$  to be abundant in gaseous nebulae (giant clouds of gas, which are the birthplace of stars) and in planetary nebulae (layers of gas ejected from dying stars). But despite this prediction, none of the several attempts to observe its extraterrestrial presence have been conclusive. The fact that  $\text{HeH}^+$  eludes observation means that either the mechanisms of creation of  $\text{HeH}^+$  are overestimated or that the mechanisms of its destruction are underestimated. As the production processes have already been extensively investigated, we focused on the destruction mechanisms, and in particular, on following reaction



### 5.2.1 The quantum calculations

A set of three-hundred coupled equations describing reaction 5.17 were solved using our, in-house code (described in chapter 4). A direct product of a Colbert-Miller discrete variable representation (DVR) of 100 points ranging from  $0.5 a_0$  to  $12 a_0$  for the reagent ion vibrational coordinate and a rotational basis of 40 spherical harmonics has been employed to describe the reactive complex. The solution matrix has been propagated up to  $50 a_0$  and the convergence was checked as a function of the propagator step-size, yielding a final convergence of cross-section values within about 1%.

The calculations were carried out over a wide range of energies, from  $10^{-6}$  to  $1.0 \text{ eV}$ , and for total angular momentum values ( $J$ ) ranging from 10 to 90 for the highest energy. The NIP parameters were tested following the Baer criteria (Baer et al. 1990): the NIP stability has been reached for  $r_{\min} = 2.75a_0$ ,  $r_{\max} = 5.75a_0$ , and the NIP order  $n = 2$ .

The results of figure 5.23 report the behaviour of the reaction probabilities as a function of the initial vibrational state of the molecular ion  $\text{HeH}^+$ . One clearly sees, from the computed probabilities for the process of eq. 5.17, the likely effects from starting the reaction with the  $\text{HeH}^+$  molecule in different vibrational states. The corresponding probabilities, in fact, change very little as the internal energy content

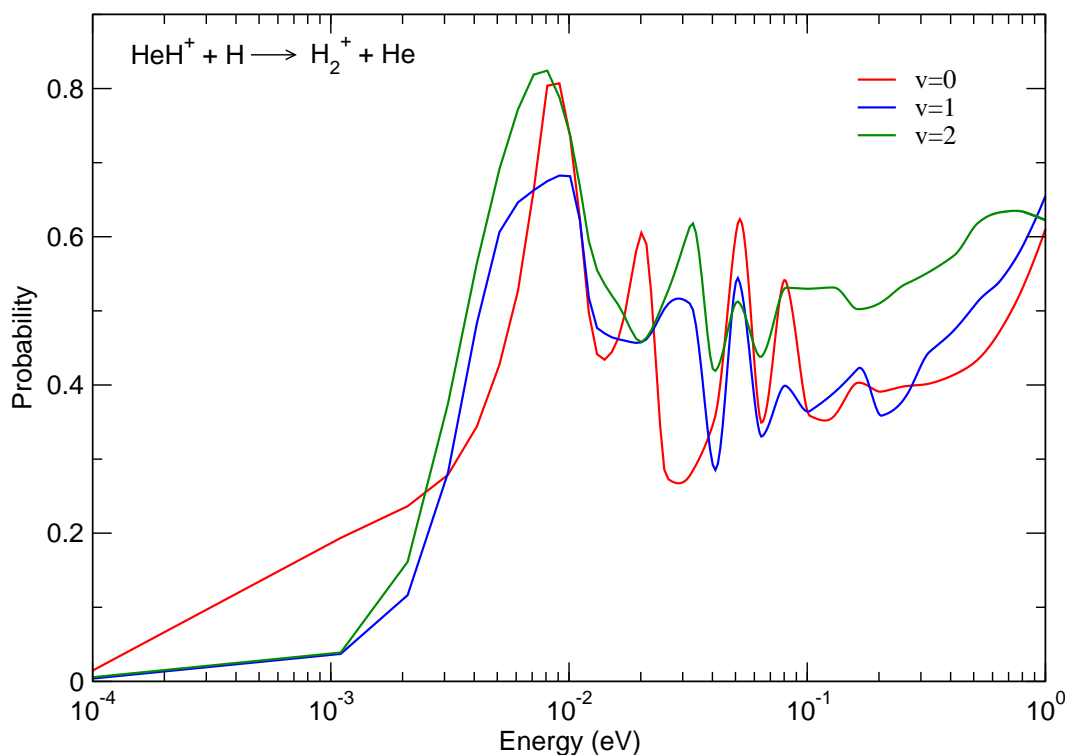


Figure 5.23 Computed reactive probabilities in function of collision energy  $E$  and for different initial vibrational states.

is increased and the presence of oscillatory structures for each initial channel (which we shall discuss later on) remains largely the same. This result indicates, at least in qualitative terms, that the dominant reaction path is very likely to be an extraction mechanism, whereby the  $\text{H}_2^+$  is formed with the "external"  $\text{H}^+$  of the ionic partner by the incoming H atom, with little influence from the He "spectator", therefore mostly involving a process that depends only marginally from the vibrational state of the initial, ionic molecular partner. This aspect has been discussed in greater detail for the endothermic channel of eq. 5.17, i.e. for the  $\text{H}_2^+$  destruction reaction, but less frequently for the exothermic,  $\text{HeH}^+$  destruction counterpart so that the present finding constitutes a useful addition to our overall understanding of the reactive behaviour of the present system. Our computed,  $J$ -converged integral cross-sections are presented in Figure 5.24.

From the figure, the non-Langevin behavior of the cross-sections for this ionic reaction is clear since, instead of independent of  $E$  at lower energies, they go through a marked maximum around  $10^{-2}$  eV. In the same figure, we report the experimental (thick line, from [33]) and the extrapolated (dotted line, from [34]) cross-sections that reach collision energy values as low as around  $10^{-2}$  eV. The agreement between our theoretical results and the experimental findings, both measured and extrapolated, is reassuringly good and confirms the physical reliability of the present NIP method for handling ionic reactions (sec. 4.2). No measured data are available at the lower collision energies as crossed beam experiments with ionic partners become

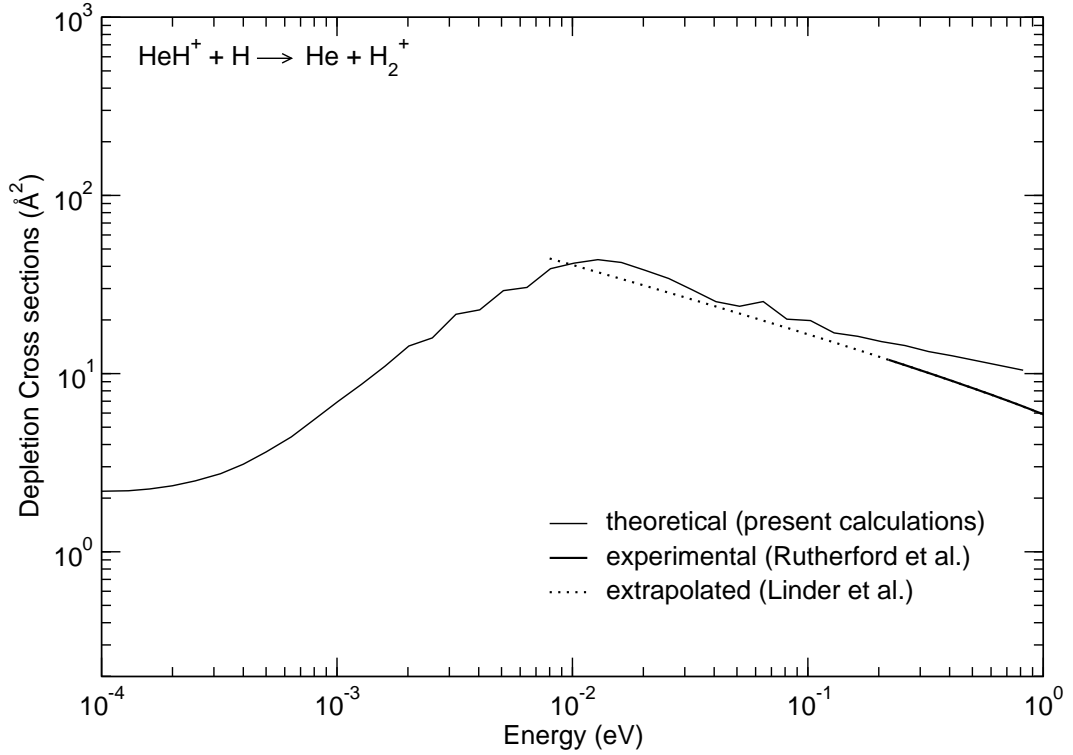


Figure 5.24 Computed integral cross-sections as a function of energy. The thick line represents the fitted experimental data from Rutherford & Vroom [33]. The dotted line is obtained from the formula given by Linder et al [34] by extrapolating the Rutherford's data.

increasingly difficult for that range.

### 5.2.2 Low energy behaviour

From the data reported by figure 5.25, where the energy range is extended down to  $10^{-6}$  eV, we see even more dramatically the presence of the strong, narrow peak appearing in the reaction probabilities at energies around a few  $\mu\text{eV}$ , i.e. at a possible temperature where trap processes could be analyzed.

It is interesting to note here that in a previous study on the behaviour in the limit of zero kinetic energy of a chemical reaction involving neutral partners [35]



has been also found that modifications of the RPES induced via artificial mass changes were able to show the appearance of a similarly strong peak in the products' channel at an energy of about  $3 \times 10^{-5}$  eV, i.e. very close to our findings in figure 5.25.

The analysis of the scattering matrix  $S(k)$ , with  $k$  being the associated wavenumber [36] for the process above, linked that behaviour with the occurrence of a virtual state as the relative kinetic energy approaches zero [35, 36]. The latter quantity appears when a pole of the  $S(k)$  matrix exists in the non-physical part of the Riemann

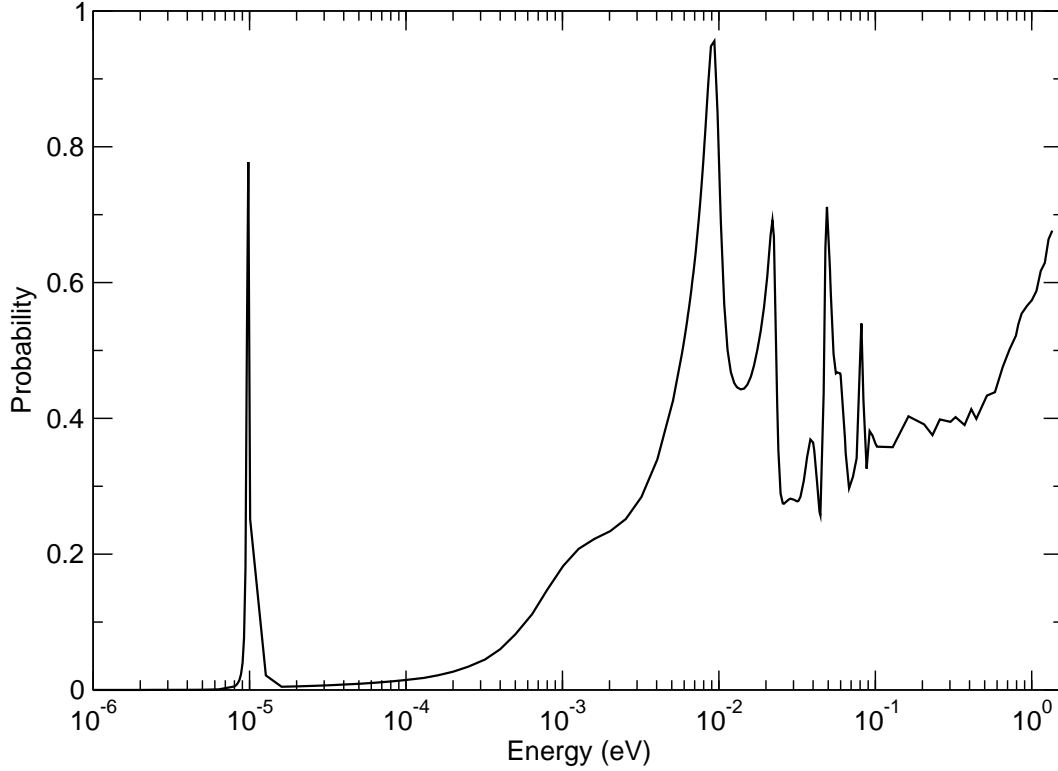


Figure 5.25 Computed reaction probabilities for process 5.17 at ultralow energies. The dominant  $J=0$  opacity contribution is shown in the figure.

surface (for  $Im(k) < 0$ ) [37]. In the case of multichannel scattering, therefore, the virtual state may decay into one of the open channels and have a marked influence on the scattering observables (e. g. see [36]). The associated scattering length for the multichannel problem becomes a complex quantity:  $a = \alpha - i\beta$ , and the two parameters are then related to the full elastic S-matrix as  $k$  tends to zero [38]

$$\alpha = -\lim_{k \rightarrow 0} \frac{Im(S^{el})}{2k} \quad \beta = \lim_{k \rightarrow 0} \frac{1 - Re(S^{el})}{2k} \quad (5.19)$$

when  $\alpha > 0$  the associated pole of the S-matrix yields an energy location for which the real part of the latter is the binding energy of the least bound resonance, while for  $\alpha < 0$  the energy is that of the virtual state of least energy:  $\alpha$  will therefore show divergent behaviour when moving from one situation to the other [36,37] Analogously, the corresponding time delay [39]  $\Delta t$  can be related to the above quantities in the limit of vanishing energy [38]

$$\Delta t \sim -\frac{2\mu}{k} \frac{\alpha}{1 - 4k\beta} \quad (5.20)$$

hence, we can see that, in the elastic scattering channels of the multichannel process, the time delay will be positive for a virtual state and negative for a resonant state.

Since we just established that virtual states of a reactive system will be seen from the presence of divergent behaviour of  $\alpha$ , we have carried out just such type

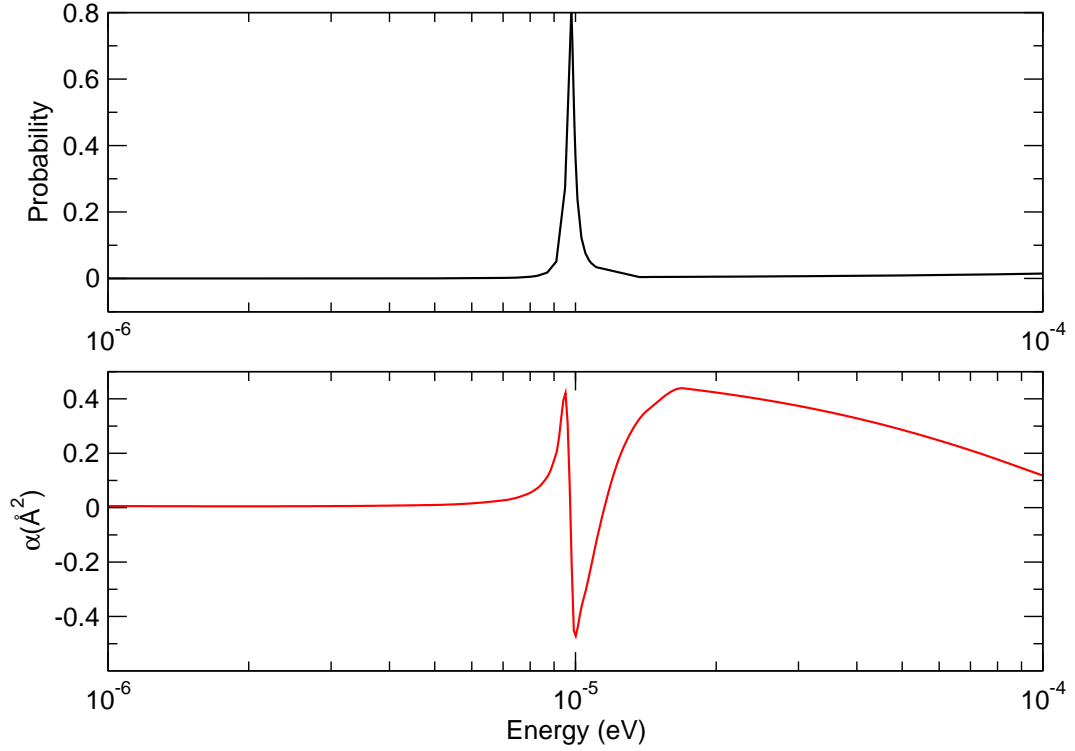


Figure 5.26 Upper panel: reactive probabilities at vanishing kinetic energy for reaction 5.17. Lower panel: computed behaviour of the associated real part of the scattering length.

of calculation for the analysis of the strong peak seen in figure 5.25. In this case we have scanned the range of vanishing energy from  $10^{-4}$  to  $10^{-6}$  eV, ensuring all along that the scattering process is dominated by s-wave contribution [37]. The results for the corresponding behaviour of the real part of the scattering length are given in the panels of figure 5.26. They indicate that indeed such a quantity diverges exactly at the energy where the strong feature of the reactive cross section occurs. Furthermore, we see that the  $\alpha(k)$  approaches the low-energy behaviour as a positive quantity of increasing size, thus indicating there the existence of a resonant state of the complex. The scattering length then changes abruptly to minus infinity as the earlier resonance turns into a virtual state and the  $\alpha(k)$  decreases to large negative values. As the energy keeps decreasing we see that the scattering length changes sign passing through a zero energy resonance, just when the reaction cross section gives rise to a marked maximum in its size [36,37]. In other words, we see that the indicator of the occurrence of a zero-energy resonance followed by a virtual state of the complex is then the changing size of the reaction cross section for the destruction process associated to the  $\text{HeH}^+$  ionic partner. Since this feature is very prominent and occurs at energies amenable, at least in principle, to experimental observations in traps, one could hope that some future observational confirmation could be found.

Another interesting set of structures in the computed reactive cross sections at ultralow energies is given by the sequence of close-by maxima reported by figure 5.25.

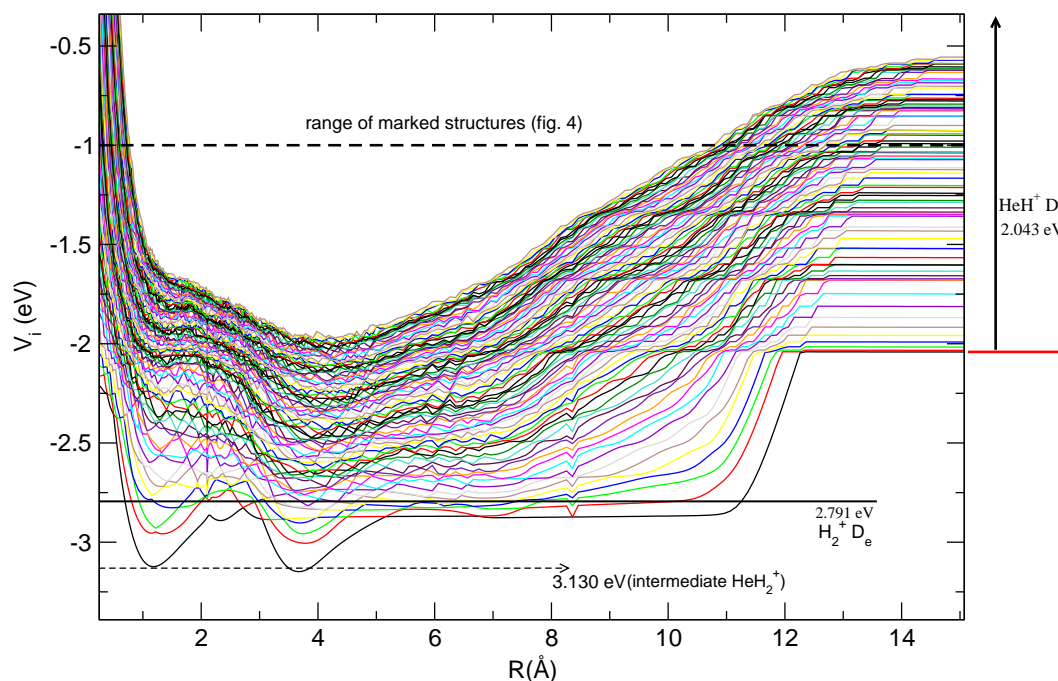


Figure 5.27 Computed, radial adiabatic potential curves  $V_i(R)$ , obtained from the RPES employed for the present reaction.

We see there, in fact, the occurrence of a series of marked peaks of varied intensity that will merge into the unstructured maximum of figure 5.24 once the correct total cross section is considered. However, we know that the  $J=0$  probabilities already give us very useful details on the effect of interchannel couplings due to the occurrence of resonant states during the reactive evolution into the products.

In particular, we wish to argue that the visible peak structure is the consequence of Feshbach-type, closed-channel interaction that makes accessible, during the scattering process, the transition-state region of the triatomic complex, thereby giving occurrence to local bound states created by the marked well of 350 meV.

To qualitatively support this possibility, we report in figure 5.27 the sequence of adiabatic potential curves ( $V_i(R)$ ), after integration over the molecular ( $\text{HeH}^+$ ) internal degrees of freedom ( $r, \theta$ , and  $\phi$ ), that are given by the full RPES along the reaction coordinate.

The energy posts reported in that figure tell us that: (i) the binding energy of the reagent ion is about 2.043 eV, thus well above the energies of interaction; (ii) the product formation ( $\text{H}_2^+$ ) is more than 0.7 eV below, thereby providing a marked energy gain within the reaction region, and (iii) the transition intermediate is below the products' asymptote by about 350 meV and therefore provides, at vanishing kinetic energy, the additional energy needed to locally couple the very numerous pseudo-bound states of the many curves shown in the figure that are instead asymptotically closed.

In other words, we see that each of the many adiabatic curves shown in the reaction region supports a number of bound states which can become locally open

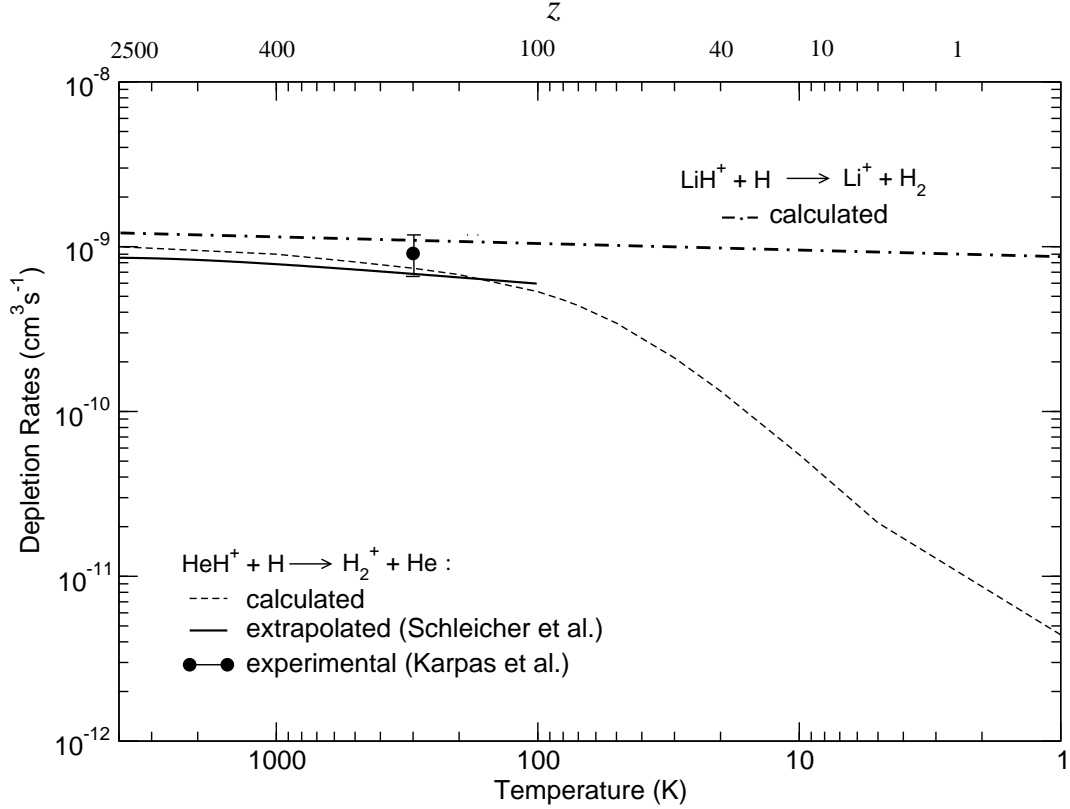


Figure 5.28 Computed rate coefficient for the reaction 5.17 as a function of  $T$

at some, very low value of relative kinetic energy of the reactive partners. For some of this extremely dense structure of adiabatic potentials these corresponding bound states thus become accessible during the reaction and therefore give rise to the maxima on the reactive cross sections shown by figure 5.25. As the collision energy increases, however, many more  $J$  values become important and the greatest majority of such local bound states are no more accessible while the number of possible open channel resonances increases, thus giving rise to the broad maximum in the reaction cross sections shown in figure 5.24.

Such features were observed earlier on in several numerical studies of low-energy resonances for the  $\text{F} + \text{H}_2$  system [40–42] and largely confirm, for a neutral system with weaker interaction forces, the present findings.

### 5.2.3 The depletion rates

The new computed rate coefficients are reported in table 5.6 and fitted with the formula

$$\alpha(T) = 4.3489 \times 10^{-10} T^{0.110373} e^{(-31.5396/T)}, \quad (5.21)$$

which is valid for  $T \leq 1000$  K. The experimental value obtained by Karpas et al [43] is also reported for comparison in the same Table. It is again very reassuring to

## Results for the chemical routes

---

T(K)	$\alpha$ ( $\text{cm}^3\text{s}^{-1}$ )	
1	$4.41 \times 10^{-12}$	
5	$2.11 \times 10^{-11}$	
10	$5.47 \times 10^{-11}$	
20	$1.33 \times 10^{-10}$	
30	$2.11 \times 10^{-10}$	
50	$3.43 \times 10^{-10}$	
70	$4.39 \times 10^{-10}$	
80	$4.76 \times 10^{-10}$	
100	$5.33 \times 10^{-10}$	
200	$6.76 \times 10^{-10}$	
300	$7.39 \times 10^{-10}$	$9.10 \pm 2.5 \times 10^{-10}$ (*)
500	$8.08 \times 10^{-10}$	
800	$8.70 \times 10^{-10}$	

(\*) experimental (Karpas et al [43])

Table 5.6 Computed production/destruction rates of  $\text{HeH}^+$  as function of redshift. Solid and dashed curves represent production and destruction processes, respectively.

see that the only existing experimental datum at 300 K is indeed very close to our computational value at the same temperature. We note, however, that the results of figure 5.28 are very different from those for  $\text{LiH}^+$  (sec. 5.1.3) across the same range of energies. These differences are related to the different microscopic mechanisms of the reaction pathways between the two systems. Qualitatively, the two systems, although both undergoing no barrier, exothermic reactions, have very different exothermicity values that affect the product separations at low energy.



# Bibliography

- [1] Lepp, S. & Shull, J.M., ApJ, **270**, 578, 1983
- [2] Stancil P. C., Lepp S. & Dalgarno A., ApJ, **458**, 401, 1996
- [3] Galli D., Palla F., A&A, **335**, 403, 1998
- [4] Wagoner R. V., Fowler W. A. & Hoyle F., ApJ, **148**, 3, 1967
- [5] Peebles P. J. E., Principles of Physical Cosmology, Princeton University Press, Princeton, 1993
- [6] Cyburt R. M., Fields B. D. & Olive K. A., J. Cosmol. Astropart. Phys., **11**, 12, 2008
- [7] Dubrovich V. K., Astron. Lett., **19**, 53, 1993
- [8] Maoli R., Melchiorri F., and Tosti D., ApJ, **425**, 372, 1994
- [9] Bougleux E. & Galli D., MNRAS., **288**, 638, 1997
- [10] Schleicher, D. R. G., Galli, D., Palla, F., Camenzind, M., Klessen, R. S., Bartelmann, M., & Glover, S. C. O. A&A, **490**, 521, 2008
- [11] Vonlanthen, P., Rauscher, T., Winteler, C., Puy, D., Signore, M., Dubrovich, V., A&A, **503**, 47, 2009
- [12] Dunne L. J., Murrell J. N. & Jemmer P., Chem. Phys. Lett., **336**, 1, 2001
- [13] Defazio P., Petrongolo C., Gamallo P. & González M., J. Chem. Phys., **122**, 214303, 2005
- [14] Wernli M., Caruso D., Bodo E. & Gianturco F. A., J. Phys. Chem. A., **113**, 1121, 2009
- [15] Skouteris D., Castillo J. F. and Manolopoulos D. E., Comp. Phys. Comm., **133**, 128, 2000
- [16] Padmanaban R. and Mahapatra S., J. Chem. Phys., **121**, 7618, 2004
- [17] Puy D., Alciau G., Le Bourlot J., Léorat J. and Pineau des Forêts G., Astron. Astrophys., **267**, 337, 1993
- [18] Neuhauser D., Baer M., Kouri D. J., J. Chem. Phys., **93**, 2499, 1990
- [19] Last I., Neuhauser D., & Baer M., J. Chem. Phys., **96**, 2017, 1992
- [20] Stechel E. B., Walker R. B., & Light J. C., J. Chem. Phys., **69**, 3518, 1978
- [21] Li X., Wang M., Pino I., Yang C., & Ma L., Phys. Chem. Chem. Phys., **11**, 10438, 2009
- [22] Lepp S., Stancil P. C. & Dalgarno A., J. Phys. B:At. Mol. Opt. Phys., **35**, R57-R80, 2002

## BIBLIOGRAPHY

---

- [23] Pino I., Martinazzo R., & Tantardini G., *Phys. Chem. Chem. Phys.*, **10**, 5545, 2008
- [24] Bulut N., Castillo J. F., Aoiz F. J., & Banares L., *Phys. Chem. Chem. Phys.*, **10**, 821, 2008
- [25] Levine R. D., & Bernstein R. B., *Molecular Reaction Dynamics and Chemical Reactivity*, Oxford Univ. Press, 1987
- [26] Bodo E., Gianturco F. A., & Martinazzo R., *Phys. Rep.*, **384**, 85, 2003
- [27] M. Baer, C. Y. Ng, D. Neuhauser, & Y. Oreg, *J. Chem. Soc. Faraday Trans.*, **86**, 1721, 1990
- [28] Roberge W., and Dalgarno A., *ApJ*, **255**, 489, 1982
- [29] Liu X.-W. et al., *MNRAS*, **290**, L71, 1997
- [30] Harris G. J., Lynas-Gray A. E., Miller S., and Tennyson J., *ApJ*, **617**, L143, 2004
- [31] Engel E. A., Doss N., Harris G. J., and Tennyson J., 2005, *MNRAS*, 357, 471
- [32] Saio H., and Jeffery C. S., 2000, *MNRAS*, 313, 671
- [33] Rutherford J. A., and Vroom D. A., 1973, *J. Chem. Phys.*, 58, 4076
- [34] Linder F., Janev R. K., and Botero J., 1995, *Atomic and Molecular Processes in Fusion Edge Plasmas*, ed. R. K. Janev (NY: Plenum Press), 397
- [35] E. Bodo, F. A. Gianturco, N. Balakrishnan, A. Dalgarno, *J. Phys. B*, **37**, 3641, 2004
- [36] D. Field and L. B. Masden, *J. Chem. Phys.* **118**, 1679, 2003
- [37] C. J. Joachain, *Quantum collision theory*, North Holland Publishing Company, 1975
- [38] N. Balakrishnan, V. Kharchenko, R. C. Forrey, A. Dalgarno, *Chem. Phys. Lett.* **280**, 5, 1997
- [39] F. T. Smith, *Phys. Rev.* **108**, 349, 1960
- [40] E. Rosenman, A. Persky, M. Baer, *Chem. Phys. Lett.* **258**, 639, 1996
- [41] D. Manolopoulos, *J. Chem. Soc. Faraday Trans.* **93**, 673, 1997
- [42] T. Takayanagi, Y. Kurosaki, *Chem. Phys. Lett.* **286**, 35, 1998
- [43] Karpas Z., Anicich V., and Huntress, Jr. W. T., *J. Chem. Phys.*, **70**, 2877, 1979

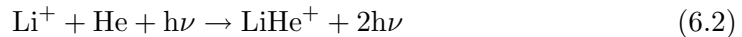
*Still the rain kept pouring,  
Falling on my ears.  
And I wonder, Still I wonder  
Who'll stop the rain.*



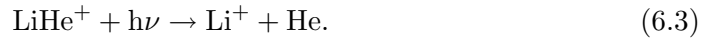
## Photon induced dynamics: the case of $\text{LiHe}^+$

### 6.1 The formation of $\text{LiHe}^+$

It is crucial to explore as much as possible the properties of the species which could have been involved in the cooling processes of the first stars formation stage. In previous sections we discussed about the possible role of lithium-containing molecules ( $\text{LiH}$  and  $\text{LiH}^+$ ) and  $\text{HeH}^+$ , all composed of the most abundant atomic species thought to be present during the post-recombination era. On the other hand, another important molecule, i.e.  $\text{LiHe}^+$ , has not yet received the same attention in earlier works although its possible presence has been suggested in earlier papers [1,2]. It is interesting, at this stage, to start with a comparison of the most revealing features of the three polar cations which could play the role of molecular coolants in that early universe environment, in order to place the  $\text{LiHe}^+$  component within a broader perspective. As we can see from table 6.1, these three species show marked differences although similar molecular properties exist among them: the present ion is the one with the smallest  $D_e$  value and the smallest harmonic frequency. Its dipole moment, however, is still substantial and, as we shall see, leading to efficient recombination mechanisms. Although it would be easily dissociated by collisions even at small collision frequencies, we think that it would still be interesting to acquire reliable modeling data from calculations and thus study the evolution of the  $\text{LiHe}^+$  ion to further extend the network of reactions which model the evolution of early universe composition and which have been studied before for  $\text{LiH}^+$  and  $\text{HeH}^+$ . In the present chapter, we intend to accurately get first the main photochemical reactions involving  $\text{LiHe}^+$ , like those involving spontaneous and stimulated photon emissions:



and also the photodissociation induced by Black-body Radiation Field (BRF) leading to photon absorption:



	$\text{LiH}^+(^2\Sigma^+)$ (a)	$\text{HeH}^+(^1\Sigma^+)$ (b)	$\text{LiHe}^+(^1\Sigma^+)$ (c)
$D_e$ ( $\text{cm}^{-1}$ )	1132.4	16448.4	648.2 (649.2 <sup>d</sup> )
$R_e$ ( $\text{\AA}$ )	2.18	0.77	1.90 (1.896 $\pm$ 0.002 <sup>d</sup> )
$\omega_e$ ( $\text{cm}^{-1}$ )	422.1	3228.0	260.0
# bound states <sup>e</sup>	6(64)	11(158)	7(73)
dipole moment (Debye)	$\sim$ 0.60	$\sim$ 1.3	$\sim$ 0.40

(a) data from Dalgarno et al [3]

(b) data from Bishop and Cheung [4]

(c) present results

(d) data from Soldán et al [5]

(e) the data in brackets refer to the total number of rovibrational states

Table 6.1 Spectroscopic parameters for the three ionic molecules thought to be present in the early universe stage as among the most likely components of the latter. The dipole moments are evaluated with the origin over the atoms which carry the charge at the dissociation limit.

### 6.1.1 The ground state intermolecular potential

In order to carry out the calculations of radiative association cross sections the potential energy curve (PEC) of the  $X^1\Sigma^+$  ground electronic state of the  $\text{LiHe}^+$  together with the electric dipole moment function are needed. We have thus calculated the PEC by employing the CCSD(T) expansion with cc-pV5Z and aug-cc-pV5Z basis sets for  $\text{Li}^+$  and He respectively. All energy calculations were performed employing MOLPRO [6] and including the full counterpoise method [7] for the basis-set superposition error (BSSE) correction. The rovibrational bound states of the molecule have been generated using Le Roy’s LEVEL 8.0 program [8]. The dipole moment function has been evaluated in the center of mass of the molecule by using the CCSD ansatz and the same gaussian basis set used for the PEC calculation. The dipole moment is reported in table 6.2 as a function of the internuclear distance between partner atoms. Some of our computed spectroscopic data for this molecule are reported in table 6.1: as we can see from that table, our data are in very good agreement with the previous calculations of Soldán et al [5].

### 6.1.2 Radiative association computational results

The total cross sections for stimulated and spontaneous radiative association of  $\text{Li}^+$  and He (eq.s 6.1 and 6.2) are given in figure 6.1 as a function of the collision energy and for black-body temperatures ranging from 0 to 5000 K. The cross sections for  $T_b = 0$  K correspond to the spontaneous radiative association only, as derived from the equation 2.7. The data show, as expected, that the presence of the BRF produces an enhancement in the association cross sections; as the temperature of the latter increases, the contribution of the stimulated process causes changes of

R (Å)	Dipole moment (a.u.)
1.350	-0.81581402
1.400	-0.84860730
1.450	-0.88231294
1.500	-0.91682463
1.550	-0.95204202
1.600	-0.98786861
1.650	-1.02421250
1.700	-1.06098692
1.750	-1.09811075
1.800	-1.13550924
1.850	-1.17311483
1.900	-1.21086778
1.950	-1.24871623
2.000	-1.28661589
2.500	-1.66273529
3.000	-2.02866481
3.500	-2.38666484
4.000	-2.74006443
4.500	-3.09090158
5.000	-3.44020292
5.500	-3.78851813
6.000	-4.13617127
6.500	-4.48336094
7.000	-4.83021547
8.000	-5.52324314
10.000	-6.90775973

Table 6.2 Computed dipole moment  $\mu(R)$  as a function of internuclear distances. The origin of  $\mu(R)$  is taken at the molecular center of mass.

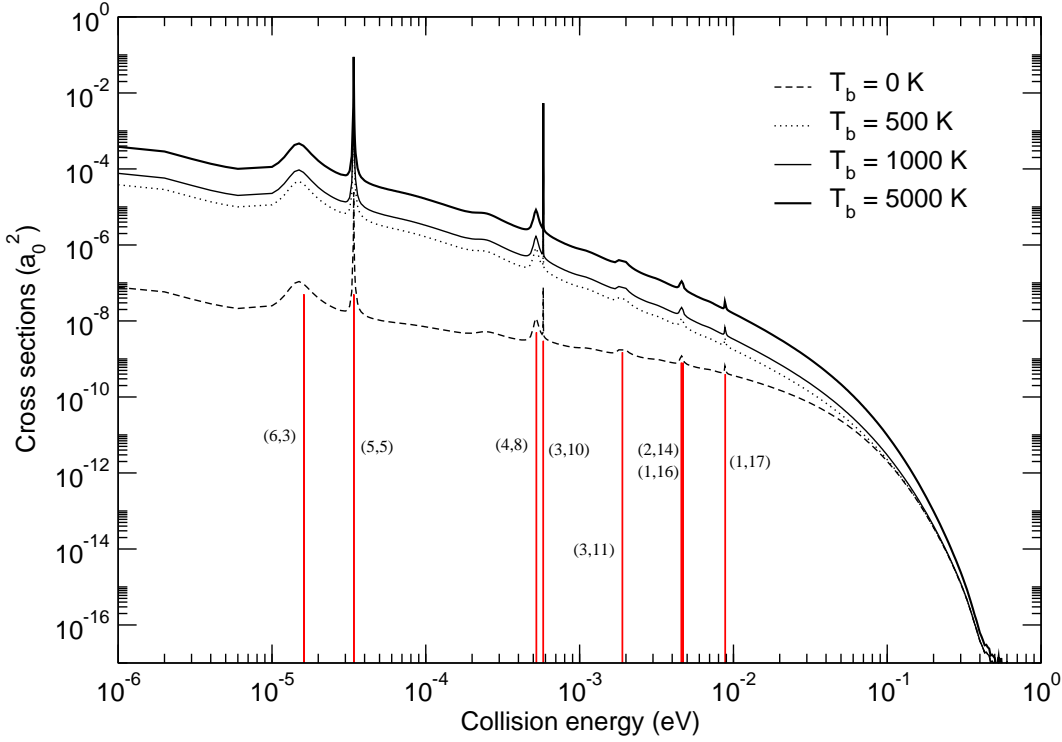


Figure 6.1 Computed cross sections for stimulated plus spontaneous (at  $T_b = 0$ ) radiative association of  $\text{Li}^+$  and He for various black-body radiation temperatures  $T_b$ . For  $T_b > 0$  only total cross sections are shown. See text for further details.

3-to-4 orders of magnitude in the total photoassociation cross sections at the lower collision energies. One further sees that the field contribution becomes negligible for collision energies corresponding to gas temperatures ( $T_g$ ) greater than 11,000 K.

The pronounced structures that appear in figure 6.1 are the result of shape resonances which occur through the formation of quasibound roto-vibrational states of the molecule being created. Each contribution has been labelled more specifically in the same figure. The relative quantities which characterize the resonances are reported there: they indicate the specific angular momentum value ( $J'$ ) causing potential trapping and the metastable bound state ( $n'$ ). Further details on the resonance features are shown collectively by table 6.3.

The final rate coefficients needed for modeling the chemical networks are in turn obtained as

$$\alpha(T_g) = \frac{(8\kappa/\pi\mu)^{1/2}}{(\kappa T_g)^2} \int_0^\infty \sigma(E) \exp(-E/\kappa T_g) E dE \quad (6.4)$$

and are displayed in figure 6.2 as a function of  $T_g$  and  $T_b$ . We see again there that the stimulated emission increases the values of the computed rate coefficients by more than one order of magnitude when the gas temperatures vary from 1000 to 5000 K. The actual numerical values are listed in table 6.4.

$n'$	$J'$	$E_r$ (meV)	$\Gamma$ (meV)	$\tau$ (s)
6	3	0.01613	$9.90741 \times 10^{-03}$	$6.6512 \times 10^{-11}$
5	5	0.03404	$1.10578 \times 10^{-04}$	$5.9593 \times 10^{-09}$
4	8	0.52391	$4.64662 \times 10^{-02}$	$1.4181 \times 10^{-11}$
3	10	0.58106	$3.59056 \times 10^{-05}$	$1.8352 \times 10^{-08}$
3	11	1.89776	$1.93660 \times 10^{-01}$	$3.4027 \times 10^{-12}$
2	14	4.59252	$2.41324 \times 10^{-01}$	$2.7306 \times 10^{-12}$
1	16	4.71345	$1.47349 \times 10^{-04}$	$4.4722 \times 10^{-09}$
1	17	8.85744	$1.11747 \times 10^{-01}$	$5.8969 \times 10^{-12}$

Table 6.3 Computed rovibrational resonances for the ground electronic state of the  $\text{LiHe}^+$  ion

$T_g/T_b$ (K)	0	300	500	1000	3000	5000
10	1.78	78.3	120.0	239.5	722.2	1195.3
20	1.56	42.5	66.5	132.5	398.2	658.2
30	1.43	28.9	45.6	90.6	271.6	448.9
45	1.33	21.8	27.0	53.8	160.3	264.3
80	0.99	9.02	14.6	29.0	86.0	141.9
90	0.95	8.05	13.0	25.8	76.5	126.2
100	0.90	7.26	11.8	23.2	68.7	113.4
200	0.69	3.28	5.24	10.2	30.0	49.6
300	0.43	1.99	3.14	6.08	17.8	29.3
400	0.34	1.37	2.15	4.10	12.1	19.5
500	0.27	1.02	1.56	3.00	8.70	14.1
700	0.18	0.61	0.94	1.77	5.12	8.46
800	0.10	0.50	0.77	1.45	4.20	6.94

Table 6.4 Computed total, spontaneous plus stimulated, radiative association rate coefficients  $\alpha(10^{-21} \text{ cm}^3\text{s}^{-1})$  for  $\text{Li}^+ + \text{He}$  as a function of gas temperature  $T_g$  (column values) and black-body radiation temperature  $T_b$  (row values). All temperatures in Kelvins. The interaction potentials is that of the molecular ground electronic state.

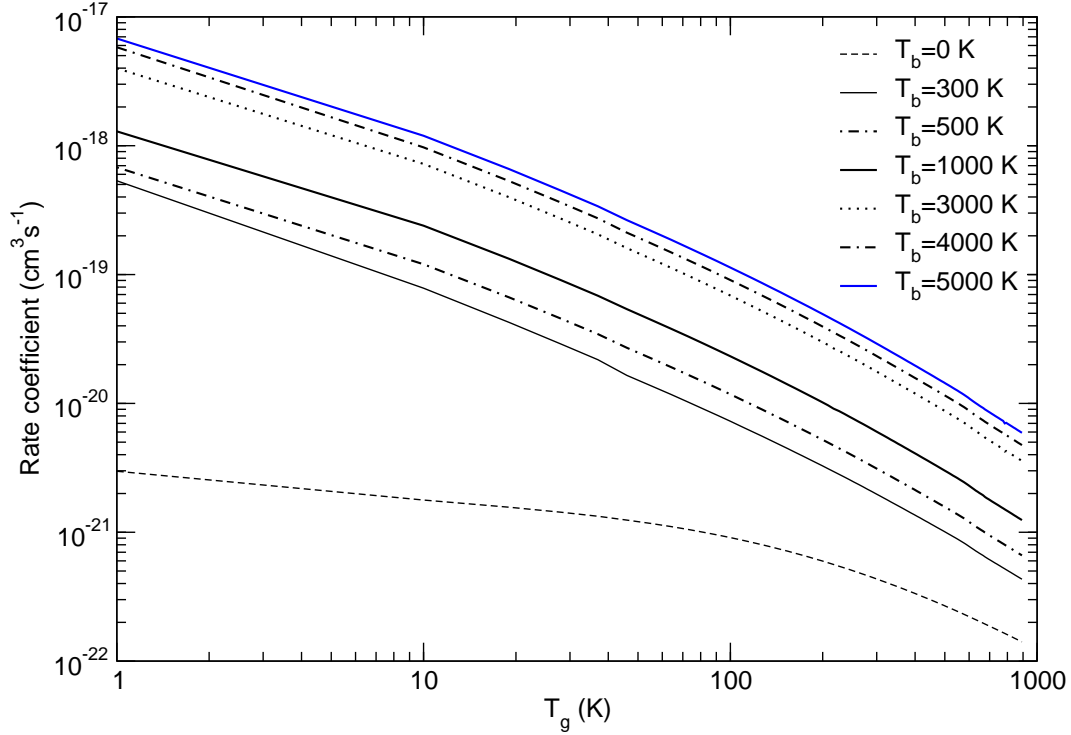


Figure 6.2 Rate coefficients for stimulated plus spontaneous ( $T_b = 0$  K) radiative association of  $\text{Li}^+$  and He in the ground electronic state of the molecule. The data are shown here for various black-body radiation temperatures ( $T_b$ ) and as function of the gas temperature  $T_g$ . Only total rates are shown for  $T_b > 0$ .

### 6.1.3 Photodissociation computational results

The calculated, Boltzmann-averaged absorption cross sections for  $T=600$  K, obtained from equation 2.9, are shown by figure 6.3 as function of photon frequency. This cross section consists of contributions from various bound states ( $n', J'$ ) undergoing transitions into the continuum. The maximum energy amount needed to dissociate the (0,0) species, i.e. the molecule in its lowest bound state, occurs at  $\sim 515.55 \text{ cm}^{-1}$  since we involve here only the electronic ground state of  $\text{LiHe}^+$  molecule as already mentioned. The first excited electronic state for  $\text{LiHe}^+$  is, in fact, at  $\sim 19 \text{ eV}$  above the ground state, hence it would require a very high temperature for making the process likely to occur, as already discussed by [1]. The threshold of minimum energy needed for dissociating the  $(n_{max}, j_{max})$  state is instead  $\sim 0.69 \times 10^{-2} \text{ cm}^{-1}$ .

The computed destruction rates, obtained from equation 2.12 as a function of the black-body radiation temperature and for each of the initial vibrational states of the target molecule, are shown in figure 6.4. We clearly see there that the effect of changing the initial vibrational state on the photodissociation rate coefficients is not very marked: they only vary by about one order of magnitude when going from  $n'=0$  to  $n'=6$ . The total, cumulative photodissociation rates are also reported in figure 5; it is evident from their values that the process of photodissociating the



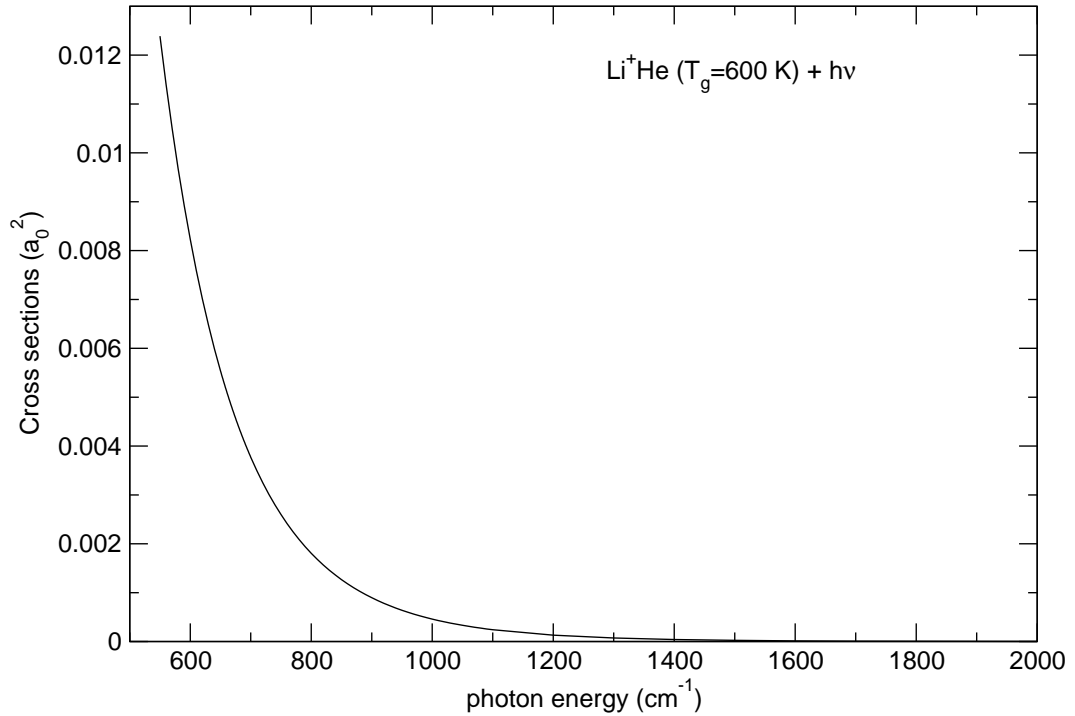


Figure 6.3 Computed  $\text{LiHe}^+$  photodissociation cross sections, from the molecular ground electronic state, as function of photon energy and for a selected temperature of 600 K. See text for further details.

molecule yields rather large cross sections, indicating that it could play an important role in the disappearance of  $\text{LiHe}^+$  after its possible formation during early universe epoch, considering that their magnitude turns out to be comparable with that of other competing processes involving  $\text{LiH}$  and  $\text{LiH}^+$ .

## 6.2 Implications for the chemical network

In this work we have analyzed in some detail the photochemistry of the  $\text{LiHe}^+$  molecule using accurate quantum methods. First, the spontaneous and stimulated radiative association cross sections have been calculated and analyzed: our results show rate coefficients of the order of  $10^{-21}$ - $10^{-20} \text{ cm}^3\text{s}^{-1}$ . Additionally, the total photodissociation rates have been calculated for the direct process involving the  $X^1\Sigma^+$  electronic ground state of the  $\text{LiHe}^+$  ion. In order to further compare the three processes, for studying the evolution of this ion during the early universe, we report in figure 6.5 the computed production and destruction rates (in  $\text{s}^{-1}$ ) as a function of redshift,  $z$ , values.

Our data show that the radiative association processes (spontaneous and stimulated) dominate over the whole range of redshifts reported and are in competition with the destruction processes by photodissociation up to  $z \sim 40$  values, rapidly losing importance as  $z$  decreases. Furthermore, the present calculations provide

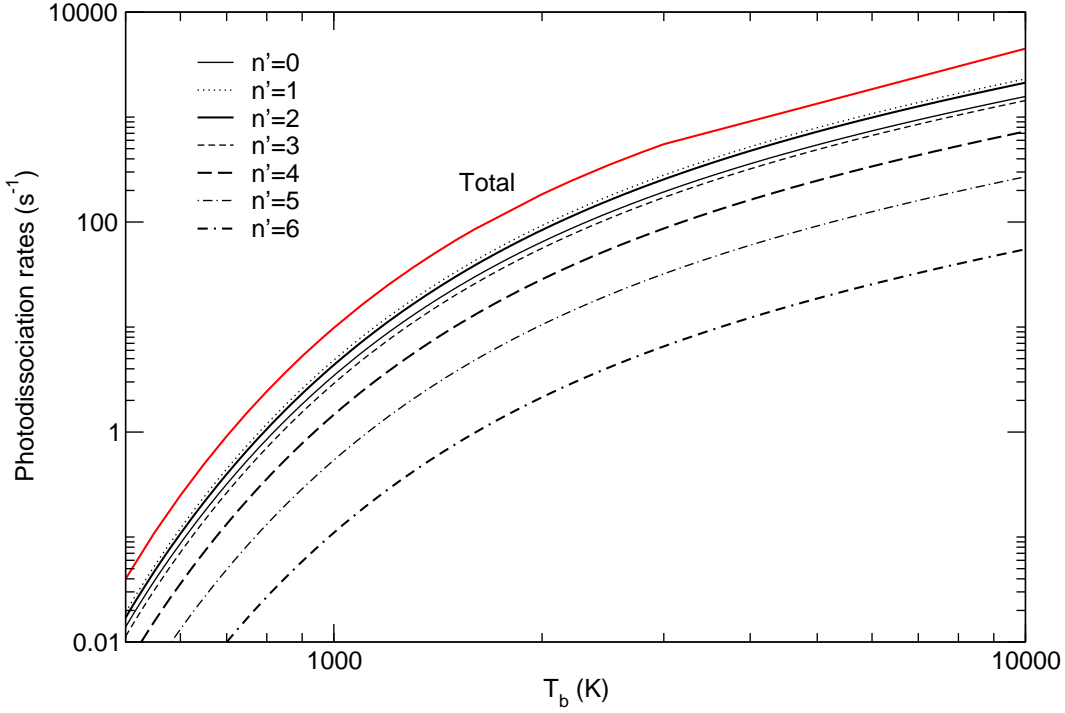


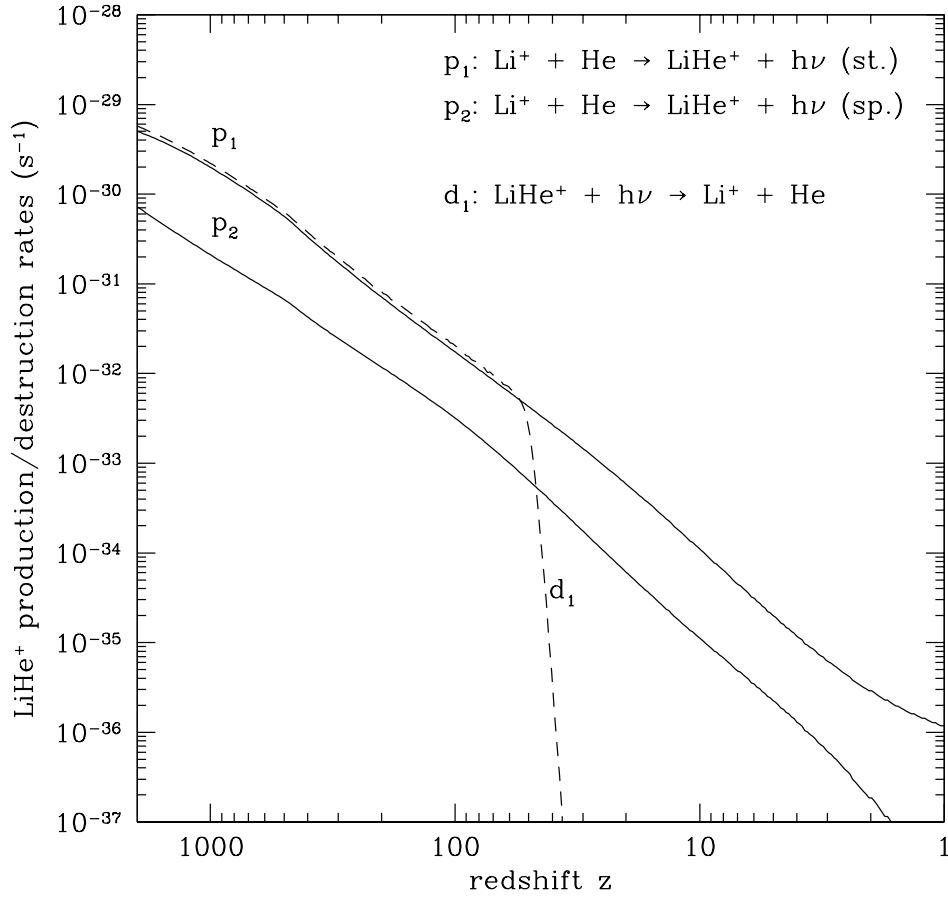
Figure 6.4 Computed  $\text{LiHe}^+$  photodissociation rate coefficients as function of black-body radiation temperature,  $T_b$ . The individual contribution from each of the possible initial vibrational levels ( $n'=0$  to 6) are shown, together with the value of the cumulative rate (Total).

compelling evidence for the fact that the contribution of stimulated association is a fundamental channel for the formation of the ion, as already discussed in previous work by [9].

To examine the rates of fig. 6.5 in a broader context, it is then important to further include all the other processes involving the  $\text{LiHe}^+$  ion in order to complete the network of reactions and thus formulate a more reliable chemical model which would yield the final abundances of  $\text{LiHe}^+$  comparing them with those for other important ions like  $\text{LiH}^+$  and  $\text{HeH}^+$ . We see here that the large photodissociation rates are likely to affect the contributions to formation from radiative association at low redshift. On the other hand, the story of the evolution for the specific ion would not be completed without considering two further pathways which could contribute to its final presence in the early universe environment: (i) the chemical path involving the ubiquitous hydrogen atoms:



which leads to the destruction of this molecule and which is, as indicated by the data of table 6.1, an exothermic reaction occurring without barrier from very low temperatures ([10]); ii) the corresponding inverse reaction involving  $\text{LiH}^+$  which

Figure 6.5 Production/destruction rates for  $\text{LiHe}^+$ 

could also contribute to the formation of our title system



but it is, however, endothermic for  $\text{LiH}^+$  in its ground vibrational level [11] and it would require its excitation to at least the  $n = 1$  level in order to acquire exothermicity. Both these processes have been largely discussed in the previous section.

Another process which could lead to destruction of the present molecule is related to the electron-driven path that causes dissociative recombination



The computational modeling of the above destruction path has not been attempted thus far and is currently being carried out in our group [12]. The likely mechanism

presiding over the efficiency of reaction 6.7 essentially hinges of the size and strength of the couplings, induced by the impinging electron at low energies, between the ion vibrational bound state (mainly  $n = 0$ ) and the manifold of vibrational levels of the temporary neutral molecule formed into one member of the extensive series of Rydberg lithium states existing for  $\text{Li}^*\text{He}$ . It is therefore hard to predict the efficiency of 6.7 without actual evaluation of those terms and their inclusion in the calculation of the final rates.

It is clear, however, that the present calculations of the photon-induced processes which can drive formation/destruction of  $\text{LiHe}^+$  ions in the early universe conditions already indicate that formation processes are dominant at low redshifts and therefore this molecular ion needs to be considered in the fuller chemical network of early molecule formation. Whether or not it will be playing a role in relation to the other two ions of table 6.1, clearly depends on the inclusion of the additional paths outlined in this Section. This specific aspect will indeed be the object of another work that obviously will rely on the accurate calculations of the photon-induced processes which we have described in detail in the present section.

# Bibliography

- [1] Kirby K. P., Phys. Scripta, **T59**, 59, 1995
- [2] Dalgarno A., Int. J. Mass. Spectr., **149**, 429, 1995
- [3] Dalgarno A., Kirby K. and Stancil P. C., ApJ, **458**, 397, 1996
- [4] Bishop D. M., and Cheung L. M., J. Mol. Spectrosc., **75**, 462, 1979
- [5] Soldán P., Lee E. P. F., Lozeille J., Murrell J. N., Wright T. G., Chem. Phys. Lett., **343**, 429, 2001
- [6] MOLPRO is a package of ab initio programs written by H.-J. Werner, P. J. Knowles, F. R. Manby, M. Schtz et al. with the CCSD treatment being described in: Hampel C., Peterson K, Werner H. J., Chem. Phys. Lett., **190**, 1, 1992
- [7] Boys S. F., and Bernardi F., Mol. Phys., **19**, 553, 1970
- [8] Le Roy R. J., LEVEL 8.0,- A computer program for solving the radial Schrödinger equation for bound and quasibound levels, University of Waterloo Chemical Physics Research Program Report CP-555R, 2000
- [9] Stancil P. C., and Dalgarno A., ApJ, **479**, 543, 1997
- [10] Scifoni E., Bodo E., Gianturco F. A., J. Chem. Phys., **122**, 224312, 2005
- [11] Wernli M., Scifoni E., Bodo E., and Gianturco F. A., Int. J. Mass Spectr., **280**, 57, 2009
- [12] Čurík R., Bovino S., Tacconi M., and Gianturco F. A., 2011, in preparation



## The chemical network

## 7.1 The evolutionary model

The evolution of the pregalactic gas is considered in the framework of a Friedmann cosmological model and the primordial abundances of the main gas components are taken from the standard big bang nucleosynthesis results [1]. The numerical values of the cosmological parameters used in the calculation are obtained from WMAP5 data [2] and are listed in Table 7.1.

In order to calculate the abundances of molecules, a set of differential coupled chemical rate equations of the form:

$$\frac{dn_i}{dt} = \alpha_{\text{form}} n_j n_k - \alpha_{\text{dest}} n_i + \dots \quad (7.1)$$

has been solved. In eq. 7.1,  $\alpha_{\text{form}}$  and  $\alpha_{\text{dest}}$  are the formation and destruction reaction rates of the considered molecule, and  $n_i$  is the number density of the reactant species  $i$ . The evolution of the gas temperature  $T_g$  is governed by the equation (see e.g. [3]):

$$\frac{dT_g}{dt} = -2T_g \frac{\dot{R}}{R} + \frac{2}{3kn} [(\Gamma - \Lambda)_{\text{Compton}} + (\Gamma - \Lambda)_{\text{mol}}], \quad (7.2)$$

where the first term represents the adiabatic cooling associated with the expansion of the Universe,  $R$  being the scale factor. The other two terms represent, respectively, the net transfer of energy from the CBR to the gas (per unit time and unit volume) via Compton scattering of CBR photons and electrons,

$$(\Gamma - \Lambda)_{\text{Compton}} = n_e \frac{4k\sigma_T a T_r^4 (T_r - T_g)}{m_e c}, \quad (7.3)$$

and via excitation and de-excitation of molecular transition

$$(\Gamma - \Lambda)_{\text{mol}} = \sum_k n_k \sum_{i>j} (x_i C_{ij} - x_j C_{ji}) h\nu_{ij}, \quad (7.4)$$

where  $C_{ij}$  and  $C_{ji}$  are the collisional excitation and de-excitation coefficients and  $x_i$  are the fractional level populations: for more details of this model see [3, 4]. The radiation temperature is  $T_r(z) = T_0(1+z)$ , where  $T_0$  is the present-day CBR temperature. The chemical/thermal network is then completed by the rate equation for the redshift

$$\frac{dt}{dz} = -\frac{1}{(1+z)H(z)}, \quad (7.5)$$

## The chemical network

Parameter	Numerical value
$H_0$	$70.5 \text{ km s}^{-1} \text{ Mpc}^{-1}$
$T_0$	$2.725 \text{ K}$
$z_{\text{eq}}$	$3141$
$\Omega_{\text{dm}}$	$0.228$
$\Omega_{\text{b}}$	$0.0456$
$\Omega_{\text{m}}$	$\Omega_{\text{dm}} + \Omega_{\text{b}}$
$\Omega_{\text{r}}$	$\Omega_{\text{m}}/(1 + z_{\text{eq}})$
$\Omega_{\Lambda}$	$0.726$
$\Omega_{\text{K}}$	$1 - \Omega_{\text{r}} - \Omega_{\text{m}} - \Omega_{\Lambda}$
$f_{\text{H}}$	$0.924$
$f_{\text{He}}$	$0.076$
$f_{\text{D}}$	$2.38 \times 10^{-5}$
$f_{\text{Li}}$	$4.04 \times 10^{-10}$

Table 7.1 Cosmological model

where

$$H(z) = H_0 \sqrt{\Omega_{\text{r}}(1+z)^4 + \Omega_{\text{m}}(1+z)^3 + \Omega_{\text{K}}(1+z)^2 + \Omega_{\Lambda}}. \quad (7.6)$$

Here,  $H_0$  is the Hubble constant and  $\Omega_{\text{r}}, \Omega_{\text{m}}, \Omega_{\text{K}}, \Omega_{\Lambda}$  are density parameters. The density  $n(z)$  of baryons at redshift  $z$  is

$$n(z) = \Omega_{\text{b}} n_{\text{cr}} (1+z)^3, \quad (7.7)$$

with  $n_{\text{cr}} = 3H_0^2/(8\pi G m_{\text{H}})$  being the critical density. The calculations have been carried out from  $z = 10^4$  down to  $z = 1$  and are discussed in the next sections.

## 7.2 The lithium chemistry

### 7.2.1 LiH chemistry

The various curves shown in Figure 7.1 follow the notation given in Table 7.2 to the most relevant processes: those labelled as  $p_1, \dots, p_4$  (solid lines) refer to the different reactions leading to LiH production, while those labelled  $d_1, \dots, d_4$  (dashed lines) refer to the destruction processes. A look at the figure allows one to make the following comments:

(i) The production by radiative recombination from the  $\text{Li}(^2P)$  state ( $p_1$ ) clearly dominates at high redshifts, while the production by recombination from the  $\text{Li}(^2S)$  state ( $p_2$ ) becomes the dominant route from  $z \simeq 800$  down to  $z \simeq 80$ . Then, the channel of recombination driven by electron attachment ( $p_4$ ) takes over. However, we must note that the latter rate is not known from quantum calculations, but only estimated by [5], together with the estimates of LiH formation from  $\text{H}^-$  [5].

(ii) At the highest redshifts, the destruction channel is dominated by photodissociation ( $d_1$ ), a rate estimated from the detailed balance of process ( $p_2$ ), while at lower  $z$  values ( $z \leq 300$ ) the collisional process of reactive destruction discussed earlier ( $d_2$ ) takes over and dominates the whole destruction channel down to the lowest



Table 7.2 List of considered reactions. Labels in the second column refer to Figures 2 and 3.

	reaction	rate ( $\text{cm}^3 \text{ s}^{-1}$ or $\text{s}^{-1}$ )	notes	reference
<b>Li reactions</b>				
1)	$\text{Li}(^2p) + \text{H} \rightarrow \text{LiH} + h\nu$	$2.0 \times 10^{-16} T_g^{0.18} \exp(-T_g/5100)$	$A^1\Sigma^+ \rightarrow X^1\Sigma^+$ , quantal calc.	(a)
2)	$\text{Li}(^2p) + \text{H} \rightarrow \text{LiH} + h\nu$	$1.9 \times 10^{-14} T_g^{0.34}$	$B^1\Pi \rightarrow X^1\Sigma^+$ , quantal calc.	(a)
3)	$\text{Li} + \text{H} \rightarrow \text{LiH} + h\nu$	$4.0 \times 10^{-20} \times$ $\exp[-T_g/4065 + (T_g/13193)^3]$	quantal calc.	(b),(c),(d)
4)	$\text{Li} + \text{H}^- \rightarrow \text{LiH} + e$	$4.0 \times 10^{-10}$	estimate	(e)
5)	$\text{Li} + \text{H}^+ \rightarrow \text{LiH}^+ + h\nu$	$5.3 \times 10^{-14} T_g^{-0.49}$	quantal calc.	(c),(d)
6)	$\text{Li} + \text{H}^+ \rightarrow \text{Li}^+ + \text{H}$	$2.5 \times 10^{-40} T_g^{5.9} \exp(-T_g/1210)$	quantal calc.	(f)
7)	$\text{Li} + \text{H}^+ \rightarrow \text{Li}^+ + \text{H} + h\nu$	$1.7 \times 10^{-13} T_g^{-0.051} \exp(-T_g/282000)$	quantal calc.	(g)
8)	$\text{Li} + e \rightarrow \text{Li}^- + h\nu$	$6.1 \times 10^{-17} T_g^{0.58} \exp(-T_g/17200)$	det. bal. applied to (27)	(i)
9)	$\text{Li} + \text{H}_2^+ \rightarrow \text{LiH} + \text{H}^+$	$6.3 \times 10^{-10} \exp(-2553/T_g)$	$T_g < 500$ , quantal calc.	(j)
	$\text{Li} + \text{H}_2^+ \rightarrow \text{LiH} + \text{H}^+$	$7.2 \times 10^{-14} T_g^{1.18} \exp(-1470/T_g)$	$T_g > 500$ , quantal calc.	(j)
<b>Li<sup>+</sup> reactions</b>				
10)	$\text{Li}^+ + \text{H} \rightarrow \text{LiH}^+ + h\nu$	$1.4 \times 10^{-20} T_g^{-0.9} \exp(-T_g/7000)$	quantal calc.	(c),(d)
11)	$\text{Li}^+ + e \rightarrow \text{Li} + h\nu$	$1.036 \times 10^{-11} \sqrt{T_g/107.7} \times$ $(1 + \sqrt{T_g/107.7})^{0.6612} \times$ $(1 + \sqrt{T_g/1.177 \times 10^7})^{1.3388} - 1$	quantal calc.	(k)
12)	$\text{Li}^+ + \text{H}^- \rightarrow \text{Li} + \text{H}$	$6.3 \times 10^{-9} T_g^{-1/2} (1 + T_g/14000)$	Landau-Zener approx.	(l)
<b>Li<sup>-</sup> reactions</b>				
13)	$\text{Li}^- + \text{H} \rightarrow \text{LiH} + e$	$4.0 \times 10^{-10}$	estimate	(e)
14)	$\text{Li}^- + \text{H}^+ \rightarrow \text{Li} + \text{H}$	$2.3 \times 10^{-6} T_g^{-1/2}$	Landau-Zener approx.	(l)
<b>LiH reactions</b>				
15)	$\text{LiH} + \text{H} \rightarrow \text{Li} + \text{H}_2$	$2.0 \times 10^{-12} T_g \exp(-T_g/1200)$	quantal calc.	(m)
16)	$\text{LiH} + \text{H}^+ \rightarrow \text{Li} + \text{H}_2^+$	$2.9 \times 10^{-10} T_g^{0.59}$	quantal calc.	(n)
17)	$\text{LiH} + \text{H}^+ \rightarrow \text{LiH}^+ + \text{H}$	$-2.6 \times 10^{-10} T_g^{0.60} \exp(-400/T_g)$	quantal calc.	(o)
18)	$\text{LiH} + \text{H}^+ \rightarrow \text{Li}^+ + \text{H}_2$	$1.0 \times 10^{-9}$	estimate	(e)
		$1.0 \times 10^{-9}$		
<b>LiH<sup>+</sup> reactions</b>				
19)	$\text{LiH}^+ + \text{H} \rightarrow \text{Li}^+ + \text{H}_2$	$8.7 \times 10^{-10} T_g^{0.040} \exp(T_g/5.92 \times 10^8)$	quantal calc.	(p)
20)	$\text{LiH}^+ + \text{H} \rightarrow \text{Li} + \text{H}_2^+$	$9.0 \times 10^{-10} \exp(-66400/T_g)$	estimate	(e)
21)	$\text{LiH}^+ + \text{H} \rightarrow \text{LiH} + \text{H}^+$	$1.0 \times 10^{-11} \exp(-67900/T_g)$	estimate	(e)
22)	$\text{LiH}^+ + e \rightarrow \text{Li} + \text{H}$	$3.9 \times 10^{-6} T_g^{-0.70} \exp(-T_g/1200)$	quantal calc.	(q)
<b>photoreactions</b>				
23)	$\text{LiH} + h\nu \rightarrow \text{Li} + \text{H}$		det. bal. applied to (3)	
24)	$\text{LiH}^+ + h\nu \rightarrow \text{Li}^+ + \text{H}$		det. bal. applied to (10)	
25)	$\text{LiH}^+ + h\nu \rightarrow \text{Li} + \text{H}^+$		det. bal. applied to (5)	
26)	$\text{Li} + h\nu \rightarrow \text{Li}^+ + e$		det. bal. applied to (11)	
27)	$\text{Li}^- + h\nu \rightarrow \text{Li} + e$		quantal calc.	(h)
28)	$\text{LiH} + h\nu \rightarrow \text{Li}(^2p) + \text{H}$		det. bal. applied to (1), (2)	

(a) Gianturco & Gori Giorgi (1996) [6]; (b) Bennett et al. (2003, 2008) [7,8]; (c) Dalgarno, Kirby & Stancil (1996) [9]; (d) Gianturco & Gori Giorgi (1997) [10]; (e) Stancil, Lepp & Dalgarno (1996) [5]; (f) Kimura, Dutta & Shinakura (1994) [11]; (g) Stancil & Ziegler (1996) [12]; (h) Ramsbottom, Bell & Berrington (1994) [13]; (i) Bulut et al. (2009) [14]; (j) Pino et al. (2008) [16]; (k) Verner & Ferland (1996) [17]; (l) Croft, Dickinson & Gad a (1999) [18]; (m) our new calculations; (n) our new calculations; (o) Bulut et al. (2008) [15]; (p) our new calculations (q) Curik & Greene (2007, 2008) [20, 21].

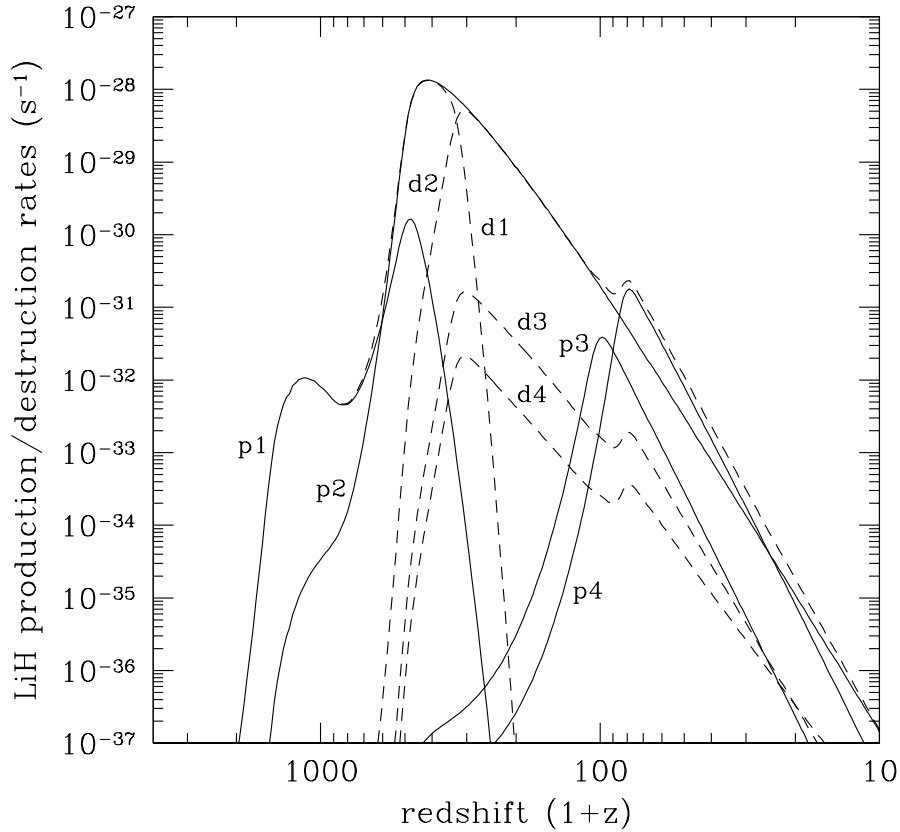


Figure 7.1 Computed production/destruction rates of LiH as function of redshift. Solid and dashed curves represent production and destruction processes, respectively.

redshifts. The same reactive process with protons ( $d_3$ ) is seen to be less important, although larger than previous estimates ( $d_4$ ).

In conclusion, the above data indicate that the radiative photoassociation from the  $n = 25$  level of Li is the most significant formation path, while the collisional destruction by H ( $d_2$ ) overcomes production over the whole range of redshifts below 300.

### 7.2.2 LiH<sup>+</sup> chemistry

Figure 7.2 shows the processes leading to the formation and the destruction of LiH<sup>+</sup>, labelled as  $p_1^+, \dots, p_2^+$  and  $d_1^+, \dots, d_4^+$  as in Table 7.2. As clearly shown by the figure, the radiative association processes ( $p_1^+$  and  $p_2^+$ ) are seen to dominate the formation of LiH<sup>+</sup> over a very broad range of redshifts. The association involving the Li ion ( $p_1^+$ ) is the major pathway down to about  $z \simeq 700$ , when the reaction of H<sup>+</sup> with neutral Li ( $p_2^+$ ) takes over and becomes dominant by several orders of magnitude

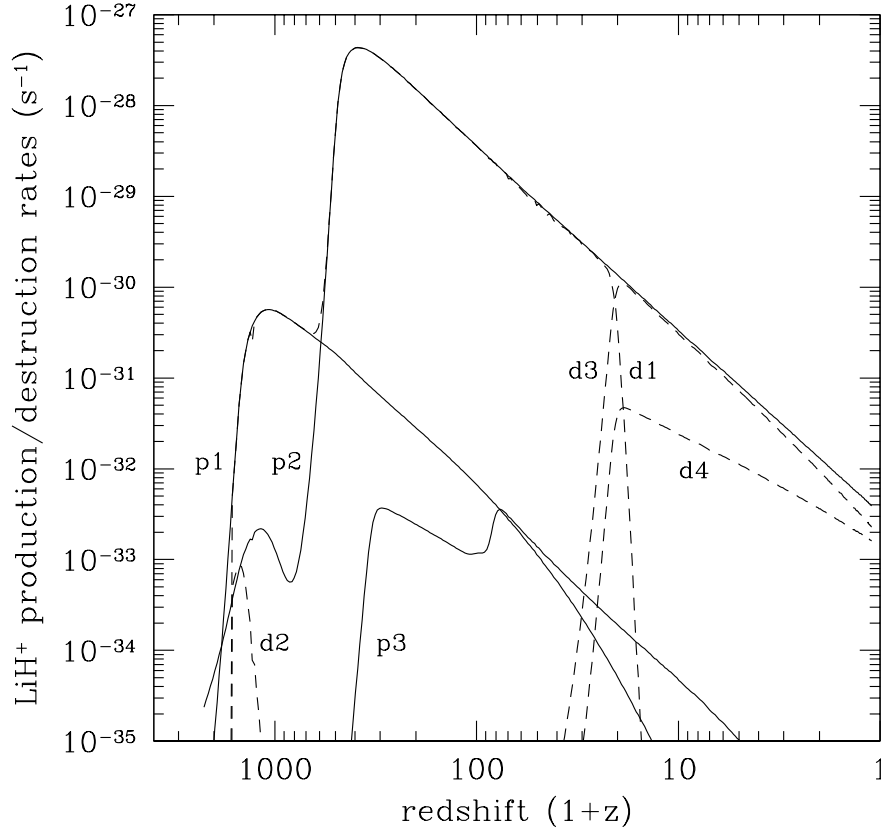


Figure 7.2 Computed production/destruction rates of  $\text{LiH}^+$  as function of redshift. Solid and dashed curves represent production and destruction processes, respectively.

over the rates of the charge-exchange reaction ( $p_3^+$ ) estimated by Stancil et al [5].

As for the destruction processes for  $\text{LiH}^+$ , one sees that photodissociation ( $d_1^+$ ) is the dominant destruction path of the ionic molecule, due to its small dissociation energy value. Furthermore, the dominant dissociation channel comes from  $\text{Li}^+$  production ( $d_3^+$ ), while the one yielding  $\text{H}^+$  ( $d_2^+$ ) is relevant only at the highest redshifts. The electron-induced dissociation ( $d_4^+$ ) was earlier based on a simple estimates from [5] while now we have included the more accurate quantum calculations from Čurik & Greene [20,21] which yield much larger rates. It turns out to be important only at low redshifts. On the other hand, the chemical paths which involve the reactions that destroy  $\text{LiH}^+$  ( $d_3^+$ ) are seen to be indeed the most important processes around  $z \simeq 40$  while becoming less efficient than the  $d_4^+$  process below  $z \simeq 10$ . The electron-assisted dissociation of  $\text{LiH}^+$  ( $d_4^+$ ) is therefore important only at the lowest redshifts.

In summary, the ionic formation is dominated by the radiative association of Li

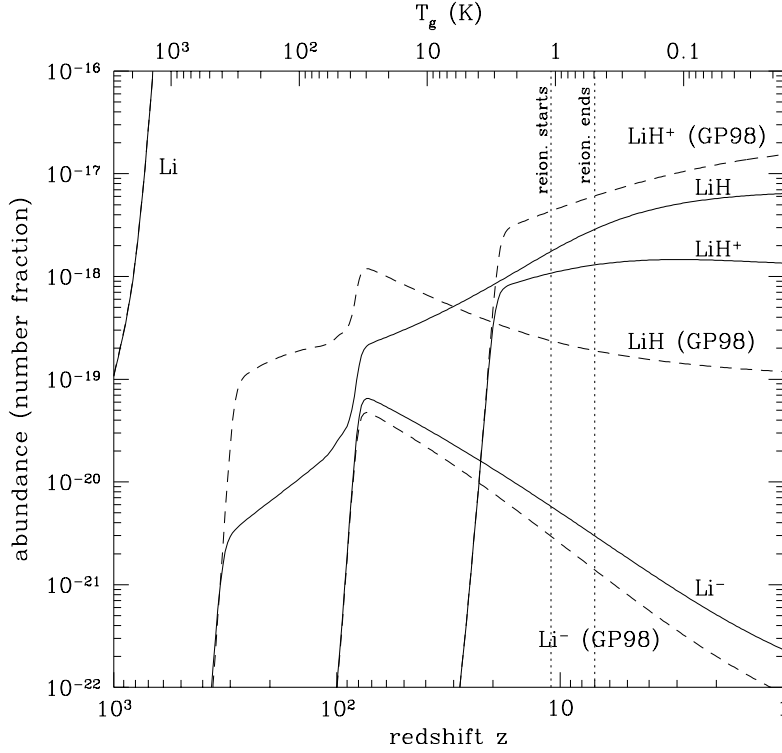


Figure 7.3 Relative abundances of Li, Li<sup>-</sup>, LiH, and LiH<sup>+</sup> in the post-recombination era as function of redshift  $z$  (lower scale) and gas temperature  $T_g$  (upper scale): present results (solid curves), results of [3] (dashed curves). The dotted lines at  $z=11$  and  $z=7$  indicate the approximate redshifts at which reionization of the primordial gas starts ( $z \simeq 11$ ) and is completed ( $z \simeq 7$ ), according to Spergel et al [19].

with H<sup>+</sup> over a very broad range of redshifts, while destruction by photodissociation prevails at larger redshift and chemical destruction ( $d_3^+$ ) dominates at lower redshifts. However, down to  $z \simeq 1$  the dissociative neutralization ( $d_4^+$ ) is markedly dominant.

### 7.2.3 Chemical evolution

The new evolution of relative abundances of atomic and molecular species involving Li is displayed in Figure 7.3, comparing the earlier results obtained with the chemical network of [3] (dashed lines) and the present results (solid lines) which employ the new quantum rates. The main results are the following:

(i) The temperature dependence of the quantum rates is clearly reflected in the molecular abundances of LiH at redshifts below  $z \sim 300$ . The rapid rise of LiH at  $z \sim 300$  found by [3] is no longer seen owing to the increased destruction rate of channel (1). The rise at  $z \sim 100$  is due to the importance of LiH formation by Li<sup>-</sup>

T(K)	$\alpha$ (cm <sup>3</sup> s <sup>-1</sup> )
1	$4.41 \times 10^{-12}$
5	$2.11 \times 10^{-11}$
10	$5.47 \times 10^{-11}$
20	$1.33 \times 10^{-10}$
30	$2.11 \times 10^{-10}$
50	$3.43 \times 10^{-10}$
70	$4.39 \times 10^{-10}$
80	$4.76 \times 10^{-10}$
100	$5.33 \times 10^{-10}$
200	$6.76 \times 10^{-10}$
300	$7.39 \times 10^{-10}$ $9.10 \pm 2.5 \times 10^{-10}$ (*)
500	$8.08 \times 10^{-10}$
800	$8.70 \times 10^{-10}$

(\*) experimental (Karpas et al. 1979)

Table 7.3 Computed rate coefficient for the reaction  $\text{HeH}^+ + \text{H}$  as a function of T.

that persists at all redshifts together with the radiative association of Li with H. This is drastically different from the behavior found by [3] where the constant value of the rate for reaction (1) caused the steady drop of LiH. The final ( $z = 0$ ) value of LiH is  $\sim 7 \times 10^{-18}$  with an increase of a factor of  $\sim 70$  relative to [3].

(ii) Due to the differences in behavior shown by the cross sections, the ionic partner,  $\text{LiH}^+$ , behaves differently at  $z \leq 30$ . First, the increased efficiency of  $\text{LiH}^+$  destruction (reaction 3; rate  $d_3^+$ ) limits the sharp rise in abundance at  $z \sim 20$ . Then, the gentle decline below  $z \sim 5$  is due to the efficiency of electronic recombination (rate  $d_4^+$ ). The new final abundances of  $\text{LiH}^+$  (solid line) is now smaller than earlier estimates of [3] by a factor of  $\sim 20$ .

The scenario emerging from the above calculations therefore indicates that in the regions of redshift below  $z \simeq 30$ , LiH remains the more abundant species compared to  $\text{LiH}^+$ , but only by a factor of  $\sim 2$ –7. The two molecular abundances, on the other hand, reach the largest values for  $z \leq 10$ , remaining both fairly small ( $\text{LiH} \sim 10^{-17}$ ,  $\text{LiH}^+ \sim 10^{-18}$ ) and hard to detect.

### 7.3 The helium chemistry

The new rate coefficients are reported in Table 7.3 and fitted with the formula

$$\alpha(T) = 4.3489 \times 10^{-10} T^{0.110373} e^{(-31.5396/T)}, \quad (7.8)$$

which is valid for  $T \leq 1000$  K. The experimental value obtained by Karpas et al [22] is also reported for comparison in the same Table. It is again very reassuring to see that the only existing experimental datum at 300 K is indeed very close to our computational value at the same temperature. To more clearly evaluate the significance of the newly computed cross-sections, we need to view the depletion

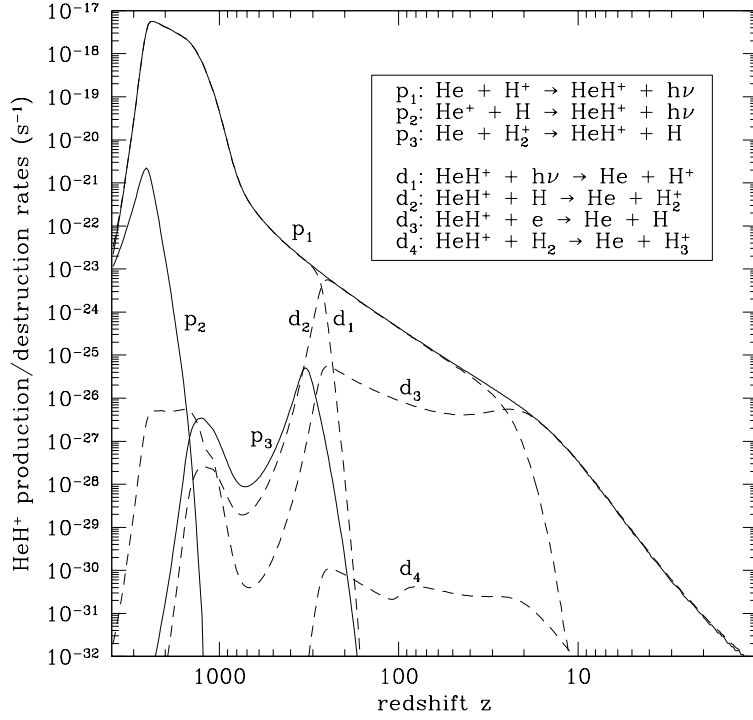


Figure 7.4 Computed production/destruction rates of  $\text{HeH}^+$  as function of redshift.

process within the broader context of the variety of elementary events involved in this molecular cation. To this end, Figure 7.5 shows the main processes leading to the formation and the destruction of  $\text{HeH}^+$ . As clearly shown by the figure, the radiative association process ( $p_1$ ) dominates the formation of  $\text{HeH}^+$  over the entire range of redshifts, while the association involving the He ion ( $p_2$ ) and the other involving the  $\text{H}_2^+$  molecule ( $p_3$ ), have negligible contributions at the lower redshift values, the most important range for the present study.

From the same figure one further realizes that the photodissociation mechanism ( $d_1$ ) is the dominant destruction path of the  $\text{HeH}^+$  for  $z \geq 300$ , while the chemical path involving the reaction (2), the one that destroys  $\text{HeH}^+$  ( $d_2$ ) in collision with H, is seen to be the most important process for  $z \leq 300$ . A contribution also comes from the electron-assisted dissociation reaction ( $d_3$ ) that neutralizes the charged partners and dominates over ( $d_2$ ) for  $z \leq 10$ .

In Figure 7.5 we report the calculated abundances for  $\text{HeH}^+$  obtained using our new quantum rates discussed above: they are compared with the old ones obtained by [3] and also with our newest results for  $\text{LiH}^+$ . The scenario emerging from the above calculations indicates that for redshift around  $z \simeq 20$ , the molecular  $\text{HeH}^+$  abundance has now increased by more than one order of magnitude with respect to the earlier calculations. It thus remains a more abundant ionic species than

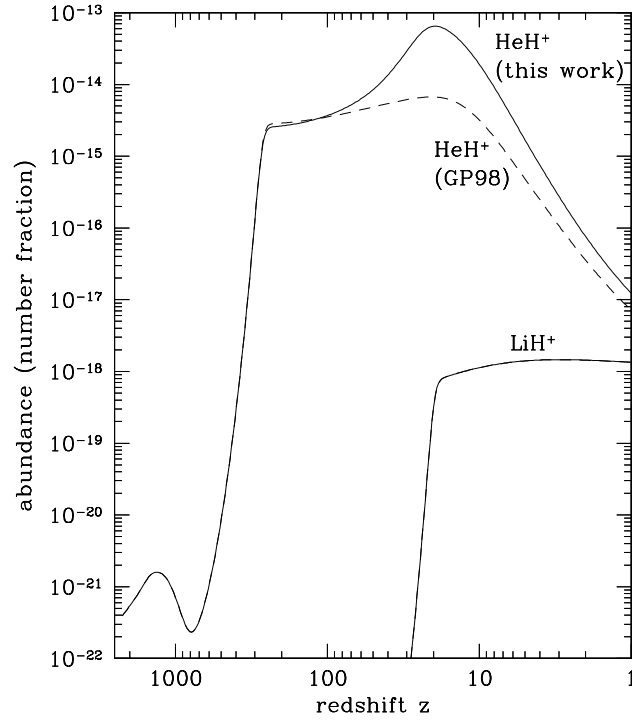


Figure 7.5 Computed relative abundances of  $\text{HeH}^+$  in the post-recombination era as function of redshift  $z$ : present results (solid curves), results of [3] (dashed curves).

$\text{LiH}^+$ , hence becoming an interesting molecular candidate for actual detection. As shown by Maoli et al [23] (see also Schleicher et al [24]), the relevant quantity for determining the imprint of molecules on the CMB is the optical depth due to line absorption. In the case of  $\text{HeH}^+$ , the optical depth has a broad peak around a frequency of  $\sim 50$  GHz, produced by redshifted rotational transitions with  $j = 4-6$  of the ground vibrational level. With the new rate coefficient derived in this work, the maximum value of the optical depth,  $\sim 10^{-7}$ , is about one order of magnitude larger than the value computed earlier by Schleicher et al [24], an encouraging result for observational perspectives. The new reaction rate also has an effect on the abundance of  $\text{H}_2^+$ , which is lower by a factor of  $\sim 5$  in the range  $10 \leq z \leq 50$  than earlier results. However, this reduction has no significant effect on the abundance of  $\text{H}_2$  because the  $\text{H}_2^+$  channel of production of  $\text{H}_2$  is no longer active at these redshifts.





# Bibliography

- [1] Smith M. S., Kawano L. H. and Malaney R. A., ApJS, **85**, 219, 1993
- [2] Komatsu, E., et al., ApJS, **180**, 330, 2009
- [3] Galli D., Palla F., A&A, **335**, 403, 1998
- [4] Bougleux E. and Galli D., MNRAS., **288**, 638, 1997
- [5] Stancil P. C., Lepp S. and Dalgarno A., Astrophys. J., **458**, 401, 1996
- [6] Gianturco F. A. and Gori Giorgi P., Phys. Rev. A., **54**, 1, 1996
- [7] Bennett O.J., Dickinson, A.S., Leininger, T., Gadéa, F.X., MNRAS, **341**, 361, 2003
- [8] Bennett O. J., Dickinson A. S., Leininger T. and Gadéa F. X., MNRAS, **384**, 1743, 2008
- [9] Dalgarno A., Kirby K. and Stancil P. C., ApJ, **458**, 397, 1996
- [10] Gianturco F. A. & Gori Giorgi P., ApJ, **479**, 560, 1997
- [11] Kimura M., Dutta C. M. and Shimakura N., ApJ, **430**, 435, 1994
- [12] Stancil P. C. and Zygelman B., ApJ, **472**, 102, 1996
- [13] Ramsbottom C. A., Bell K. L. and Berrington K. A., J. Phys. B, **27**, 2905, 1994
- [14] Bulut N., Castillo J. F., Banares L., Aoiz F. J., J. Phys. Chem. A, **113**, 14657, 2009
- [15] Bulut N., Castillo J. F., Aoiz F. J., and Banares L., Phys. Chem. Chem. Phys., **10**, 821, 2008
- [16] Pino I., Martinazzo R., & Tantardini G., Phys. Chem. Chem. Phys., **10**, 5545, 2008
- [17] Verner D. A., Farland G. J., ApJS, **103**, 467, 1996
- [18] Croft H., Dickinson A. S. and Gadéa F. X., MNRAS, **304**, 327, 1999
- [19] Spergel D. N., et al., ApJS, **170**, 377, 2007
- [20] Curík R. and Greene C. H., Phys. Rev. Lett., **98**, 173201, 2007
- [21] Curík R. and Greene C. H., J. Phys.: Conference Series, **115**, 012016, 2008
- [22] Karpas Z., Anicich V., and Huntress, Jr. W. T., J. Chem. Phys., **70**, 2877, 1979
- [23] Maoli R. et al., ApJ, **425**, 372, 1994
- [24] Schleicher, D. R. G., Galli, D., Palla, F., Camenzind, M., Klessen, R. S., Bartelmann, M., & Glover, S. C. O. A&A, **490**, 521, 2008

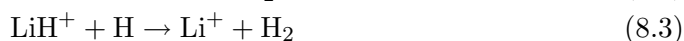


# 8

## Conclusions

As discussed in previous chapters, the first galaxies and stars were formed from an atomic gas of chiefly H and  $^4\text{He}$  with trace amounts of D,  $^3\text{He}$  and  $^7\text{Li}$ . Since there was a clear absence of heavier elements, the necessary radiative cooling kinetics below 8000 K must have been controlled by a small fraction of that gas which was molecular, in order to make more efficient the collapse of the primordial clouds. In the present work we have focused on the study of the chemistry of some of the most important molecular species expected to be already formed via radiative recombination during the early universe stage, LiH,  $\text{LiH}^+$  and  $\text{HeH}^+$ , to understand from ab-initio calculations how likely it would be for them to survive the chemical reactions with the very abundant hydrogen gas existing under those conditions. To do this, a theoretical/computational tool to describe, at a quantum level, an atom-molecule reactive scattering process is needed. The common packages available to study such problems, like ABC [1], have been used only for the  $\text{LiH} + \text{H}$  reaction. The huge computational time asked from the latter and some physical restrictions convinced us to develop a new quantum reactive code based on the negative imaginary potential (NIP) which is less time consuming and allow us to obtain results with a good level of accuracy as proved by the benchmark calculations presented in sec. 4.2.

We have carried out quantum calculations of the reactive processes that are allowed at the existing conditions of those clouds and which essentially involve the exothermic channels of the following reactions:



The  $\text{H}_2$  formation process 8.1 which describe the destruction of the initial molecular LiH has been studied by employing a newly obtained PES [2] and carrying out a coupled-channel study of the quantum reaction, summing over all possible final states of  $\text{H}_2$ . Furthermore we analyzed the possible changes due to having the initial LiH molecule formed in some of its excited vibrational levels. The final rates were obtained by employing the uniform  $J$ -shifting procedure described in sec. 3.2.1. The rates for both events (i.e. H replacement and  $\text{H}_2$  formation) were thus ob-

## Conclusions

---

tained over a very broad range of redshift values, covering those that pertain to the recombination era (sec. 5.1.1).

The present calculations are the first quantum results, in regions of astrophysical interest, which employ both the "exact" coupled-channel dynamics and the best, thus far, reactive potential energy surface obtained from *ab-initio* computations. They allowed us to make the following points:

- to have the initial molecule excited in any of its internal vibrational states does not modify the above result, albeit showing an increase of the simple H-replacement rates as  $\nu$  increases;
- the analysis of the rates of  $\text{H}_2$  formation into different roto-vibrational levels indicates that such species is preferentially formed into its lower  $(\nu', j')$  states, although the formation of internally "hot"  $\text{H}_2$  molecules is far from negligible;
- formation of either  $\text{oH}_2$  or  $\text{pH}_2$  changes very little the computed rate values, thereby not influencing the above findings;
- the computed rates with the present PES turn out to be larger than the earlier calculations which used a less accurate form of reactive interaction [4, 5] and similar in size to the earlier, empirical estimates by Stancil et al [6].

An accurate quantum analysis of another destruction mechanism involving LiH species, this time reacting with the abundant ionic partner  $\text{H}^+$  (eq. 8.2), has been also considered in order to extend the existing information about this very important chemical evolution network. All the features we found indicate a sizeable but limited disappearance of LiH in collision with  $\text{H}^+$ , also a very abundant species in the redshift range considered. Although these findings confirm the above to be a likely secondary destruction mechanism, the final abundance of LiH may however not be markedly different from the one surmised by eq. 8.1, although still further reduced by reaction 8.2.

When we turn to the ionic  $\text{LiH}^+$ , besides its being important in the formation of the LiH molecules through the exchange reaction ( $\text{LiH}^+, \text{H}$ ), we find that it is a molecule which could have survived at low redshifts.

We therefore have carried out quantum reactive calculations for the exothermic reaction of the  $\text{LiH}^+$  molecular cation with hydrogen atom (eq. 8.3) at the temperatures corresponding to the redshifts important for the lithium chemistry in the early universe environment ( $z < 400$ ). The aim of this work has therefore been to try and establish from first principles the likely efficiency of the depletion rates associated with the ionic lithium molecule once it is formed by association reaction during the recombination era (in particular  $z < 400$ ). The present calculations were carried out by employing an accurate, *ab initio* reactive PES [7] and using a quantum modelling of the reaction process. The most important final channels were also compared with recent semiclassical studies [8] on the same system. We found from our calculations that the exothermic process is the dominant reactive process that leads to density reduction for the cationic hydride.

Having obtained accurate rates from quantum dynamics, we have been able to assemble a more realistic chemical network for the first stages of Universe formation

---

(chapter 7). Then, the present work has revisited the analysis of all the dynamical processes that are known to significantly contribute to the production/destruction of the lithium-containing molecules. We have employed as many results as possible from calculations based on ab-initio methods, both for the interaction forces and the quantum dynamics, resorting to estimates only for a few of the considered processes.

One of the main results from the quantum reactive calculations is that two of the important rates exhibit a temperature dependence that was not present in the earlier estimates.

The results for the abundance of LiH indicate that this molecule is much more likely to have survived at low redshift, since its fractional abundance, albeit still fairly small, goes up by a factor of  $\sim 70$  compared to previous estimates. However, it becomes smaller by nearly the same amount for  $z > 300$ .

The fractional abundance of  $\text{LiH}^+$  only becomes significant in the low-redshift region of  $z \leq 30$  and shows a reduced value of the relative abundance by about one order of magnitude with respect to the earlier estimates. The comparison between the specific fractional abundances of the two species now indicates that the neutral molecule is likely to be more abundant than the ionic species and that their ratio in the region of small redshift increases up to a factor of 7 down to  $z \simeq 1$ . Unlike previous estimates that predicted a difference at low- $z$  of about two orders of magnitude in favor of  $\text{LiH}^+$ , the new calculations find more comparable abundances of LiH and  $\text{LiH}^+$ . Furthermore, we found that the neutral molecule, in spite of a large dilution at the low redshifts, should be more amenable to experimental observation [9] than its ionic counterpart.

Finally, given the recent studies (e.g. see [10]) on the possible detection, within the microwave background anisotropies, of the earlier imprint from the recombination history of lithium, the present results strongly suggest that such anisotropies could be amenable to observation due to the changed optical depth induced by the changes on lithium abundances.

The relevant importance given to the  $\text{HeH}^+$  molecule as probe for the early universe conditions, has pushed us to revise, more accurately, also the evolution of this molecule. We have carried out a new set of ab initio, quantum calculations for the rate coefficient of the reaction 8.4, which therefore permit us to revise the abundance of  $\text{HeH}^+$  molecule within the expected conditions operating during the early universe. One of the main results from the present reactive calculations is that the chemical destruction rate of this polar cation depends on temperature in a way that is very different from previous data, both experimental and theoretical, especially for temperatures lower than 100 K.

These new results obtained for the  $\text{HeH}^+$  abundance now indicate that this molecule should be much more likely to have survived at low redshift, since its fractional abundance goes up by more than one order of magnitude from previous estimates, becoming of the order of  $10^{-13}$ . Comparing the specific fractional abundances of the two species therefore suggests rather compellingly that the  $\text{HeH}^+$  ionic molecule, if more abundant than the  $\text{LiH}^+$ , would become more likely to be observed experimentally.

We note that, because of its larger dipole moment and greater number of roto-vibrational levels, when compared with  $\text{LiH}^+$ , the molecular cation  $\text{HeH}^+$  turns out

## Conclusions

---

to be the most suitable candidate for experimental observations in different astrophysical environments, a result now supported by the present ensemble of accurate computational studies from quantum, ab initio methods.

Finally, we decided to analyze, for the first time, the  $\text{LiHe}^+$  molecule, which has received no attention in the past. The photoassociation and photodissociation rates have been calculated together with the chemical routes which lead to the destruction of the  $\text{LiHe}^+$  in reaction with H and its inverse reaction. The rate constants have been then employed within a partial chemical network to see how abundant this molecule could be. The work is still in progress because we need to complete the network of reactions that include the dissociative recombination, but the preliminary results show an abundance which is more than three orders of magnitude lower than that for LiH and  $\text{LiH}^+$ , thereby exiling  $\text{LiHe}^+$  to a minor role within the present chemical network.

# Bibliography

- [1] Skouteris D., Castillo J. F. and Manolopoulos D. E., *Comp. Phys. Comm.*, **133**, 128, 2000
- [2] Wernli M., Caruso D., Bodo E., and Gianturco F. A., *J. Phys. Chem. A*, **113**, 1121, 2009
- [3] Zhang D. H. and Zhang J. Z. H., *J. Chem. Phys.*, **110**, 7622, 1999
- [4] Padmanaban R. and Mahapatra S., *J. Chem. Phys.*, **121**, 7618, 2004
- [5] Defazio P., Petrongolo C., Gamallo P. & González M., *J. Chem. Phys.*, **122**, 214303, 2005
- [6] Stancil P. C., Lepp S., and Dalgarno A., *ApJ*, **458**, 401, 1996
- [7] Martinazzo R., Bodo E., Gianturco F. A., & Raimondi M., *Chem. Phys.*, **287**, 335, 2003
- [8] Pino I., Martinazzo R., & Tantardini G., *Phys. Chem. Chem. Phys.*, **10**, 5545, 2008
- [9] Persson, C. M., et al., *A&A*, **515**, A72, 2010
- [10] Zalagarriaga M., and Loeb A., *ApJ*, 564, 52, 2002





## 9.1 My work at the Harvard-College Center for Astrophysics

---

When someone evokes the word "Harvard" always arouses a strange reaction to the interlocutor, a gasp followed by a feeling of non-tangibility (something ethereal). For a young scientist, the great american universities are indeed the top step to be reached, that impossible which becomes rarely possible.

The first time I arrived in Cambridge, in April 2008, I was permeated by these strange sensations, something like an hesitation which later became normality. I had the honor of working at the Harvard-College Center for Astrophysics for nine months, four of which during my PhD program, and I met exceptional people, humanly and scientifically. I always like to tell about my first business meeting with prof. Alex Dalgarno, prof. Vasili Kharchenko and Dr. Peng Zhang, about my huge embarrassment at my poor English. I left that meeting a little bit confused, but over the time I did my best to work well and in tune with these new colleagues (who also became new friends).

The work done in the summers of 2009 and 2010 led to the publication of two papers [1, 2], but we made with Vasili and Peng other work and we obtained other results which have not yet been published but deserve a mention because they were proposed with the proper scientific spirit and with the unique motivation of passion for the natural phenomena.

A very good mathematician (Vasili) and a very good computational man (Peng) always have an ace up their sleeves to pull out at the appropriate time, as it often also occurred during our tennis games!

In the next section, I will briefly describe, without going into details, some of the aspects of the work I did at the Center for Astrophysics in the group of Prof. A. Dalgarno and the results we obtained.

## 9.2 The energy transfer processes

---

An accurate theoretical description of the translational energy relaxation of energetic atoms and molecules is fundamental to a wide variety of fields of chemical physics, plasma physics, planetary science and astrophysics. Sources of energetic particles may have very different parameters and character, but the collisional mechanism of energy relaxation is similar in different non-equilibrium systems. The theoretical basis for an accurate description of the energy relaxation process is the Boltzmann

kinetic equation. We consider the energy relaxation of fast atoms in an infinite uniform bath gas. If the density of bath gas is much larger than that of the projectile particles, collisions between projectiles may be neglected and evolution of the energy distribution function of fast particles can be described by the linear form of the Boltzmann equation [3]. Closed analytical expression of the kernel of this Boltzmann equation can be obtained using the fully energy and angular dependent collision cross sections [4]. The time-dependent solution of the Boltzmann equation can then be computed and used for different applications. Successful implementations of this method have been reported in the study of the thermalization problem in physical chemistry, atmospheric physics and applied atomic spectroscopy [5–7].

### 9.2.1 Kernel of Boltzmann equation

The energy evolution of atoms due to elastic and inelastic collisions with a uniform bath gas has been considered by Kharchenko *et al.* [8,9]. The rate of energy transfer of the projectile atoms from initial energy  $E'$  to final energy  $E$  in the laboratory frame (LF) is given by the kernel of the Boltzmann equation  $B(E|E')$ . In a uniform bath gas the energy distribution  $f(E, t)$  of the projectile can be described by the linear Boltzmann equation

$$\frac{\partial}{\partial t}f(E, t) = \int B(E|E')f(E', t)dE' - f(E, t) \int B(E'|E)dE' - \zeta(E)f(E, t) + Q(E, t), \quad (9.1)$$

where  $Q(E, t)$  is the rate of production of the atoms with energy  $E$  and  $\zeta(E, t)$  is the rate of the sink reactions that remove them. For binary elastic and inelastic collisions,  $B(E|E')$  can be derived analytically through the double differential cross-section  $d^2\sigma/d\Omega d\varepsilon$  [8,9] and in the case of elastic scattering, the energy relaxation  $B(E|E')$  can be calculated using the differential cross section

$$B(E|E') = \frac{n_b m^{3/2}}{2\sqrt{2}\pi\mu^2} \sqrt{E} \int \frac{d\sigma(\varepsilon, \cos\chi)}{d\Omega} \rho(\mathbf{p}'_b) d\mathbf{p}'_b d\Omega_{\mathbf{p}} d\Omega_{\mathbf{p}'}, \quad (9.2)$$

where  $m$  is the mass of the projectile,  $\Omega_{\mathbf{p}'}$  and  $\Omega_{\mathbf{p}}$  are the solid angles of the initial and final momenta in the LF for fixed  $|\mathbf{p}'| = \sqrt{2mE'}$  and  $|\mathbf{p}| = \sqrt{2mE}$ ,  $n_b$  is the density of the bath gas, and  $\rho(\mathbf{p}'_b)$  is the Maxwellian-Boltzmann distribution function of the bath gas. The solution of equation (5) may be written

$$f(E, t) = \int_0^t \int_0^\infty K(E, t|E', t') Q(E', t') dE' dt', \quad (9.3)$$

where the propagator  $K(E, t|E', t')$  describes the energy evolution of the projectile atoms created at the time  $t'$  with energy  $E'$ . If the initial function  $f(E, t = 0)$  is given,  $f(E, t)$  at a later time  $t$  may be calculated from the propagator  $K(E, t|E', t)$  according to

$$f(E, t) = \int K(E, t|E', 0) f(E', 0) dE'. \quad (9.4)$$

The equation 9.4 can be solved numerically [10, 11] by defining the function  $f(E, t)$  in a given energy range  $[0, E_{max}]$  and using a discretized kinetic equation for the kernel, defined as a  $N \times N$  matrix [3] with the energy grid of  $\delta E$

$$A_{ij} = \delta E [B(i\delta E | j\delta E) - \delta_{ij}\omega(i\delta E)], \quad (9.5)$$

where  $\delta_{ij}$  is the Kronecker delta and:

$$\omega(E) = \int_0^\infty B(E | E') dE', \quad (9.6)$$

The time-dependent distribution function is generated from the initial distribution function  $f(E, 0)$ :

$$f(E, t) = e^{t\mathbf{A}} f(E, 0), \quad (9.7)$$

and the time-dependent average translational energy is obtained from:

$$\langle E(t) \rangle = \int f(E, t) E dE. \quad (9.8)$$

---

## 9.3 The results

### 9.3.1 S-Xe

Sulfur species have been detected in the upper atmospheres of Jupiter and Titan [12], and atomic sulfur is the dominant atmospheric constituent in Jupiter's satellite, Io [13]. Energetic S(<sup>1</sup>D) is produced by the photodissociation of OCS and H<sub>2</sub>S molecules and the study of energy transfer with other atmospheric gases is important for understanding the energy balance of the upper atmosphere and its evolution. Laboratory experiments involving the energy and speed relaxation of S(<sup>1</sup>D) atoms in collisions with planetary and atmospheric gases, such as N<sub>2</sub>, O, H, and N are challenging, but investigations of S energy relaxation in rare gases have been carried out [14]. These experiments concluded that for energy relaxation in heavy bath gases, such as Xe, the effective cross sections, describing the energy transfer collisions, depend strongly on kinetic energy. These conclusions have been drawn in comparisons of the experimental data on the time-dependent energy relaxation of fast S atoms with the results of Monte Carlo simulations of the S(<sup>1</sup>D) thermalization process. Monte Carlo simulations had been carried out using the hard-sphere approximation (HSA) model of atomic collisions. The additional assumption of a completely frozen bath gas was made in these simulations. For collisions of neutral atoms or molecules the HSA is a serious misrepresentation. It does not reproduce the strong forward scattering that arises from the attractive long-range van der Waals interaction and it ignores the energy dependence of the collisional cross sections. For elastic collisions of real atomic particles, the translational energy losses occur by a series of highly probable collisions with relatively small energy transfer occurring in each of these sequential collisions. Therefore the value of energy transferred per collision and the number of collisions derived by HSA are misleading.

We have carried out a full theoretical description of the thermalization process by computing accurate angular-dependent cross sections for energy transfer collisions between S and Xe atoms and solving the time dependent Boltzmann equation 9.1 that describes the energy relaxation. Our calculations, starting with *ab initio* quantum mechanical calculations of the interaction potential in the S+Xe system, have no adjustable parameters. Elastic differential cross sections were evaluated quantum mechanically and used to construct the kernels of the Boltzmann equation, describing the rate of energy transfer collision in the LF. The corresponding time-dependent solutions of the Boltzmann equation were obtained by propagating the LF energy distribution function.

Our calculations are compared to the experimental data from ref. [14]. In their paper Nan and Houston [14] presented an analysis of their experimental data and obtained the average relative speed of S and Xe collisions as a function of the number of collisions.

The average relative speed  $\langle v_i \rangle$ ,  $\vec{v}_i = \vec{v}_p - \vec{v}_b$ , in our work was found by averaging the absolute value of relative velocity over a Boltzmann distribution  $f(v_b)$  of the bath gas,

$$\langle v_i \rangle = \langle |\vec{v}_i| \rangle = \int_0^\infty v_i f(v_b) d^3 v_b, \quad (9.9)$$

where  $v_p$  and  $v_b$  are velocities of the projectile and the bath gas atoms respectively. We found

$$\langle v_i \rangle = v_T \left[ \sqrt{\frac{2}{\pi}} e^{-\frac{v_p^2}{2v_T^2}} + \text{Erf} \left[ \frac{v_p}{\sqrt{2}v_T} \right] \left( \frac{v_p}{v_T} + \frac{v_T}{v_p} \right) \right], \quad (9.10)$$

where  $v_T$  is defined as

$$v_T = \sqrt{\frac{k_B T}{m_b}}, \quad (9.11)$$

$k_B$  is the Boltzmann constant,  $T$  is the temperature of the bath gas and Erf is the error function. Consistent results for the time dependent relative velocity were observed except at long relaxation times. The strong energy dependent relaxation cross sections are responsible for the difference between the results of our *ab initio* calculations and prediction of the Monte Carlo simulation with the hard sphere model [14]. The relative velocity reported in the experiment was obtained with the aid of HSA Monte Carlo simulation. *Ab initio* calculations yield a larger number of collisions than HSA to reach equilibrium, reflecting the physical characteristics of the energy transfer process.

### 9.3.2 Helium escape from Mars atmosphere

Helium is one of the dominant constituents in the upper atmospheres of Mars and Venus [15]. Helium escape is crucial for understanding the evolution of the Martian atmosphere and modeling elemental abundances in Mars' interior [16, 17]. Information on the He balance in the upper atmosphere is also important for analysis of the interaction between the solar wind and the Martian exosphere [16]. Since Mars has a negligible intrinsic magnetic field [18], the solar wind can penetrate deeply into the neutral corona. This process contributes to a global erosion of the atmosphere but

also provides additional He atoms due to neutralization of  $\alpha$ -particles. The thermal (Jeans') escape of He is negligible on Mars [19] and the major mechanism of escape is the collisional ejection of He atoms by energetic oxygen. This process turns out to dominate over ion-related mechanisms [20] and to obtain an accurate evaluation of the escape flux of neutral He becomes a fundamental issue. The dissociative recombination of  $\text{O}_2^+$  ions is the major source of energetic oxygen atoms [21–24]. The rate of production of energetic oxygen atoms varies with solar activity [25]. We report below the results of an accurate evaluation of the energy transfer from hot  $\text{O}(^3\text{P}, ^1\text{D})$  atoms to the atmospheric He gas. We have calculated angular dependent cross sections for collisions of hot  $\text{O}(^3\text{P}, ^1\text{D})$  atoms with the thermal  $^4\text{He}$  and  $^3\text{He}$  atoms and constructed the kernel of the Boltzmann equation. Energy distribution functions of the He recoil atoms have been computed at different altitudes and the He loss rate is evaluated for the Martian upper atmosphere at low solar activity.

Distributions of the secondary hot atoms produced in recoil collisions with energetic oxygen are crucial for the determination of the escape flux of the He atoms from terrestrial planets. The escape energies ( $E_{esc}$ ) of  $^4\text{He}$  and  $^3\text{He}$  in the Martian atmosphere are 0.48 eV and 0.36 eV respectively. If the recoil atoms gain enough energy in the upward direction, they could escape from that atmosphere. Reliable estimates of the He escape flux can be made using the Boltzmann kernel, which yields information on  $\text{O}+\text{He}$  recoil collisions and provides the fraction of the secondary hot atoms with energies  $E_r$  larger than the escape energy  $E_{esc}$ . The energy distribution function  $\rho(E_r|E)$  of recoil atoms, normalized to unity, is given by

$$\rho(E_r|E) = B(E - E_r|E) / \int B(E'|E) dE'. \quad (9.12)$$

The percentage of the recoil  $^4\text{He}$  and  $^3\text{He}$ , generated by both  $\text{O}(^3\text{P})$  and  $\text{O}(^1\text{D})$ , with energies above the escape energy threshold can be calculated as

$$\Gamma(E_i) = \int_{E_{esc}}^{\infty} \rho(E_r|E_i) dE_r. \quad (9.13)$$

One of the results clearly showed that the  $\text{O}(^3\text{P})$  and  $\text{O}(^1\text{D})$  relaxation kinetics are similar, and the related percentage of hot He agrees within 2%. It is possible therefore to treat them in escape modeling as single oxygen particles.

The altitude-dependent rate of production of hot O atoms with initial energy  $E_i$ ,  $f(E_i, h_O)$ , has been constructed considering the four dissociation channels of  $\text{O}_2^+$  with the exothermicities and branching ratios compiled in [26] and [27].

For the simplified one-dimensional atmospheric model, the altitude-dependent yield of hot helium atoms moving upwards with energy exceeding  $E_{esc}$  is given by:

$$P(h_{He}) = \frac{1}{2} \int_0^{\infty} dE_i \int_{h_O^{min}}^{h_{He}} dh_O f(E_i, h_O) \Gamma(E_i) n_{He}(h_{He}) \times \sigma_{He,O}^{eff}(E_i) T_O(h_O, h_{He}, E_i) T_{He}(h_{He}, E_i), \quad (9.14)$$

where the transparency factor  $T_O$

$$T_O(h_O, h_{He}, E_i) = \exp \left[ - \int_{h_O}^{h_{He}} dh' \sum_j \sigma_{j,O}^{eff}(E_i) n_j(h') \right] \quad (9.15)$$

is the probability that hot oxygen atoms, produced at the altitude  $h_O$ , reach altitude  $h_{He}$  without energy-loss collisions; the expression  $dh_O n_{He} \sigma_{O-He} \Gamma(E_i)$  is the probability to collide with the atmospheric He atoms in the atmospheric layers  $h_{He} - h_{He} + dh_{He}$ .  $T_O$  describes the energy-relaxation process in the upward moving flux of fast oxygen atoms and effective cross-sections  $\sigma_{j,O}^{eff}$  have been determined from the analysis of experimental data or results of the numerical solutions of the Boltzmann kinetic equation for thermalization of hot O in atmospheric gases [28–32].

The summation in the exponential includes the major constituents of the Martian upper atmosphere, CO<sub>2</sub>, CO, N<sub>2</sub>, O<sub>2</sub>, H<sub>2</sub>, H, Ar, and He. The corresponding cross sections for N<sub>2</sub>-O, O<sub>2</sub>-O and O-H were taken from [33], [28], [34], and [32] respectively. Since no data for collisions of atomic oxygen with CO<sub>2</sub> and CO molecules are available, we approximated these cross sections by those of O-O<sub>2</sub> and O-N<sub>2</sub> respectively. Similarly, O-H<sub>2</sub> collisions were approximated by O-N<sub>2</sub>. For further simplification, O-O collisions are not included in the energy relaxation scheme for nascent hot O, because these collisions do not reduce the total kinetic energy of hot O, if energetic recoil O atoms are also included in the upward flux of hot atoms. The densities of all species considered are taken from [35]. The other transparency factor  $T_{He}$  in eq. 9.14,

$$T_{He}(h_{He}, E_i) = \exp \left[ - \int_{h_{He}}^{h_{He}^{max}} dh' \sum_j \sigma_{j,He}^{eff}(E_i) n_j(h') \right] \quad (9.16)$$

represents the escape probability of energetic He atoms produced in collisions with hot O. The summation in eq. 9.16 is similar to that of eq. 9.15 except that the thermal helium is not included. In our calculation,  $h_O^{min}$  is chosen to be 130 km, and  $h_{He}^{max} = 700$  km. The altitude-dependent yield of escaping helium atoms,  $P(h_{He})$ , calculated from eq. 9.14, is shown in fig. 9.1 for low solar activity conditions. The solid curve shows results of our calculations with the diffusion cross sections defined earlier. To illustrate sensitivity of the He escape flux to collision cross sections,  $P(h_{He})$  has been computed by replacing in the transparency factors  $T_O$  and  $T_{He}$  the diffusion cross sections with the total cross sections. Results are shown in fig. 9.1 by the dashed curve. Although the total cross section accurately represents a collisional depth, they do not account properly for the energy relaxation in the upward O flux and they underestimate the contribution of energetic O atoms, produced in the region 150–200 km. These atoms collide with the atmospheric gas and lose only small fraction of their initial energy but contribute significantly to the collisional ejection of He atoms below and above the exobase level of 200 km. The yield of escaping He has a maximum around 230 km. The He column escape flux  $F^{esc}$  is obtained by integrating the production rates over all altitudes considered (130–700 km),  $F^{esc} = \int_{130}^{700} dh_{He} P(h_{He})$ . The percentage contribution to the column escape flux from each atmospheric layer of 25 km height is shown in the same figure. The greatest contribution comes from the layer ranging from 170–400 km, and the yield of escaping He from altitudes lower than 200 km is considerable. The computed column rate of He escape flux for the day side of the Mars atmosphere is  $F^{esc} = 1.7 \times 10^6$  cm<sup>-2</sup> s<sup>-1</sup> at the minimum of the solar activity. This value is in close agreement with an estimate of the He escape flux,  $1.6 \times 10^6$  cm<sup>-2</sup> s<sup>-1</sup>, obtained from the reported

rates of oxygen escape fluxes [35, 36], the cross section of O+He collisions, and the averaged value of the escape fraction. The column rate of the He escape rate computed with the total cross sections is seven times smaller, because it strongly suppresses the escape fluxes from the regions below the exobases of 200 km. We computed the rate of nonthermal losses  $Q$  of the atomic helium from the upper atmosphere of Mars as  $Q = F^{esc} S_{max}$ , where  $S_{max} = 2\pi(h_{He}^{max} + R_M)^2$  is the area of the illuminated Martian hemisphere at  $h_{He}^{max}$  and  $R_M$  is the volumetric mean radius. The result obtained considering both  $O(^3P)$  and  $O(^1D)$ , for  $h_{He}^{max} = 700$  km is  $8.9 \times 10^{23} \text{ s}^{-1}$ , which is almost twice the escape rate computed in the exobase approximation by [15] ( $5 \times 10^{23} \text{ s}^{-1}$ ). The agreement to an order of magnitude could be considered as accidental: the atmospheric, the ionospheric, and collision parameters are different in these two models, and the exobase approximation does not consider the atmospheric regions below 200 km, which are important for production of hot O and He escape fluxes. Strong angular anisotropy of collision cross sections yields a result differing several times with the HSA calculations [32, 35–37]. The knowledge of the accurate angular dependent cross sections is fundamentally important for the determination of the upward fluxes of energetic atoms. The degradation of upward atomic fluxes in the simplified modeling may be computed with the effective hard sphere cross sections, describing the energy relaxation process, or with related diffusion cross sections. Value of the effective hard sphere cross section can be determined only by fitting accurate data on the energy relaxation obtained in laboratory experiments, the solutions of the Boltzmann kinetic equation, or Monte Carlo simulations of the thermalization process.

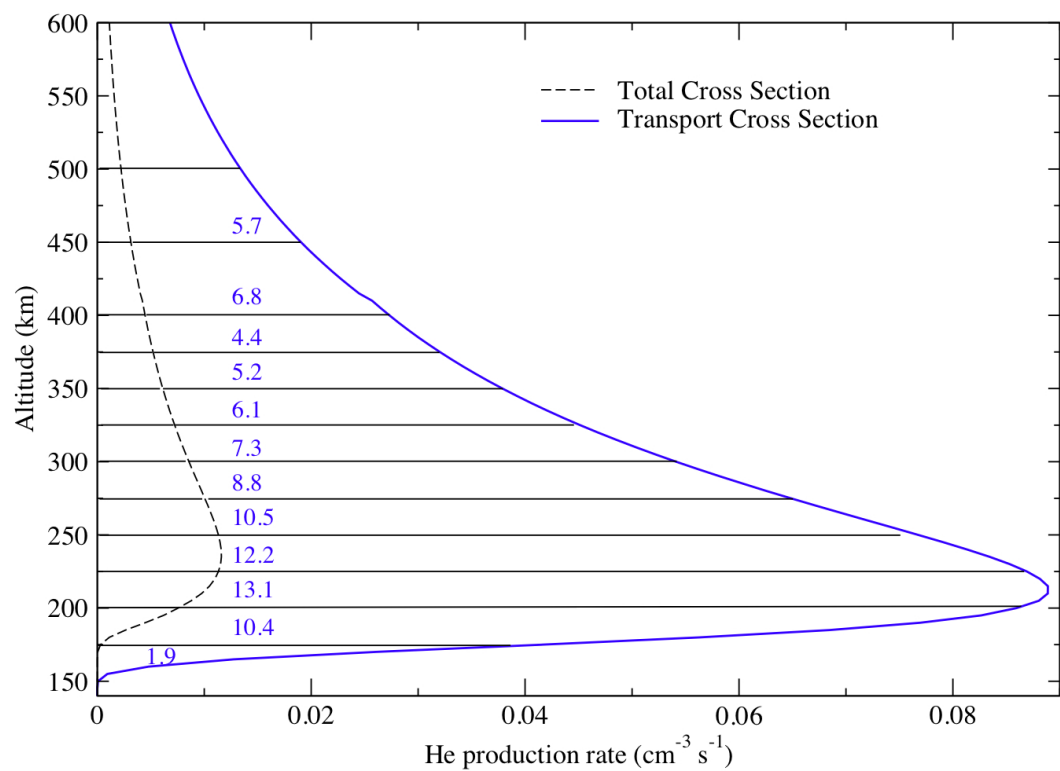


Figure 9.1 The production rate of  $^4\text{He}$  escape flux as a function of altitude. Dashes and solid lines represent results evaluated using total cross-section and transport cross-section respectively. Numbers in the figure represent the percentage contribution from each atmospheric layer.



# Bibliography

- [1] S. Bovino, P. Zhang, V. Kharchenko, F. A. Gianturco, and A. Dalgarno, *Geophys. Res. Lett.*, **38**, L02203, 2011
- [2] S. Bovino, P. Zhang, V. Kharchenko, and A. Dalgarno, *J. Chem. Phys.*, **135**, 024304, 2011
- [3] I. Oppenheim, K. Schuler, and G. Weiss, *Stochastic Processes in Chemical Physics: The Master Equation* (MIT Press, Cambridge, MA, 1977).
- [4] V. Kharchenko, J. T. Tharamel, and A. Dalgarno, *J. Atmos. Solar-Terr. Phys.* **59**, 107 (1997); V. Kharchenko, N. Balakrishnan, and A. Dalgarno, *J. Atoms. Solar-Terr. Phys.* **60**, 95, 1998
- [5] S. Bovino, P. Zhang, V. Kharchenko, and A. Dalgarno, *J. Chem. Phys.* **131**, 054302, (2009); P. Zhang, V. Kharchenko, M. J. Jamieson, and A. Dalgarno, *J. Geophys. Res.* **114**, A07101, 2009
- [6] P. Zhang, V. Kharchenko, A. Dalgarno *et al.*, *Phys. Rev. Lett.* **100**, 103001, 2008; P. Zhang, V. Kharchenko, and A. Dalgarno, *Mol. Phys.* **105**, 1485, 2007
- [7] K. Takahashi, N. Taniguchi, Y. Sato, and Y. Matsumi, *J. Geophys. Res.* **107**, 4290, 2002
- [8] V. Kharchenko, J. T. Tharamel, and A. Dalgarno, *J. Atmos. Solar-Terr. Phys.* **59**, 107, 1997
- [9] V. Kharchenko, N. Balakrishnan, and A. Dalgarno, *J. Atoms. Solar-Terr. Phys.* **60**, 95, 1998
- [10] P. Zhang, V. Kharchenko, and A. Dalgarno, *Molecular Phys.* **105**, 1485, 2007
- [11] V. Kharchenko and A. Dalgarno, *J. Geophys. Res.* **109**, D18311, 2004
- [12] U. von Zhan, and D. M. Hunten, *Science* **272**, 849, 1996; H. B. Niemann et al., *Science*, **272**, 846, 1996
- [13] M.E. Summers, and D. F. Strobel, *Icarus* **120**, 290, 1996
- [14] G. Nan, and P. L. Houston, *J. Chem. Phys.* **97**, 7865, 1992
- [15] Krasnopolsky, V. A., and G. R. Gladstone, *Icarus*, **176**, 395, 2005
- [16] Barabash, S., E. Kallio, R. Lundin, and H. Koskinen, *J. Geophys. Res.*, **100**, 21307, 1995
- [17] Krasnopolsky, V. A., and G. R. Gladstone, *J. Geophys. Res.*, **101**, 15765, 1996
- [18] Acuna, M. N., *Science*, **279**, 1676, 1998
- [19] Chassefière E. and F. Leblanc, **52**, 1039, 2004
- [20] Krasnopolsky, V., *Icarus*, **207**, 638, 2010

## BIBLIOGRAPHY

---

- [21] Fox, J. L., *Geophy. Rev. Lett.*, **20**, 1847, 1995
- [22] Hodges, R. R., *J. Geophys. Res.*, **105**, 6971, 2000
- [23] Ip, W.-H., *Geophy. Res. Lett.*, **17**, 2289, 1990
- [24] Kim, J., A. F. Nagy, J. L. Fox, and T. E. Cravens, *J. Geophy. Res.*, **103**, 29339, 1998
- [25] Fox, J. L., P. Zhou, and S. W. Bougher, *Adv. Space Res.*, **17**, 11203, 1996
- [26] Kella, D., P. J. Johnson, H. B. Pedersen, L. Vejby-Christensen, and L. H. Andersen, *Science*, **276**, 1530, 1997
- [27] Petrignani, A., F. Heldberg, R. D. Thomas, M. Larsson, P. C. Cosby and W. J. van der Zande, *J. Chem. Phys.*, **122**, 234311, 2005
- [28] Balakrishnan, N., V. Kharchenko, and A. Dalgarno, *J. Geophy. Res.*, **103**, 23393, 1998
- [29] Balakrishnan, N., V. Kharchenko, and A. Dalgarno, **103**, 3999, 1999
- [30] Kharchenko, V., J. Tharamel, and A. Dalgarno, *J. Atoms. So. Terr. Phys.*, **59**, 107, 1997
- [31] Takahashi, K., N. Taniguchi, Y. Sato, and Y. Matsumi, *J. Geophy. Res.*, **107**, 4290, 2002
- [32] Zhang, P., V. Kharchenko, M. J. Jamieson, and A. Dalgarno, *J. Geophy. Res.*, **100**, 103001, 2009
- [33] Kharchenko, V., A. Dalgarno, B. Zygelman, and J.-H. Yee, *J. Geophy. Res.*, **105**, 24899, 2000
- [34] Brunetti, B., G. Liuti, E. Luzzatti, F. Pirani, and F. Vecchiocattivi, *J. Chem. Phys.*, **74**, 6734, 1981
- [35] Fox, J. L. and A. Hać, *Icarus*, **204**, 527, 2009
- [36] Fox, J. L. and A. Hać, *Icarus*, **208**, 176, 2010
- [37] Krestyanikova, M. A. and V. I. Shematovich, *Solar System Research*, **40**, 384, 2006





## Relevant Publications

1. **S. Bovino**, M. Wernli, and F. A. Gianturco  
*Fast LiH destruction in reaction with H: quantum calculations and astrophysical consequences.*  
**Astrophys. J.**, 699, 383 (2009).
2. **S. Bovino**, T. Stoecklin, and F. A. Gianturco  
*The Ionic Pathways of Lithium Chemistry in the Early Universe: Quantum Calculations for  $\text{LiH}^+$  reacting with H.*  
**Astrophys. J.**, 708, 1560 (2010).
3. **S. Bovino**, M. Tacconi, F. A. Gianturco, and T. Stoecklin.  
*Is  $\text{H}^+$  an efficient destroyer of LiH molecules? A quantum investigation at the early universe conditions.*  
**Astrophys. J.**, 724, 126, (2010).
4. **S. Bovino**, M. Tacconi, and F. A. Gianturco,  
*LiH destruction by protons: a comparison of quantum models for an important astrochemical process.*  
**Physica Scripta**, 84, 028103, (2011)
5. M. Tacconi, **S. Bovino**, and F. A. Gianturco,  
*Testing the lithium chemistry for early universe models with a quantum reactive method.*  
**Rend. Fis. Acc. Lincei**, 22, 69, (2011)
6. **S. Bovino**, M. Tacconi, F. A. Gianturco, D. Galli, and F. Palla  
*On the relative abundance of LiH and  $\text{LiH}^+$  molecules in early universe models: new data from quantum reactions.*  
**Astrophys. J.**, 731, 107 (2011).
7. **S. Bovino**, M. Tacconi, F. A. Gianturco, and D. Galli  
*Ion chemistry in the early universe: revisiting the role of  $\text{HeH}^+$  with new quantum calculations.*  
**Astron. & Astrophys**, 529, A140, (2011).
8. **S. Bovino**, M. Tacconi, F. A. Gianturco  
*Photon-induced evolutionary rates of  $\text{LiHe}^+$  in early universe from accurate quantum computations.*  
**Astrophys. J.**, 740, 101, (2011).
9. M. Tacconi, **S. Bovino**, F. A. Gianturco  
*Direct and inverse reactions of  $\text{LiH}^+$  with  $\text{He}(^1S)$  from quantum calculations: mechanisms and rates.*  
**Phys. Chem. Chem. Phys.**, accepted (2011)



## Other Publications

1. **S. Bovino**, E. Coccia, E. Bodo, D. Lopez-Duran, and F. A. Gianturco.  
*Spin-driven structural effects in alkali doped  $^4\text{He}$  clusters from quantum calculations.*  
**J. Chem. Phys.**, 130, 224903 (2009)
2. **S. Bovino**, P. Zhang, V. Kharchenko, and A. Dalgarno.  
*Trapping hydrogen atoms from a neon gas-matrix: a theoretical simulation.*  
**J. Chem. Phys.**, 131, 054302 (2009)
3. **S. Bovino**, P. Zhang, V. Kharchenko, F. A. Gianturco, and A. Dalgarno.  
*Energy transfer in  $\text{O} + {}^{3,4}\text{He}$  collision and helium escape from Mars.*  
**Geophys. Res. Lett.**, 38, L02203, (2011)
4. **S. Bovino**, P. Zhang, V. Kharchenko, and A. Dalgarno.  
*Relaxation of energetic  $S(^1D)$  atoms in Xe gas: comparison of ab initio calculations with experimental data.*  
**J. Chem. Phys.**, 135, 024304, (2011)
5. **S. Bovino**, M. Tacconi, F. A. Gianturco  
*Cold Chemistry with ionic partners: quantum features of  $\text{HeH}^+$  ( $^1\Sigma$ ) with  $\text{H}(^1S)$  at ultralow temperatures.* **J. Phys. Chem. A**, 115, 8197 (2011)
6. D. Caruso, M. Tacconi, E. Yurtsever, **S. Bovino**, F. A. Gianturco  
*Quenching vibrations of cesium dimers by He at low and ultralow temperatures: quantum dynamical calculations,* **Eur. Phys. J. D**, in press (2011)